



Lehrstuhl für Raumfahrttechnik

Prof. Prof. h.c. Dr. Dr. h.c.
Ulrich Walter



Technische Universität München

Masterthesis

**Modeling and Verification of a
Thermo-Optical Sun and Earth Sensor
for Small Satellites**

MA-2018-19

Autor:

Christian Gscheidle

Supervisor: Dipl. Ing. (Univ.) Martin Dziura

Lehrstuhl für Raumfahrttechnik / Chair of Astronautics

Technische Universität München / Technical University of Munich

Acknowledgments

I would like to thank my supervisor Dipl. Ing. Martin Dziura. He always had an open ear for new ideas or approaches and gave me very helpful advice when I ran into trouble. I am also very grateful for him steering me in the right direction when he thought I would need it.

I must also express my gratitude to my parents Andreas and Monika for always supporting and encouraging me during my years of study.

Zusammenfassung

Die steigende Popularität kleiner Satelliten über die letzten Jahre lenkt zunehmend Aufmerksamkeit auf deren Lagebestimmungssysteme und die hohen Anforderungen an diese. Zwar existieren gute Lagebestimmungssensoren, die die Anforderungen für kleine Satelliten erfüllen, es gibt jedoch weiter vielversprechende Technologien, die bislang nur für größere Satelliten verfügbar sind.

Der Grobe Erd und Sonnen Sensor (CESS) von SpaceTech nutzt das Konzept der Bestimmung von Erd- und Sonnenrichtung mittels Thermometern und Fotodioden. Er ist flugerprobt, ist jedoch nicht für kleine Satelliten verfügbar.

Diese Arbeit untersucht deshalb die Anwendbarkeit des CESS-Konzepts auf einen Sensor aus günstigen Bauteilen für kleine Satelliten. Der Thermo-Optische Sonnen- und Erdsensor (TOSS), der zwei Thermometer und eine Fotodiode verwendet, bildet dafür die Grundlage. In dieser Arbeit wird die Modellierung des TOSS beschrieben, die Verifikation des Modells dargelegt und eine Bestimmung der Unsicherheiten in der Lagebestimmung mit Hilfe von Simulationen durchgeführt.

Um den Sensor umfassend beschreiben zu können, werden die Grundlagen von Wärmeübertragung und Photometrie erklärt. Physikalische Eigenschaften, die theoretisch wellenlängenabhängig sind, wurden spektral modelliert. Die geometrische und numerische Struktur des Modells und die angewandten numerischen Methoden werden erklärt. Mit einfachen Beispielfällen und experimentellen Daten werden die numerischen Methoden und die benutzten Modellparameter verifiziert. Das verifizierte Modell wurde für Simulationen und Einflussanalysen benutzt, um Unsicherheiten in der Lagebestimmung auf Grund von Variationen in den Modellparametern zu bestimmen.

Die Simulationen zeigen, dass der TOSS eine Genauigkeit erreichen kann, die für einen groben Lagebestimmungssensor für Erd- und Sonnenrichtung ausreichend ist und bestätigen das Konzept. Die Grenzen, in denen der Sensor funktioniert, wurden bestimmt. Die Unsicherheiten in der Lagebestimmung durch Albedostrahlung und die Infrarotemission der Erde wurden quantifiziert und sie sind gering im Vergleich zu den Unsicherheiten auf Grund anderer Modellparameter. Durch eine Bestimmung der Art der Unsicherheiten wurde verdeutlicht, dass der Sensor noch Entwicklungspotential besitzt. Das in dieser Arbeit entwickelte Modell und die Simulationen mit ihm können helfen, ihn zu verbessern und zu einem flugtauglichen Sensor weiter zu entwickeln.

Abstract

The increasing demand of small satellites, such as CubeSats, in the past years draws attention to the demanding challenges regarding their attitude determination. Good attitude determination sensors exist, which fulfill the requirements stated by small satellites, but there are still promising technologies which are available only for larger satellites.

The Coarse Earth Sun Sensor (CESS) by SpaceTech uses a technology concept, which determines the direction of the Sun and of Earth by measuring radiation with thermometers and photo diodes. It has an extensive flight heritage, but is not available for small satellites.

This thesis therefor scrutinizes the practicability of applying the CESS concept to a sensor for small satellites using low cost components. The Thermo-Optical Sun and Earth Sensor (TOSS) serves as basis. It uses two thermometers and a photo diode to determine a satellites attitude. The thesis contains modeling of a TOSS for small satellites, the model's verification and simulation based on the model to assess uncertainties in the attitude determination.

To be able to describe the sensor, the basics of heat transfer and photometry are explained. Wavelength dependent physical properties were modeled spectral to distinguish between different radiation spectra. The model's geometric and numerical structure is given and the numerical methods used are explained. The numerical methods and the used model parameters are correlated and verified with experimental data and simple generic test cases. The verified model was then used for simulations and sensitivity analyses which gave insight into the sensor's uncertainties due to parameter variations.

The simulations show that the TOSS can reach an accuracy which is sufficient to qualify it as a coarse sensor for the direction of both Sun and Earth and to confirm the concept. The boundaries in which the sensor functions properly are determined. The uncertainties in attitude measurements due to Earth's albedo radiation and Earth's infrared emission are quantified and show to be minor compared to uncertainties from other model parameters. Characterizing the sources of uncertainties, it becomes apparent that the sensor still requires development to become a viable attitude determination sensor for future missions. The model developed and verified in this thesis and its simulation results can help making the right improvements.

Contents

1. Introduction	1
1.1. Thesis Outline	1
2. State of the Art	3
2.1. Attitude Determination Sensors	3
2.2. MOVE-II ADCS	6
2.3. Coarse Earth Sun Sensor (CESS)	7
2.4. Thermo-Optical Sun and Earth Sensor (TOSS)	7
2.5. Thesis Aims	9
3. Heat Transfer	11
3.1. Thermal Conduction	11
3.2. Convection	12
3.3. Radiation	13
3.3.1. Basic Quantities and Nomenclature	14
3.3.2. Planck's Law, Wien's Law and the Stefan-Boltzmann Law	14
3.3.3. Radiant Heat Transfer	16
3.3.4. Photometric Law and View Factors	17
3.3.5. Reflectance, Transmittance, Absorptivity and Emissivity	20
3.3.6. Solar Irradiation	21
3.3.7. Earth's Albedo	22
3.3.8. Earth's Infrared Emission	23
4. Photometry	26
4.1. Spectral and Radiant Sensitivity	26
4.2. Amplification and Analog to Digital Conversion	28
5. Model Geometry and Parameters	29
5.1. TOSS v2.2 Model	30
5.2. TOSS v3 Model	31
5.3. Printed Circuit Board	32
6. Numerical Methods	35
7. Verification and Experiments	38
7.1. Simulation Code Verification	38
7.1.1. No Gradients Case	38
7.1.2. Heat Diffusion Case	39
7.1.3. IR Radiation Case	39

7.1.4. Radiation Equilibrium Case	40
7.1.5. Temporal Behavior	41
7.2. RACOON-Lab Experiments	42
7.2.1. Photo Diode Experiments	43
7.2.2. Thermal Experiments	44
7.2.3. RACOON-Lab Experiments Summary	46
8. Simulation and Analysis	47
8.1. Sensitivity Analysis	49
8.2. Simulation Evaluation Method	49
8.3. Sensor Accuracy	52
8.4. Influence Analysis	54
8.4.1. Albedo Radiation	55
8.4.2. Earth IR Emission	55
8.4.3. Solar Radiation	56
8.4.4. Thermometer Surface Coating	57
8.4.5. PCB Surface Coating	58
8.4.6. Thermometer Thermal Mass	59
8.4.7. Cutout Analysis	60
8.5. Discussion	61
9. Conclusion	64
A. Bibliography	67
B. Statistics	72
B.1. Stochastic Methods	72
B.2. Discrete Statistics	73
B.3. Linear Regression	74
B.4. Error Propagation	76
C. Additional Figures	77
C.1. RACOON-Lab Experiments	77
C.2. TOSS Schematics	80
C.3. Matlab Struct	82

List of Figures

2.1. Radiation Overview	5
2.2. Attitude Sensors	6
2.3. TOSS Boards	8
3.1. Geometric Quantities for View Factor Calculation	16
3.2. View Factor Geometries	18
3.3. Angle Cones	19
3.4. Orbit Geometry	20
3.5. Spectral Surface Properties	21
3.6. Solar Spectra	22
3.7. Spectral Albedo Data	23
3.8. Earth IR Spectrum	24
4.1. Spectral Sensitivity	26
4.2. Quantum Response	27
5.1. Thermal Exchange Path	29
5.2. TOSS v2.2 Geometric Model	30
5.3. TOSS v2.2 Thermal Model	31
5.4. TOSS v3.0 Geometric Model	31
5.5. TOSS 3.0 Thermal Model	32
6.1. Program Flow Chart	36
7.1. Verification - No Gradients	38
7.2. Verification - Heat Diffusion	39
7.3. Verification - IR Radiation	40
7.4. Verification - Radiation Equilibrium	40
7.5. Verification - Solver Time Step	41
7.6. RACOON-Lab Radiation Environment	42
7.7. RACOON-Lab Measured and Simulated Photocurrents	43
7.8. RACOON-Lab Measured and Simulated THM Temperatures	45
7.9. RACOON-Lab Cross Plot	46
8.1. Temperature Field	48
8.2. Evaluation Work Flow	49
8.3. Isosurface Example	51
8.4. Intersections Example	51
8.5. Sensor Uncertainty Intersections	53
8.6. Sensor Uncertainty Histogram	54

8.7. Sensor Uncertainty Histogram for Albedo	55
8.8. Sensor Uncertainty Histogram for Earth IR	56
8.9. Sensor Uncertainty Histogram for Solar Irradiation Variation . . .	57
8.10. Sensor Uncertainty Histogram for THM Absorptivity	58
8.11. Sensor Uncertainty Histogram for PCB Absorptivity	58
8.12. Sensor Uncertainty for THM Thermal Mass Variation	59
8.13. Sensor Analysis Transient Cutout	60
B.1. Accuracy and Precision	72
B.2. Normal Distribution	73
C.1. RACOON-Lab Simulated and Measured Temperatures THM1 . .	78
C.2. RACOON-Lab Simulated and Measured Temperatures THM2 . .	78
C.3. RACOON-Lab Distance Current Measurements	79
C.4. TOSS v2.2 Schematic	80
C.5. TOSS v3 Schematic	81

List of Tables

3.1. Properties of Air at Sea Level	13
3.2. Radiometric Terminology and Units	15
3.3. MODTRAN 5 Input Parameters	25
5.1. TOSS v2.2 Nodes	30
5.2. TOSS v3.0 Nodes	32
5.3. FR4 Properties	33
5.4. DS18B20U Thermal Properties	33
8.1. Inherent Sensor Uncertainty Statistics	53
8.2. Sensor Uncertainty Statistics for Albedo Variation	55
8.3. Sensor Uncertainty Statistics for Earth IR Variation	56
8.4. Sensor Uncertainty Statistics for Solar Irradiation Variation	56
8.5. Sensor Uncertainty Statistics for THM Absorptivity Variation	57
8.6. Sensor Uncertainty Statistics for PCB Absorptivity	59
8.7. Sensor Uncertainty Statistics for THM Thermal Mass Variation	60
8.8. Uncertainty Summary	61
B.1. Basic Error Propagation	76
C.1. RACOON-Lab Experiment Parameters	77

List of Symbols

Formula Symbols

Symbol	Unit	Description
a	m^2/s	Thermal diffusivity
\hat{a}, \hat{b}	\sim^1	Linear regression coefficients
A	m^2	Area
B	$\text{W}/\text{m}^2 \cdot \text{nm}$	Black-body radiation
c	$\text{J}/\text{kg} \cdot \text{K}$	Specific heat capacity
d	m	Distance
E	$\text{eV} \setminus \text{J}$	Energy
f	\sim	Simulation
F	1	View factor
G	1	Gain
h	m	Height
H	m	Height
I	A	Current
I	W/sr	Radiant intensity
k	$\text{W}/\text{m} \cdot \text{K}$	Thermal conductivity
L	$\text{W}/\text{m}^2 \cdot \text{sr}$	Radiance
m	kg	Mass
M	W/m^2	Radiant emittance
n	1	Count / Number of particles
N	1	Resolution
\mathcal{N}	\sim	Normal distribution
p	1	Probability
Q	J	Thermal energy / heat

¹ \sim = Depends on input of operation

Symbol	Unit	Description
r	m	Radius
R	Ω	Resistance
R^2	1	Coefficient of Determination
s	1	Standard deviation
S	1	Sensitivity
t	s	Time
T	K	Temperature
U	J	Internal Energy
U	V	Voltage \ electric potential
V	m ³	Volume
x, y, z	m	Spacial coordinate \ distance
α	1	Absorptivity
β	rad	(Elevation) Angle
δ	1	Uncertainty
ε	1	Emissivity
η	1	Efficiency
λ	m	Wave length
μ	\sim	Mean
ν	Hz	Frequency
ρ	kg/m ³	Density
ϱ	1	Reflectance
ξ	1	Albedo share
τ	1	Transmittance
ν	m ² /s	Kinematic viscosity
Υ	1	Inverse probability distribution
ϕ	1	Probability density function
φ	rad	Azimuth angle
Φ	W/m ²	Radiant flux
ω	W	Internal heat sources
Ω	\sim	Isosurfaces

Constants

Symbol	Value and Unit	Description
b	$2.898 \times 10^{-3} \text{ m} \cdot \text{K}$	Wien's displacement constant
c	$2.998 \times 10^8 \text{ m/s}$	Speed of light in vacuum
h	$6.626 \times 10^{-34} \text{ J} \cdot \text{s}$	Planck constant
k_B	$1.381 \times 10^{-23} \text{ J/K}$	Boltzmann constant
q	$1.602 \times 10^{-19} \text{ C}$	Elementary charge
r_S	$6.963 \times 10^8 \text{ m}$	Radius of the Sun
r_E	$6.370 \times 10^6 \text{ m}$	Radius of Earth
T_{CMB}	2.725 K	Cosmic microwave background temperature
σ	$5.670 \times 10^{-8} \text{ W/m}^2 \cdot \text{K}^4$	Stefan-Boltzmann constant

Subscripts and Superscripts

Symbol	Description
A	Albedo
b	Black body
$crit$	Critical
E	Earth
g	Band gap
h	Convection \ convective
k	Conduction \ conductive
i, j, n	Iteration markers
min	Minimum
max	Maximum
p	Photon
PD	Photo diode
q	Charge
r	Radiation \ radiative
S	Sun

Symbol	Description
--------	-------------

sat	Satellite
W	Wall
λ	Spectral
σ	68%-Error
Ω	Radiant
\parallel	Parallel
\perp	Perpendicular/Through
∞	Environment

Abbreviations

ADC	Analog Digital Converter
ADCS	Attitude Determination and Control System
AM0	Air Mass Zero
CMB	Cosmic Microwave Background
CESS	Coarse Earth Sun Sensor
CFRP	Carbon Fiber Reinforced Polymer
COTS	Commerical-of-the-shelf
FOV	Field of View
IR	Infrared
LEO	Low Earth Orbit
LRT	Chair of Astronautics (Lehrstuhl für Raumfahrttechnik)
MODTRAN	Moderate Resolution Atmospheric Transmission
MOVE	Munich Orbital Verification Experiment
NASA	National Aeronautic and Space Agency
OFAT	One-factor-at-a-time
PCB	Printed Circuit Board
THT	Through-hole Technology
TOSS	Thermo-Optical Sun and Earth Sensor
RACOON-Lab	Robotic Actuation and On-Orbit Navigation Laboratory
SMT	Surface-mounting Technology
THM	Thermometer
TUM	Technical University of Munich (Technische Universität München)

1. Introduction

Satellites require accurate knowledge on their position and orientation to ensure their ability to fulfill their designation [1]. All systems assigned to determining a satellite's attitude in space are considered to be part of the Attitude Determination and Control System (ADCS). Requirements to these systems vary greatly with the task assigned to them. For example, telescopes require a far better pointing accuracy and stability than regular solar cells. Therefore, modern satellites utilize a variety of sensors to determine their attitude, including Sun sensors, Earth sensors, magnetometers and star trackers. They differ by the physical properties they use to determine the attitude, their accuracy, their complexity, the amount of necessary signal processing and their price. Additionally, not all sensors are able to determine the attitude at any point in time. All types of sensors have advantages but also suffer from individual drawbacks. For example, a highly specialized star tracker is used when precise positioning is necessary, but these sensors are expensive and cannot be used during certain mission phases. For initial orientation and in cases of emergency, coarse measurements are often necessary or sufficient and simpler sensors are used.

An additional point, which has to be considered, especially during development of ADCS sensors and systems, are the differences in the environment where the sensors are intended to function. Space is usually very cold, has no atmosphere and extreme radiation is present. Attitude sensors must be able to survive this harsh environment while retaining full functionality. Therefore, new sensors are constantly being developed promising higher reliability, longer survivability, lower power consumption, smaller form factors or higher accuracy.

In this thesis, the object of interest is a new Thermo-Optical Sun and Earth Sensor (TOSS) for small satellites. The sensor should be able to reliably determine a satellite's attitude with respect to both Sun and Earth by using different radiation measurements. Its feasibility and performance are assessed in the following chapters which are shortly introduced in the next section.

1.1. Thesis Outline

This thesis covers development of the thermal and optical model of the new Thermo-Optical Sun and Earth Sensor (TOSS), the verification of its model, simulations conducted to assess its attitude determination uncertainty and a discussion of the results. The contents of it are given in the following.

In chapter 2, present day attitude determination sensor concepts and their histories are presented. The idea behind this thesis is described in detail and the sensor, which shall be modeled, is introduced.

In chapter 3, the thermal exchange mechanisms, which were necessary to assemble a proper model, are discussed in detail. Formulas for analytic calculation of conduction are given. For experiments under atmospheric conditions, a simple natural convection model is implemented. As radiation is the heat exchange mechanism of interest for this thesis, it is described in depth. Spectra of solar radiation, Earth's albedo and Earth's Infrared (IR) emission are given. Spectral surface properties are discussed as well as view factors for radiation.

Chapter 4 explains the physics how photo diodes work and builds a model relating incident radiation to produced photocurrent. Additionally, the measurement method is explained.

Chapter 5 describes the model. The geometric structure for the evaluated sensor boards is given along side with the model's thermal structure. Material parameters for important components are presented.

Chapter 6 gives an overview over the implementation in Matlab and the used numerical methods.

Chapter 7 shows generic verification cases for the simulations' solver and presents experiments conducted to verify and correlate the numerical model to the real sensor.

In chapter 8, the model is used to determine the influence of important parameters and the subsequent uncertainties of the Thermo-Optical Sun and Earth Sensor. A method to gain Sun and Earth angles from temperature and photocurrent measurements is presented. By varying important parameters their influence on the sensor's accuracy is determined. Furthermore, the results from the uncertainty analysis and their implications are discussed.

Chapter 9 finalizes the thesis with a conclusion. Advantages and points for improvement are discussed. A review over the work, which has been done, is given and possible future applications are presented.

2. State of the Art

In the following, a short overview over commercially available attitude determination sensors for small satellites is given. Additionally, the motivation for developing the new sensor is presented.

Nowadays, there is an increasing interest in small satellites, especially for ones with a mass less than 10 kg [2]. Since 2013 over 500 NanoSats and CubeSats have been launched successfully into space from all over the world, providing valuable platforms for universities, institutions and businesses for research, communication or technology demonstration [3]. Similar to bigger satellites, these small satellites require an ADCS. Early CubeSats featured simple sensors, such as magnetometers [4] and Sun sensors. Over time sensors have become more sophisticated and accurate. However, restrictions regarding volume, mass, power and cost can be hard to fulfill and still influence the sensor selection. For example, standard 1U CubeSats must deal with restriction regarding size of $V_{sat} < 100 \times 100 \times 113.5 \text{ mm}^3$ and mass of $m_{sat} < 1.33 \text{ kg}$ [5]. By combining multiple units, up to 27U CubeSats can be created, which increase the limits concerning mass and volume [6]. Nevertheless, these requirements greatly influence and complicate the choice and design of the ADCS [7]. Therefore, attitude determination sensors should ideally be lightweight, small and low power consuming while providing accurate measurements. To overcome financial budget limitations, developers often default to Commercial-off-the-shelf (COTS) components, which are mostly easy to obtain while being significantly cheaper than dedicated space hardware. In return, these components can induce uncertainties that can lead to loss of accuracy for the ADCS.

2.1. Attitude Determination Sensors

There are numerous technologies and sensors available for attitude determination [1, 8]. Sensors, such as inertial measurement units or gyroscopes, provide attitude determination based on measuring rates of change and are often called relative sensors. Such sensors are not discussed in the following as the focus of this thesis is absolute attitude determination. Some sensor concepts providing absolute attitude measurements are now addressed.

Magnetometers have been used frequently in past small satellite missions. By measuring the magnitude and direction of Earth's magnetic field, an estimation of the satellites current attitude can be made. The sensors have substantial advantages as they are lightweight, consume small amounts of power, are small and reliable [1]. However, the models used to predict the magnetic field can be inaccurate and the magnetic field's magnitude rapidly decreases with increasing distance from Earth which limits the achievable accuracy. For small satellites

magnetometers are also often used as they are mandatory when using the popular approach of magnetorquers for detumbling and attitude control.

Star trackers use the position of the stars to determine the attitude of the satellite by comparing them to known star patterns [8]. They are used for high precision tasks, for example remote sensing operations. Although star trackers can potentially provide attitude determination up to < 5 arcsecond [9], even small ones are usually too big ($50 \times 50 \times 113 \text{ mm}^3$) and too heavy ($m = 245 \text{ g}$)[9] for 1U or 2U CubeSats. The high price of star trackers is an additional inhibitor to integrate one in a CubeSat [10].

In contrast to focusing on distant celestial bodies, Earth sensors are instruments designed to detect the direction of Earth, usually called nadir vector. They have been well understood for a long time [11]. Mainly, there are two different Earth sensor concepts, horizon scanners and IR scanners [8]. Most horizon sensors consist of multiple trackers, each monitoring the horizon in one direction. They are configured to detect deviations from an Earth-shaped reference. Internally, the trackers are lines of infrared sensitive photo diodes with a narrow field of view focused on the horizon. Changing signals from the line of diodes and a deviation from the reference can be related to change in attitude. Horizon sensors are used for Earth focused sensors with low spin rates. Thermal Earth sensors utilize Earth's thermal emission to distinguish between the comparably warm Earth and cold Cosmic Microwave Background (CMB) visually surrounding Earth. The difference in incident thermal radiation can be related to the visibility angle of Earth. In general, Earth sensors are light weight, reliable and small. Although, the accuracy of Earth sensors is comparably inaccurate.

Another major and very often used category of attitude determination sensors are Sun sensors. "A Sun sensor determines a spacecraft's orientation with respect to the Sun" [12]. The instruments are designed to measure radiation in the visible spectrum and have been very popular up until today [13]. Because of their relative simplicity, almost all spacecrafts use Sun sensors of some sort and multiple models in various configurations are commercially available [12, 14, 15, 16]. Using the Sun as reference direction is reasonable because of its high brightness relative to other celestial objects and its small apparent radius [17]. Usual applications are:

- Solar array pointing: Knowing the direction of the Sun is essential for maximizing the power available from solar arrays because they work best if pointed directly towards the Sun.
- Instrument safety: Optical instruments, for example telescopes, are very sensitive to irradiation and can be destroyed by direct solar irradiation. Simple, robust and reliable Sun sensors ensure that safety measures, such as closing shutters or lids, can be taken before the instruments are damaged.
- Initial orientation, fail-safe mode and low power mode: In cases of emergency very precise attitude determination is often of lower priority while

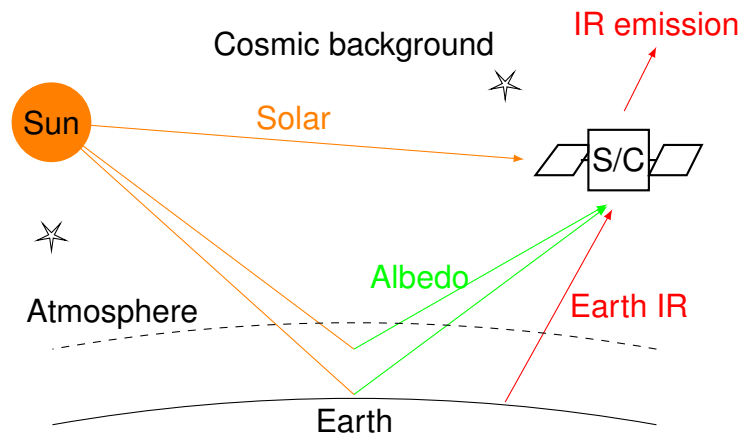


Fig. 2.1.: Overview over the radiation environment experienced by a satellite in a LEO. Radiation shown: Direct irradiation by the Sun, IR radiation emitted by Earth, the albedo of Earth reflected by both Earth's surface and atmosphere and IR radiation emitted by the spacecraft itself.

saving power and ensuring a coarse attitude determination is more important. This state also appears in the initial phase after launch.

Advantages of Sun sensors are their simplicity, reliability, low weight, low cost, low power demand and comparably high achievable accuracy [1]. In contrast, Sun sensors require the Sun to be in their Field of View (FOV) for attitude determination, meaning that in Earth's shadow Sun sensors cannot give a proper measurement. Furthermore, Sun sensors can be influenced by solar radiation reflected by Earth, called albedo radiation. This radiation is very hard to predict as it depends on the hardly predictable surface and atmospheric conditions on Earth. Albedo intensity can be up to 30% of nominal solar radiation, which can cause major inaccuracy in Sun sensor [18]. This issue is often handled by having multiple sensor on differently oriented surfaces on the satellite and filtering the measurements.

Figure 2.1 gives an overview over a satellite's radiation environment. Especially for Sun sensors, solar reflection from Earth's surface or its atmosphere can significantly influence the accuracy of these sensors. "The model predicts that diffuse reflected light can cause errors of up to 10° in Coarse Sun Sensor (CSS) measurements and 5 to 10 arcsecond in Fine Sun Sensor (FSS) measurements, depending on the spacecraft's orbit and attitude [18]. Earth sensors are also subject to uncertainties in the IR emission and the structure of Earth's atmosphere [19]. For these reasons, satellites usually combine multiple sensors of multiple types to determine their current attitude.



Fig. 2.2.: Pictures of two attitude sensors: a) Digital Sun sensor NANO-ISS60 by SolarMEMS[15], b) Coarse Earth and Sun Sensor (CESS) by SpaceTech [20].

2.2. MOVE-II ADCS

For research and education, the Chair of Astronautics (Lehrstuhl für Raumfahrt-technik) (LRT) at the Technical University of Munich (Technische Universität München) (TUM) is currently developing the second iteration of the Munich Orbital Verification Experiment (MOVE) [21], following the successful First-MOVE [22]. MOVE-II will be a 1U CubeSat featuring a sophisticated ADCS. “The ADCS consists of six circuit boards (five satellite side panels and one central circuit board in satellite stack), each equipped with a microcontroller, sensors and an integrated coil” [23]. MOVE-II will rely on measurements of Earth’s magnetic field and digital Sun sensors for attitude determination. For that, each of the five side panels will include a magnetic field sensor BMX055 by Bosch, which has a thermometer included, a Sun sensor NANO-ISS60 by Solar Mems and three DS18B20U temperature sensor by Maxim Integrated.

A picture of the Sun sensor is given in figure 2.2a. Its data sheet states: “The accuracy of the measurements depends on the integration and the calibration processes. The NANO-ISSX sun sensors are not calibrated.” [15]. For comparison, technologically equal sensors can reach an accuracy in the Sun direction measurement of $< 1^\circ$ [1]. It weights < 5 g, has a size of $18 \times 18 \times 3.85$ mm³ and a FOV of $120^\circ \times 120^\circ$. The DS18B20U thermometers are standard COTS temperature sensors with an accuracy of 0.5 K while being small and lightweight [24].

2.3. Coarse Earth Sun Sensor (CESS)

However, in 1997 a patent on a “Coarse Sun and Earth sensor for satellites and methods for coarse position determination of Sun and Earth aboard a satellite” (German: “Grober Sonnen- und Erdsensor für einen Satelliten sowie Verfahren zur groben Positionsbestimmung von Sonne oder Erde an Bord eines Satelliten”) was filed by Bernhard Doll and Wolfgang Pitz [25]. Their sensor consists of a silicon solar cell and two temperature sensors (PT1000) with different thermo-optical surfaces. By measuring the solar array’s photocurrent and the temperatures, determination of the Earth vector and the Sun vector is possible. A rendering of one of their sensor heads is given in figure 2.2b. At least six individual sensor heads should be attached to a satellite so that they can see the entire space around the satellite. Today, the sensor system is distributed as CESS by SpaceTech GmbH, Immenstaad, and has been used in multiple missions, for example TanDEM-X, CryoSat-2 and GOCE [20, 26].

The CESS gains attitude information in multiple steps. Initially, the sensor’s thermal inertia is accounted for and the incident solar radiation is determined. Then Earth’s thermal emission and from it the nadir direction is calculated. Next the albedo’s influence is assessed and removed. Finally, the Sun direction is determined.

The original sensor is designed to have a 68% vector error of $< 15^\circ$ for Earth and $< 10^\circ$ for the Sun at turn rates less than 0.2 r/min and small inertia to enable measurements at higher turn rates. Furthermore, low noise, complete visibility and error tolerance were aimed for along with low power consumption, mass and assembly effort. Judging from the pictures and the patent, the sensor’s FOV can be assumed to be the entire hemisphere over its top surface. Although, one sensor head’s size of $95 \times 46 \times 40 \text{ mm}$ and mass of $\approx 44 \text{ g}$ make the entire sensor system impractical for usage on small satellites [26].

For the most recent version of the CESS the datasheet states, that the accuracy was improved to have a mean Earth vector error of $< 5^\circ$ and a mean Sun vector error of $< 3^\circ$. However, the improved sensor head’s size ($108 \times 42 \times 58 \text{ mm}^3$) and its mass (80 g) still prevent the usage in small satellites [20].

2.4. Thermo-Optical Sun and Earth Sensor (TOSS)

Comparing the MOVE-II ADCS and the CESS, similarities between the sensor systems are notable. Both approaches utilize photo diodes and have thermometers as components albeit the MOVE system’s thermometers are not used for attitude determination. Instead they are used for “later on-orbit debugging in case of hardware failures and are used by the Thermal subsystem to get an overall thermal view of the satellite” [23]. This states that in the MOVE ADCS thermometers are not actively participating in attitude determination. In contrast,

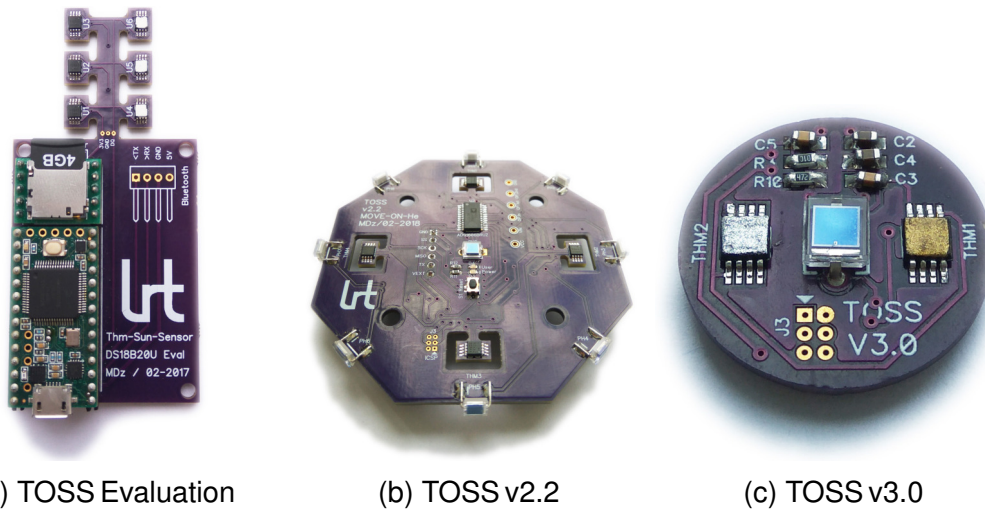


Fig. 2.3.: Pictures of the Thermo-Optical Sun and Earth Sensor (TOSS) boards:
a) TOSS Evaluation board with six DS18B20U for thermometer evaluation, b) TOSS v2.2 sensor board with four DS18B20U temperature sensors and nine BPW34 photo diodes for prove of concept and verification, c) TOSS v3.0 sensor board with two DS18B20U temperature sensor one BPW34 photo diode and a similar form factor compared to the NANO-ISS60 used in the MOVE-II ADCS.

the CESS heavily relies on a temperature measurements to gain information regarding the attitude of the satellite, mainly the nadir direction.

To address this issue and seeing that there are no technologically equivalent systems to the CESS available for small satellites, development of the Thermo-Optical Sun and Earth Sensor (TOSS) has begun [27]. Based on the CESS patent, the system uses thermometers and photo diodes to determine the Earth and Sun elevation, while reducing the influence of albedo radiation. The general idea is that there are three unknown parameters for attitude determination with the TOSS system: The amount of albedo irradiation and the angles of both Earth and Sun. Three linearly independent measurements should, therefore, be enough to determine the three unknowns. With two thermometers featuring different optical coatings and a photodiode measuring incident radiation in the solar wavelengths, a TOSS sensor should be able to determine the unknowns and should be able to function as a sensor for the nadir and the Sun direction.

Development has been done in multiple steps, each focusing on different aspects. Figure 2.3 shows the history of the TOSS project:

- TOSS Evaluation: The initial sensor board is shown in figure 2.3a. This board was primarily used to prove that significant temperature differences are measurable using different surface coatings. For this task, the board was equipped with six DS18B20U temperature sensors, three of which were either coated with white paint or left uncovered.

- TOSS v2.2: The subsequent TOSS v2.2 is shown in figure 2.3b. As the TOSS v2.1 had only slight geometric differences compared to the TOSS v2.2, it will not be discussed further in this thesis. The focus of this iteration was to include all hardware necessary to reproduce thermo-optical behavior comparable to the CESS. The TOSS v2.2 featured four DS18B20U temperature sensors [24] which could be coated individually to increase information gain. One vertically facing Vishay BPW-34 photo diode [28] was included for solar intensity measurement. Additionally, eight supplementary, horizontally facing photo diodes were included into the design for pseudo-satellite balloon mission [27]. Since these photo diodes are not an crucial aspect of the design, they will not be discussed further. The board has a size of 70 mm across.
- TOSS v3.0: The currently most advanced sensor is shown in figure 2.3c. This design focuses on reducing the sensor's size to a form factor similar to the NANO-ISS60. The TOSS v3 features two DS18B20U temperature sensor and one vertically facing BPW-34 photo diode. The board has a diameter of 20 mm.

Common for all TOSS variants is that the processing of measurements is done in the on-board microcontroller and the two layer FR 4 Printed Circuit Board (PCB) as structure. One important focus while developing the sensor was using COTS components in order to reduce the system's cost and to make it possible for fast replication as well as hardware in the loop development. A more in-depth description of the TOSS's legacy is given in [27].

However, just measuring the temperature or the photocurrent does not provide useful attitude information. The TOSS approach is infeasible without a model with which simulations predicting its behavior can be made. With a model and the simulations, measurements can then be related with radiation incidence angles and an attitude determination is possible. Development of the model required for predicting the sensor's behavior is this thesis' purpose and the requirements are presented in the following section.

2.5. Thesis Aims

The ambitions of this thesis are to construct a thermal model for the TOSS v2.2 and the TOSS v3.0 sensor board, verify the model and use it to evaluate the sensor's theoretical accuracy. The overall goal is to determine, if the TOSS concept can yield a system, which can reliably measure Earth and Sun angle, is robust against influences from albedo and Earth's infrared radiation and has requirements for volume, mass and power compatible with small satellites.

The model should represent the existing sensor, be numerically evaluable and uncomplicated. It should include knowledge of all important sensor parameters. Focus is to be laid on easy interchangeability of parameters defining the model so that the solver can be used for evaluation of future sensor's models. All

thermal exchange mechanisms relevant to the sensor have to be modeled to ensure proper thermal behavior. To increase the degrees of freedom for later optimization, radiation should be modeled as a spectral phenomenon.

The model should be verified to be able to use it as basis for analysis. This means, simulations with the sensor's model should be able to predict or reproduce experimentally acquired data. Also the numerical methods must be verified.

With a properly verified model, assessment of the TOSS sensor's accuracy should be done based on simulations. The method should be reproducible and statistically meaningful. Important parameters, such as albedo or surface coating, are to be investigated and discussed.

3. Heat Transfer

This chapter will provide insight on the thermo dynamic principles of heat exchange between distinct systems and how these physical processes can be modeled mathematically. The three transfer mechanisms conduction, convection and radiation are individually scrutinized and related to the application in the TOSS model. The equations and correlations necessary for modeling heat transfer were taken from [29] and [30].

The first law of thermodynamics is the basis for all further considerations. It is given in equation 3.1

$$\Delta U = Q + W \quad (3.1)$$

and states that the change in internal energy ΔU is equal to the heat Q transferred to it minus the work W it does on its environment. For a diabatic closed system, equation 3.2 determines the internal energy's temporal derivative with heat fluxes over its system borders and internal heat sources.

$$\frac{dU}{dt} = \rho c V \frac{\partial T}{\partial t} = \sum_i \Phi_i + V \sum_j w_j \quad (3.2)$$

where ρ is the density in kg/m^3 , c is the specific heat capacity in $\text{J}/\text{kg} \cdot \text{K}$, V is the volume in m^3 , A is the area in m^2 , Φ are heat fluxes in W/m^2 , w are internal heat sources in W , T is the temperature in K and t is the time in s . In order to know how the temperature of a system transient change, the heat fluxes over its system borders and its internal heat sources have to be modeled and calculated. Also the material properties influencing thermal exchange have to be known.

3.1. Thermal Conduction

Thermal conduction occurs when spacial thermal gradients exist in an object and heat can be transferred. The conductive heat flux can be calculated with Fourier's law given in equation 3.3. Fluxes are always in negative direction of the gradient.

$$\begin{aligned} \Phi_k &= -k A \nabla T \\ &= -k_1 A_1 \frac{\partial T}{\partial x_1} - k_2 A_2 \frac{\partial T}{\partial x_2} - k_3 A_3 \frac{\partial T}{\partial x_3} \end{aligned} \quad (3.3)$$

where $k = [k_1, k_2, k_3]$ is the thermal conductivity in $\text{W}/\text{m} \cdot \text{K}$, which is a characteristic material property. For isotropic materials, which means that material properties do not change with the relative direction, the thermal conductivity is a scalar, thus $k = k_1 = k_2 = k_3$. This is true for most pure metals and materials.

Although, if the thermal conductivity in one direction does not equal the others, the material is anisotropic and thermal conduction is a function of the direction within the material. For example, this occurs in layered structures or composite materials such as Carbon Fiber Reinforced Polymer (CFRP) or a PCB. For such materials the thermal conductivity must be known in all directions to ensure proper modeling. In the model conduction occurs within the PCB and between the components and the PCB.

3.2. Convection

Convection is heat transfer between a surface and its adjacent fluid, which is heated or cooled and subsequently carries energy away. In a vacuum convection has no effect, since there is no matter to which heat can be transferred to. Therefore, convection is not considered a potential thermal exchange mechanism when in space. For verification however, providing vacuum as experiment environment, for example by using a vacuum chamber, was infeasible. Additionally, natural convection and forced convection are distinguished. Forced convection occurs when there is fluid flow over the surface caused by external forces. In contrast, natural convection is caused by buoyancy forces, which occur when the density changes due to change in temperature. Thus, natural convection is modeled to assess the influence on test cases and to provide better results.

In general, the heat flux from or to an object by convection can be calculated with equation 3.4

$$\Phi_h = hA(T_W - T_\infty) \quad (3.4)$$

where h is the heat transfer coefficient, A is the area, T_W is the wall temperature and T_∞ is the temperature of the environment. Considering natural convection, values for the non-dimensional parameters Prandtl number, Rayleigh number and Nusselt number can be calculated with known material parameters. The heat transfer coefficient can then be deduced using correlations relating these non-dimensional parameters. Material parameters for the experiment environment are given in table 3.1 which were taken from [31].

Firstly, the Rayleigh number has to be calculated with equation 3.5. It describes the transition between laminar and turbulent flow.

$$Ra = \frac{g\beta(T_W - T_\infty)L^3}{\nu^2} \quad (3.5)$$

where g is the gravitational acceleration, ν is the kinematic viscosity, L is the characteristic length of the geometry and β is the coefficient of thermal expansion, which becomes $\beta = 1/T_\infty$ for ideal gases. At sea level the gravitational acceleration is $g = 9.81 \text{ m/s}^2$. Secondly, the Prandtl number has to be calculated with equation 3.6. It relates diffuse heat to impulse transport.

$$Pr = \frac{\nu}{a} \quad (3.6)$$

Tab. 3.1.: Properties for air at $T_\infty = 300$ K and $p_\infty = 100$ kPa [31].

Property	Symbol	Value and Unit
Density	ρ	1.161 kg/m ³
Thermal conductivity	k	2.62×10^{-2} W/m · K
Specific heat capacity	c_p	1007 J/kg · K
Thermal diffusivity	a	1.9×10^{-5} m ² /s
Kinematic viscosity	ν	1.6×10^{-5} m ² /s

where a is the thermal diffusivity k is the thermal conductivity of the fluid. The range of validity for the Prandtl number is $0.002 < Pr < 8000$. The Nusselt number, which relates Prandtl and Rayleigh numbers, can then be calculated with equation 3.7. It relates the convective transport to conductive transport in the boundary layer.

$$Nu = \begin{cases} Nu_0 + 0.668 K_f f(Pr) Ra^{0.25} & , 10^{-4} < Ra < 10^9 \\ 0.15 (f(Pr))^{4/3} Ra^{1/3} & , Ra > 10^9 \end{cases} \quad (3.7)$$

In the relevant experiments the sensor board was mounted vertically, which gives $L = H$, $K_f = 1$ and $Nu_0 = 0.68$. The correction factor for the Prandtl number is given in equation 3.8, which can be used in both cases.

$$f(Pr) = (1 + (2Pr)^{-9/16})^{-4/9} \quad (3.8)$$

Finally, the heat transfer coefficient can be calculated with equation 3.9, which requires the Nusselt number.

$$h = \frac{Nu \, k}{L} \quad (3.9)$$

There was no or negligible fluid flow in the experiment environment, which permits not including forced convection.

3.3. Radiation

Electromagnetic radiation is the mechanism which allows radiant energy transfer by photon exchange. Radiation does not require transfer of matter. In this regard it is an unique exchange mechanism and easily observable in reality, for example solar heat-up. Its nature and properties have been studies extensively in the past and are explained in the following sections.

3.3.1. Basic Quantities and Nomenclature

The energy of a photon Q in J , which is the carrier of radiant energy, is given in equation 3.10

$$Q_p = h\nu = \frac{hc}{\lambda} \quad (3.10)$$

where ν is the frequency in Hz, λ is the wavelength in m, $h = 6.626 \times 10^{-34} \text{ J} \cdot \text{s}$ is the Planck constant and $c = 2.998 \times 10^8 \text{ m/s}$ is the speed of light in vacuum. Photon energy is typically reported in units of electron volts (eV), which is the energy required to move an electron across a potential difference of 1 V, therefore 1 eV equals approximately $1.6 \times 10^{-19} \text{ J}$. As radiation often changes with respect to time, the radiant flux Φ is given in equation 3.11. Radiant flux is the derivation of radiant energy with respect to time, thus radiant power, and therefore has $\text{J/s} = \text{W}$ as unit.

$$\Phi = \frac{\partial Q}{\partial t} \quad (3.11)$$

where t is the time in s. Additionally, other dependencies can be expressed by derivation with respect to the property:

- Derivations with respect to the surface area $\partial/\partial A$ are helpful and the unit is expanded with $1/\text{m}^2$.
- Derivations with respect to wavelength $\partial/\partial \lambda$ yield spectral quantities denoted with a λ as subscript. The unit is expanded with $1/\text{nm}$ as the wavelength is measured in nanometers.
- Derivations with respect to solid angle $\partial/\partial \Omega$ give radiant quantities denoted with a Ω as subscript. A $1/\text{sr}$ is added to the unit because the solid angle is measured in steradians.

In table 3.2 the important radiometric quantities and their properties are again summarized. Note that emittance and irradiance have the same units but different directions, meaning irradiance is energy transfer towards a surface while emittance is energy transfer from a surface.

3.3.2. Planck's Law, Wien's Law and the Stefan-Boltzmann Law

Every object emits thermal radiation dependent on its temperature. The law, which was first developed by Max Planck in 1900 (therefore referred to as "Planck's Law") and which marks the begin of quantum physics, describes the spectral radiance of a black body as a function of its temperature. It is given in equation 3.12 [29].

$$B(\lambda, T) = \frac{c_1}{\lambda^5 (\exp(c_2/\lambda T) - 1)} \quad (3.12)$$

Tab. 3.2.: Radiometric terminology and units.

Quantity with Symbol	SI Unit	Description
Radiant energy Q	J	Thermal energy \ heat
Radiant flux Φ	W	Radiant energy per unit time
Emittance \ irradiance M	W/m ²	Power emitted \ received per surface
Spectral emittance \ irradiance M_λ	W/m ² · nm	Power emitted \ received per surface per wavelength
Radiant intensity I_Ω	W/sr	Power per unit solid angle
Radiance L_Ω	W/m ² · sr	Power per unit solid angle per surface area
Spectral radiance $L_{\lambda,\Omega}$	W/m ² · nm · sr	Power per unit solid angle per surface area per wavelength

where T is the objects temperature in K. The constants c_1 and c_2 are given in equation 3.13 and 3.14, respectively.

$$c_1 = 2\pi hc^2 = 3.742 \times 10^{-16} \text{ W/m}^2 \quad (3.13)$$

$$c_2 = \frac{hc}{k_B} = 1.439 \times 10^1 \text{ m} \cdot \text{K} \quad (3.14)$$

where $k_B = 1.381 \times 10^{-23} \text{ J/K}$ is the Boltzmann constant. Be aware that in equation 3.13 the object is assumed to be diffuse and thus the Lambertian Law $M_\lambda = \pi L_\lambda$ can be applied. If the object can not be taken as diffusely radiating, the factor π has to be removed from equation 3.13 and the integrals in equation 3.15 have to be evaluated [29].

$$B(\lambda, T) = \int_{\varphi=0}^{2\pi} \int_{\beta=-\pi/2}^{\pi/2} L_{\lambda,\Omega}(\lambda, T) \cos \beta \sin \beta \, d\beta d\varphi \quad (3.15)$$

where $L_{\lambda,\Omega}$ is the spectral radiance in W/m² · nm · sr, φ is the azimuthal angle in rad and β is the elevation angle in rad (see figure 3.3).

Another valuable law when considering radiative heat transfer is Wien's displacement law [30]. It is given in equation 3.16 and relates the maximum wavelength λ_{max} in nm of a black body's radiation to its temperature T in K.

$$\lambda_{max} = \frac{b}{T} \quad (3.16)$$

where the proportionality constant $b = 2.898 \times 10^{-3} \text{ m} \cdot \text{K}$ is Wien's displacement constant. This law is especially helpful when determining in which waveband an object is emitting radiation.

Additionally, Josef Stefan and Ludwig Boltzmann each individually derived the law nowadays known as Stefan-Boltzmann law from Planck's law. Stefan and

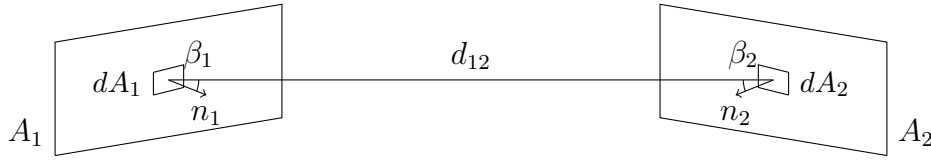


Fig. 3.1.: Geometric Quantities for View Factor Calculation

Boltzmann discovered that the radiant emittance of a black body with unit surface area is proportional to the fourth power of its temperature, see equation 3.17.

$$\Phi = A\sigma T^4 \quad (3.17)$$

where $\sigma = 5.67 \times 10^{-8} \text{ W/m}^2 \cdot \text{K}^4$ is the Stefan-Boltzmann constant.

3.3.3. Radiant Heat Transfer

The previous section's laws consider black bodies, which are an abstraction of reality. Incident radiation is not necessarily absorbed equally for all wavelength.

$$\Phi_{r,in} = A_1 F_{12} \int_0^\infty \alpha_\lambda M_{in,\lambda} d\lambda \quad (3.18)$$

Radiative power incident on an surface is dependent on its size A_1 , view factor F_{12} , spectral absorptivity α and the spectrum of incident radiation M_S . Besides, real radiations can emit power differently for different wavelength. They are called gray radiators with absorptivity α and emissivity ε . Furthermore, heat exchange is always mutual between bodies. For two bodies forming an enclosure equation 3.19 states how the heat flux between these two bodies can be calculated.

$$\Phi_{r,12} = \int_0^\infty \frac{B(\lambda, T_1) - B(\lambda, T_2)}{\frac{1-\varepsilon_{\lambda,1}}{A_1 \varepsilon_{\lambda,1}} + \frac{1}{A_1 F_{12}} + \frac{1-\varepsilon_{\lambda,2}}{A_2 \varepsilon_{\lambda,2}}} d\lambda \quad (3.19)$$

Here, ε is the emissivity and A is the surface area of the respective body. With the assumption that $A_1 \ll A_2$ equation 3.19 can be simplified to yield equation 3.20.

$$\Phi_{r,12} = A_1 F_{12} \int_0^\infty \varepsilon_\lambda (B(\lambda, T_1) - B(\lambda, T_2)) d\lambda \quad (3.20)$$

If for emission in the IR waveband the emissivity can be assumed to be constant, equation 3.20 can be simplified using the Stefan-Boltzmann law, gaining equation 3.21.

$$\Phi_{r,12} = A_1 F_{12} \sigma \varepsilon (T_1^4 - T_2^4) \quad (3.21)$$

View factors for different geometric constellations, spectra, emissivity and absorptivity are discussed in the following sections.

3.3.4. Photometric Law and View Factors

For electro-magnetic radiation the distance from the source and the orientation of both the emitting and the receiving surface are important for the determination of the radiant flux between them. Equation 3.22 states the photometric law and figure 3.3.4 depicts a basic graphical representation. The radiant flux decreases with the square of the distance between the surfaces, if there is no attenuation of radiation. In figure 3.1 the geometric properties for calculation of radiant fluxes between two surfaces are given.

$$d^2\Phi_{12} = L_1 \frac{\cos \beta_1 \cos \beta_2}{d_{12}^2} dA_1 dA_2 \quad (3.22)$$

Assuming surface A_1 to be a Lambertian radiator, its emitted heat flux to the half space is given in equation 3.23.

$$\Phi_1 = \pi A_1 L_1 \quad (3.23)$$

With this quantity, the ratio of heat flux emitted from surface A_1 to heat flux incident on surface A_2 is the view factor F_{12} . Figure 3.1 shows the geometric quantities, which are required for calculation of the view factor with equation 3.24. The angles β_1 and β_2 are measured between the respective surface normals (n_1 and n_2) and the distance vector d_{12} connecting dA_1 and dA_2 .

$$F_{12} = \frac{\Phi_{12}}{\Phi_1} = \frac{1}{\pi A_1} \int_{A_1} \int_{A_2} \frac{\cos \beta_1 \cos \beta_2}{d_{12}^2} dA_1 dA_2 \quad (3.24)$$

One should be aware, that equation 3.24 is only valid for diffuse, homogeneous emitting surfaces A_1 . This assumption was made for radiation emitted from Earth, both in the infrared waveband and for albedo. Furthermore, there are useful relationships between view factors, which can help simplifying their calculation.

- For a fully surrounded surface the radiation balance yields that the view factors to all distinct visible surfaces A_i with $i \in [1, n]$ have to add up to unity, $\sum_{j=1}^n F_{ij} = 1$.
- Flat and convex surfaces A_i do not see themselves, thus $F_{ii} = 0$.
- The reciprocity law, $A_1 F_{12} = A_2 F_{21}$, defines the connection between two view factors. This relationship is helpful because only one view factor has to be calculated as long as the two involved surfaces are known.

For numerous geometries the view factors are given in various literatures and view factors for relevant geometries are described hereafter [29, 30, 32].

Firstly, radiative heat exchange happens with the Sun, which can be assumed to be a single radiant heat source far away from Earth. Irradiance is therefore only a function of the irradiation angle. Although, if the view from the spacecraft to the Sun is obstructed by Earth, there is no irradiance on the sensor. The

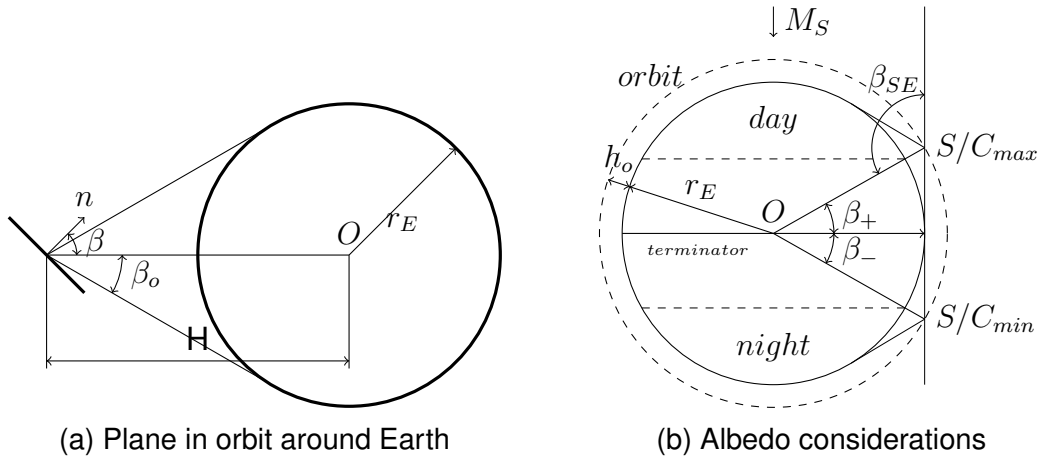


Fig. 3.2.: Symbolic view factor geometry: a) For a satellite in orbit around Earth, b) For estimation of the albedo shares over an orbit.

formula for calculation of the view factor of an object irradiated by the Sun is given in equation 3.25. The cases are

$$F_{sat,S} = \begin{cases} \cos \beta_S & , \text{ if visible} \\ 0 & , \text{ if not visible} \end{cases} \quad (3.25)$$

Secondly, the view factor of Earth for an object in orbit around it is more complex to calculate. Again, figure 3.2a depicts the basic setup for calculating this property. The bold line represents an area increment of the orbiting objects surface with surface normal n and the circle represents Earth with radius r_E . The distance of the object from the center of Earth is denoted with H , while the angle between the surface normal n and the nadir direction is denoted β_E . Only one side of the area increment is considered because the object is assumed to have a volume and not to consist of only a plane floating around Earth. When calculating the view factor for Earth, a distinction between the formulas with respect to the angle has to be made because it is possible that for certain angles Earth is only partially visible or even not at all. Equation 3.26 shows the formulas and distinctions with $h = H/r_E$, $x = \sqrt{h^2 - 1}$ and $y = -x \cot \beta_E$ [32].

$$F_{sat,E} = \begin{cases} \frac{\cos \beta_E}{h^2} & , \text{ if } |\beta_E| \leq \arccos(1/h) \\ 0 & , \text{ if } |\beta_E| + \arccos(1/h) \geq \pi/2 \\ \frac{1}{\pi h^2} \left(\cos \beta_E \arccos y - x \sin \beta_E \sqrt{1 - y^2} \right) + \frac{1}{\pi} \arctan \left(\frac{\sin \beta_E \sqrt{1 - y^2}}{x} \right) & , \text{ otherwise.} \end{cases} \quad (3.26)$$

In contrast to the Sun's view factor, Earth is still visible when the Earth angle is above 90° . Figure 3.4a shows the view factor of Earth for different orbit heights.

Thirdly, the view factor for albedo radiation, which is solar radiation reflected back to space by Earth, has to be established. Albedo radiation comes in the

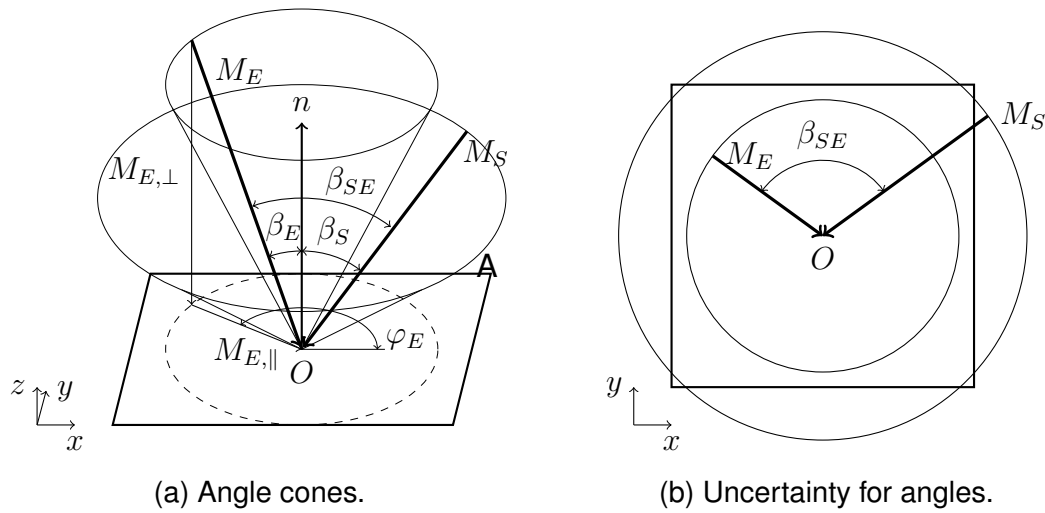


Fig. 3.3.: Cones of angles for Earth β_E and Sun β_S : a) View from the side, b) View from above. Geometric description of irradiance by vector $[\beta \ \varphi \ M]^T$.

direction of Earth β_E and thus has the same base view factor as infrared radiation. This is an assumption but other modeling approaches did not yield better results. Although, not the entire Earth must reflect solar radiation, as only half of Earth is illuminated at one time. The boarder between sunlit area and night is called the terminator. Which part of Earth is illuminated at what time is a function of the Sun angle β_S on Earth and to account for this the albedo factor ξ is introduced, as given in equation 3.27.

$$F_{sat,A} = \xi F_{sat,E} \quad (3.27)$$

The factor ranges from zero to unity ($\xi \in [0, 1]$) and describes the share of visible Earth surface, which is illuminated by sunlight. In figure 3.3a a geometric representation of the angles is given. The cones correspond to the angles of the respective radiation. As they can be anywhere on the cone, the angle between incident solar radiation and radiation from Earth can range from zero to pi ($\beta_{SE} \in [0, \pi]$), which is better visible in figure 3.3b. This ambiguity clarifies that the introduction of a new parameter is necessary.

$$\beta_o = \arccos\left(\frac{r_E}{H}\right) \quad (3.28)$$

For determining the albedo, it is interesting to know, whether the terminator is in the view field. If the terminator is rarely visible, modeling only full albedo and no albedo might be reasonable. As visible in figure 3.2b, the terminator is within the field of view as long as the angle is within $[\beta_-, \beta_+]$. A patch of a sphere's surface is given as $dA = r^2 \sin \varphi \, d\varphi \, d\theta$ and integration yields the total surface area of $A_{sphere} = 4\pi r^2$

$$\begin{aligned} A_{term}(\beta) &= \int_0^{2\pi} \int_{-\beta}^{\beta} r_E^2 \sin \varphi \, d\varphi \, d\theta \\ &= 4\pi r_E^2 \sin \beta \end{aligned} \quad (3.29)$$

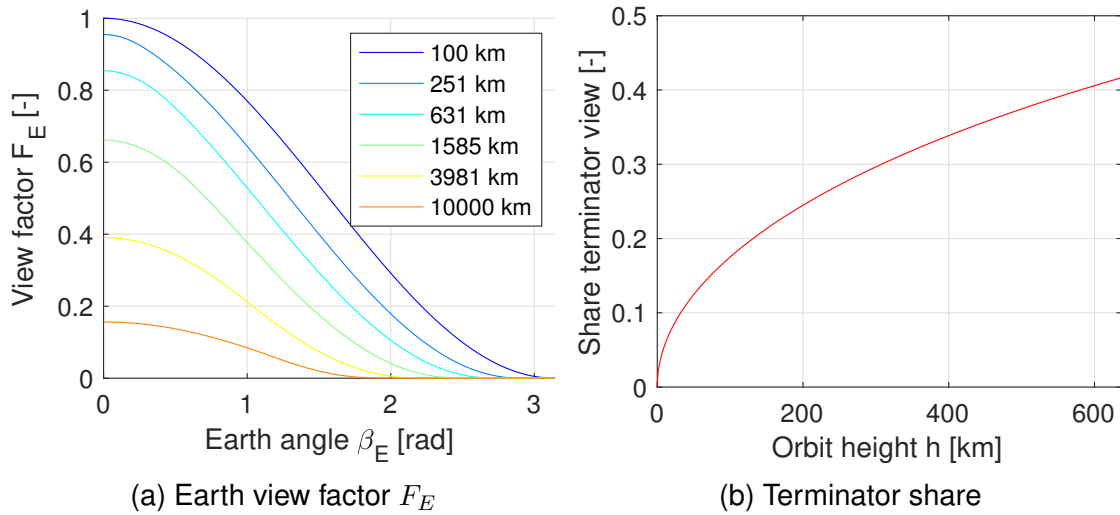


Fig. 3.4.: Orbit Geometry: a) View factor of Earth for different orbit heights, b) Share of positions with terminator visible.

$$\frac{A_{term}(\beta_o)}{A_{sphere}} = \sqrt{\left(1 - \frac{r_E^2}{H^2}\right)} \quad (3.30)$$

Figure 3.4b shows this share of positions for which the terminator is visible for different orbit heights following equation 3.30. It is 0.34 for Earth's radius 6370 km and a typical LEO height of 400 km. This means that 34 % of all possible positions of a satellite see the terminator and therefore both day and night. The lower the satellite's orbit height is, the smaller this share becomes.

Fourthly, for most applications emission towards the Cosmic Microwave Background (CMB) is important. The temperature of the CMB is $T_{CMB} = 2.725$ K [33]. Fulfilling the requirement, that for a geometry the view factors to all visible objects have to add up to unity, the view factor for radiation against the CMB can be derived. By geometric reasoning, the albedo is part of Earth and must not be taken into account. Sun is also regarded to have a small apparent radius [17]. Thus, $F_{sat,CMB} + F_{sat,E} = 1$.

3.3.5. Reflectance, Transmittance, Absorptivity and Emissivity

The surface material has a major impact on radiant heat exchange. An incoming photon of a certain wavelength can either be absorbed, transmitted or reflected, whilst the material emits photons. These properties change with the photon's wavelength and the surfaces are called selective. Energy conservation states that for each wavelength λ spectral absorptivity α_λ , spectral transmittance τ_λ and spectral reflectance ϱ_λ sum up to one, see equation 3.31.

$$\alpha_\lambda + \tau_\lambda + \varrho_\lambda = 1 \quad (3.31)$$

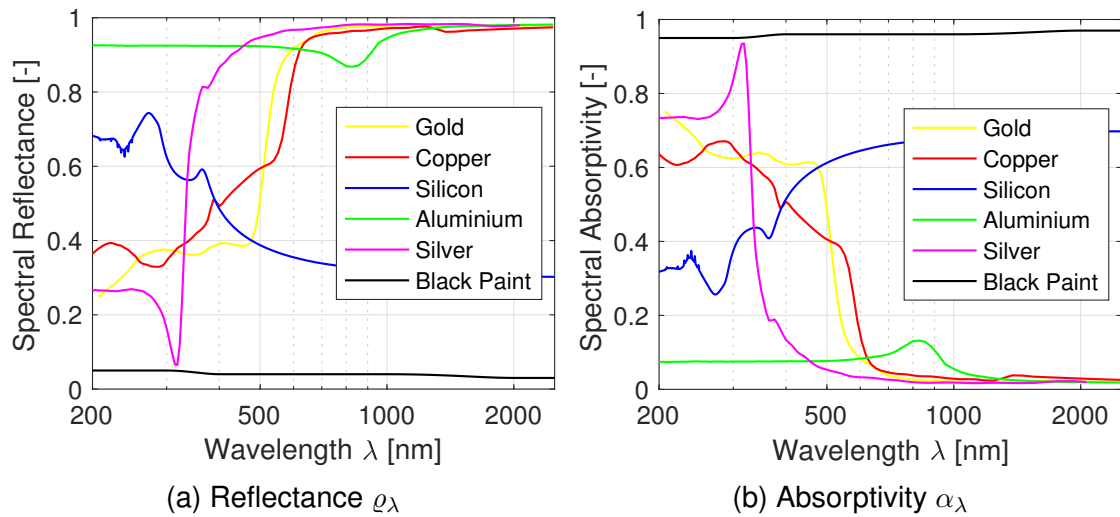


Fig. 3.5.: Spectral surface properties for various materials for solar wavelengths: a) Reflectance, b) Absorptivity. [34].

Transmittance can be neglected because in the considered waveband the materials are assumed nontransparent ($\tau = 0$). Thus, an incoming photon can either be absorbed or reflected, yielding $\alpha_\lambda + \rho_\lambda = 1$. Furthermore, Kirchhoff's law of thermal radiation, given in equation 3.32, links spectral absorptivity to spectral emissivity.

$$\alpha_\lambda = \varepsilon_\lambda \quad (3.32)$$

Determination of these material properties is not trivial and requires extensive effort. Reflectance data for numerous materials is given in the CRC Handbook of Chemistry and Physics [34]. The photon's energy in eV and the spectral reflectance, which is dimensionless, are given. In figure 3.5a, spectral reflectance curves for various materials are plotted. Spectral reflectance for black paint has been modeled based on [35]. The absorptivity for these materials has also been calculated using equation 3.31. Figure 3.5b depicts the calculated absorptivity curves.

3.3.6. Solar Irradiation

The most important source of radiant energy in an orbit around Earth is the Sun. Numerous measurements of the solar radiation's spectrum have been performed over time [36, 37]. They form the basis of the ASTM E-490-00 solar spectrum standard, which is distributed online and plotted in figure 3.6 [38]. This spectrum will be referred to as $M_{\lambda,S}$ and it has been used as reference solar radiation spectrum. In figure 3.6, Air Mass Zero (AM0) denotes that the spectrum is solar radiation outside Earth's atmosphere. Increasing AM values correspond to increasing atmospheric absorption. Another standard for solar irradiance is the ASTM G-173-3 solar spectrum [39], which includes direct and

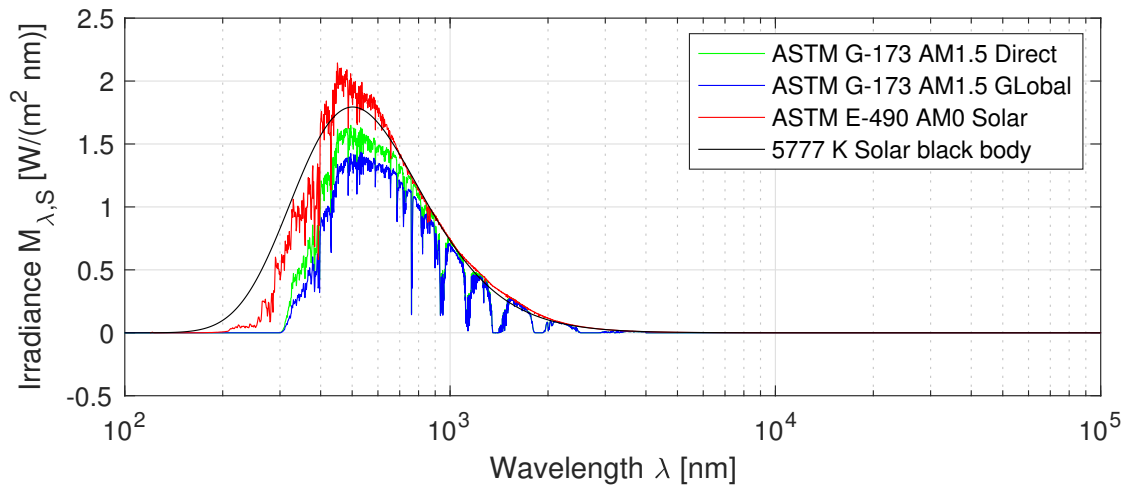


Fig. 3.6.: ASTM International standards for spectral solar irradiance at space (ASTM E-490-00, AM0) and ground (ASTM G-173, AM1.5 Direct and Global) and 5777 K solar black body spectral irradiation.

global spectra for earth's surface at AM1.5. These are also plotted in figure 3.6.

$$M_S = \left(\frac{r_S}{d_{S,E}} \right)^2 \int_0^\infty M_{\lambda,S}(\lambda, T_S) d\lambda = 1367 \text{ W/m}^2 \quad (3.33)$$

The integration in equation 3.33 over all wavelengths yields the solar constant M_S at a distance of $d_{S,E} = 1 \text{ au} = 1.496 \times 10^{11} \text{ m}$, which is the astronomical unit. The solar spectrum can be assumed temporally constant, since variation in measurements of the solar luminosity with the Active Cavity Radiometer Irradiance Monitor 1 (ARCIM-1) instrument aboard the Solar Maximum Mission from 1980 to 1989 are below 0.1 % [40]. Using the solar constant, a corresponding black body temperature of Sun's surface can be deviated by solving equation 3.33 for T_S . Here $r_S = 6.963 \times 10^8 \text{ m}$ is the Sun's radius and $d_{S,E} = 1 \text{ au}$. It gives $T_S = 5777 \text{ K}$ and this value is also given in the National Aeronautic and Space Agency (NASA) Sun fact sheet [41]. Additionally, the solar black body spectral irradiance is plotted in figure 3.6.

3.3.7. Earth's Albedo

Albedo radiation is the amount of irradiation which is reflected back into space by both atmospheres and surfaces [42]. All celestial bodies emit albedo radiation as all objects reflect radiation albeit with different shares. Earth's albedo from Solar irradiation is highly variable and hard to predict [43]. Some parameters influencing the albedo are:

- Surface material: Spectral reflectance is a material specific property, which greatly varies for different materials. For example, snow has significantly higher reflectance than tarmac. Local differences and seasonal changes

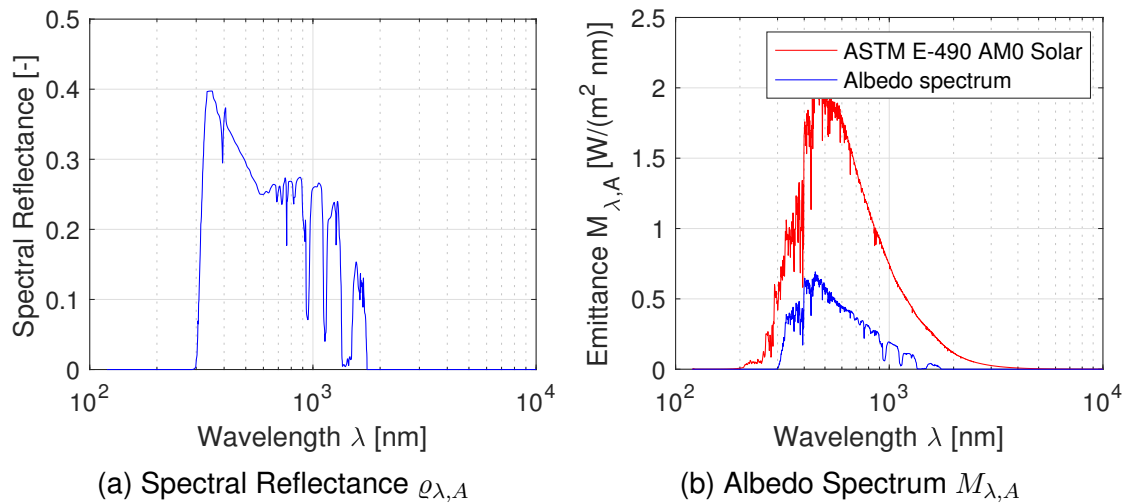


Fig. 3.7.: Spectral albedo data: a) Annual and hemispherical averaged reflectance of Earth's surface, b) ASTM E-490-00 spectral solar irradiance and resulting spectral albedo with reflectance from a).

in the surface material influence the reflectance and subsequently the albedo.

- **Atmosphere:** The thickness and composition of the atmosphere influences the albedo. Certain gases, such as carbon dioxide CO_2 , methane CH_4 , ozone O_3 or water vapor H_2O , absorb or reflect radiation and complicate the radiation exchange. Also the thicker the atmosphere, the more solar radiation can be absorbed or reflected.
- **Clouds:** The ratio of Earth's sunlit surface covered with clouds is also a major factor for reflectance. Clouds reflect sun light to a high degree, which greatly influences the albedo share.

In figure 3.7 data for albedo modeling is given. Annual, norther-hemispherical average reflectance is plotted in figure 3.7a [19]. It describes the ratio of spectral emittance of Earth to solar spectral irradiance on Earth, as given in equation 3.34.

$$\rho_{\lambda,A} = \frac{M_{\lambda,A}}{M_{\lambda,A}} \quad (3.34)$$

With an average value of 30% it lies well within the boundaries given by [43]. The resulting spectrum is given in figure 3.7b, alongside the reference solar spectrum.

3.3.8. Earth's Infrared Emission

As previously mentioned, all object emit thermal radiation depending on their temperature and so does Earth. Assuming Earth as a black body and averaging over time, Earth's mean black body temperature can be calculated by solving equation 3.35 for $T_E = 279 \text{ K}$, which states an energy balance between solar

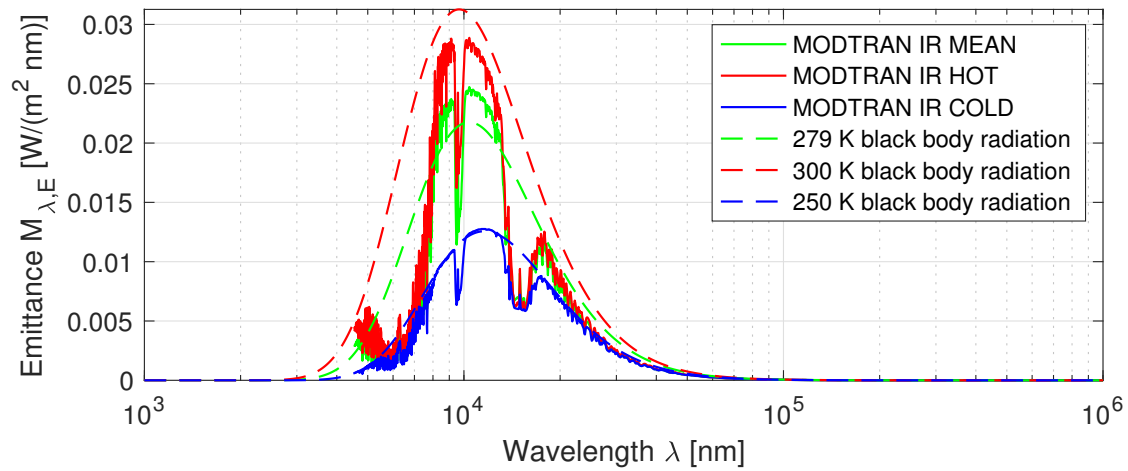


Fig. 3.8.: MODTRAN Earth IR emittance simulations for different scenarios: Hot for tropical atmosphere, mean for standard atmosphere and cold for subarctic winter. For reference, black body radiation curves for different temperatures are plotted.

irradiance on the projected surface of Earth πr_E^2 and Earth's radiant emittance from its entire surface $4\pi r_E^2$.

$$\pi r_E^2 M_S = 4\pi r_E^2 \int_0^\infty M_{b,\lambda}(\lambda, T_E) d\lambda \quad (3.35)$$

Though, in reality the assumptions for a steady state black body Earth do not hold [43]. IR radiation from Earth depends on numerous highly complex parameters. Amongst these parameters are:

- **Ground:** The ground temperature is not uniform over time or location, thus the emittance varies. For example, the emittance of high temperature desert ground at the equator is higher than the emittance of low temperature tundra at higher latitudes. Also, fluctuations in ground temperature may vary from point to point due to locally different thermal inertia.
- **Atmosphere:** The atmosphere selectively absorbs radiation of specific wavelengths and is transparent to other radiation. This decreases the emittance at the respective wavelengths. Since the composition of the atmosphere is not constant, the share of absorbed radiation changes as well.
- **Clouds:** Clouds reflect and absorb IR radiation similarly to Solar radiation. When and where clouds may appear can not be predicted today but only statistically approximated.

For this project, Moderate Resolution Atmospheric Transmission (MODTRAN) has been used. MODTRAN is a code for prediction of spectral radiation propagation through Earth's atmosphere under various constraints [44]. The simulated spectral infrared emittance has been taken as approximation for Earth's IR emittance $M_{\lambda,E}$ [45]. Results are plotted in figure 3.8 and their respective

Tab. 3.3.: MODTRAN 5 locality input parameters for different scenarios.

Scenario	Locality	Cloud Scenario
Mean	1976 U.S. Standard Atmosphere	No clouds or rain
Hot	Tropical Atmosphere	No clouds or rain
Cold	Subarctic Winter	Altostratus Cloud Base 2.4 km Top 3.0 km

settings in the MODTRAN code are given in table 3.3. Attitude parameters, which were used for all simulation with the MODTRAN version 5, were an altitude of 100 km and ‘Looking down’ direction. The altitude has been chosen to correspond to the Kármán line, commonly taken as the boarder of space. For comparability, atmosphere parameters and temperature offset have not been altered.

Figure 3.8 also presents black body spectral emittance curves for the temperatures associated with the respective spectrum. Integration of the modeled spectrum over the wavelength yields a radiant emittance of $M_E = 267.88 \text{ W/m}^2$ at 100 km height above Earth’s surface. Additionally, the factors for view factor calculation with equation 3.26 have to be adjusted, since the result of MODTRAN is at a height of 100 km above the surface of Earth. The sphere’s radius r_E has to be increased by 100 km, while the orbit height h_o has to be decreased by the same amount. For reference see figure 3.2.

4. Photometry

The photodiode will be used to detect by how much the sensor is irradiated from both the Sun and Earth's albedo. Therefore, a model is developed which relates irradiance and incident angle to the photocurrent. As photodiode a Vishay BPW 34 PIN silicon photodiode has been selected and the circuit has been designed to operate in short circuit mode, which minimizes the effect of reverse dark current [46].

4.1. Spectral and Radiant Sensitivity

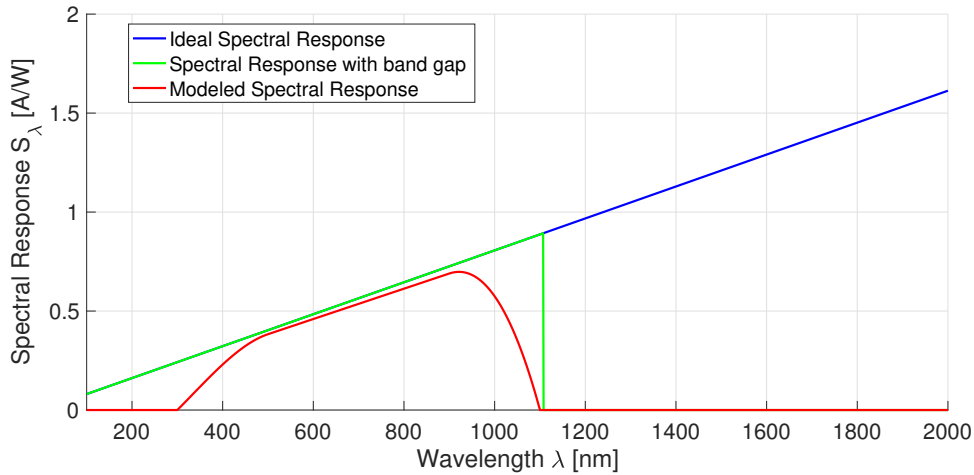


Fig. 4.1.: Ideal and modeled spectral sensitivity for silicon semiconductors of 250 μm thickness.

This section is supposed to explain how irradiation causes a photocurrent in a silicon photodiode depending on the irradiation's spectrum and the angle of incidence.

The energy of n_p photons at wavelength λ is $E_{p,N} = n_p E_p(\lambda)$, as stated in equation 3.10. The photons interact with the silicon's electrons and cause a photocurrent I_p following equation 4.1

$$I_p = qn_q \quad (4.1)$$

where n_q is the number of charge carriers and $q = 1.602 \times 10^{-19} \text{ C}$ is the elementary charge. The relation between the photon's energy and the photocurrent is the spectral sensitivity S_λ as defined in equation 4.2 [47]

$$S_\lambda(\lambda) \equiv \frac{I_p}{E_{p,n}} = \eta(\lambda) \frac{q\lambda n_q}{hcn_p} = \eta(\lambda) \frac{q}{hc} \lambda \quad (4.2)$$

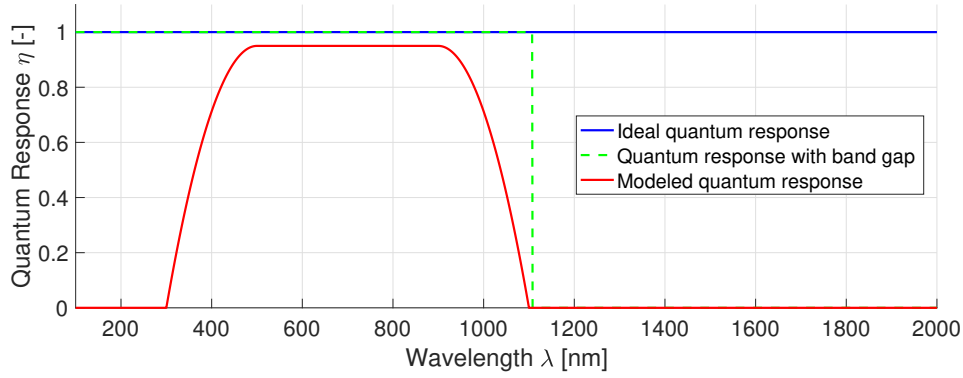


Fig. 4.2.: Ideal and modeled quantum response for silicon semiconductors of 250 μm thickness.

where η is the dimensionless quantum efficiency. Its unit is A/W and an ideal spectral sensitivity curve as well as an empiric model have been plotted in figure 4.1. The number of photons n_p and the number of charge carriers n_q cancel out, because in this model one photon can only excite one electron. Introduction of quantum efficiency in equation 4.2 is necessary because the conversion from irradiance to current is neither perfect nor constant over the wavelength. The modeled quantum efficiency has been designed on the following assumptions, which are empirically based on the absorption and penetration depth versus wavelength graph in [48]. Both ideal and modeled quantum efficiency are plotted in figure 4.2.

- The maximum efficiency has been set to $S_{\lambda, \max} = 0.95$. Radiation is not entirely absorbed, some share is reflected.
- At small wavelengths (300 nm – 500 nm) the penetration depth is low and recombination effects appear near the surface reducing the quantum efficiency.
- At longer wavelength (900 nm – 1100 nm) the absorptivity is reduced and so the quantum efficiency is decreased.
- The band gap of silicon is at $E_g = 1.12 \text{ eV}$ at 273 K, above which the photodiode is practically insensitive to radiation and the quantum efficiency is zero. The band gap's wavelength is $\lambda_g = \frac{hc}{qE_g} = 1107 \text{ nm}$.

Besides the spectral sensitivity, the current produced by the photo diode also depends on the radiation's incident angle. Irradiation generates the maximum photocurrent when parallel to the surface normal. Experiments show that there are differences comparing photo diode's angle dependency to the standard view factor dependency in equation 3.25. For photo diodes the current decreases slower for angles close to the normal direction and faster for big angles from the normal. The radiant sensitivity S_θ has been modeled according to equation 4.3.

$$S_\theta = (\cos \beta)^{0.4} \quad (4.3)$$

where β is the incident angle from the normal (see figure 3.3a).

With a spectral irradiance M_λ , such as solar irradiation, the resulting photocurrent can be calculated by integrating the product of spectral irradiance and spectral response over all wavelengths and multiplying it with the diode's radiant sensitive area as given in equation 4.4.

$$I_r = A_{PD} S_\theta \int_0^\infty S_\lambda \cdot M_\lambda d\lambda \quad (4.4)$$

where A_{PD} is the photo diode's radiation sensitive area.

4.2. Amplification and Analog to Digital Conversion

The micro controller can only measure voltage which has a relative magnitude compared to its internal reference voltage in the range of its resolution. Furthermore, the measurements have to be transformed from analog signals to digital readings. Analog to digital conversion turns the measurement discrete values, for both time and magnitude. Although, the current from the photo diode has to be converted to a voltage and amplified at first. For the TOSS, a two step conversion and amplification process has been chosen. The first stage transimpedance amplifier converts the current into voltage and amplifies it. The second stage is a non-inverting amplifier. Converting the measurement has been performed by the internal Analog Digital Converter (ADC) with $N = 10$ bit resolution and an internal reference voltage of $U_{ref} = 2.56$ V. An offset in the ADC of $n_{offset} = +25$ is present, which has to be added onto simulation or subtracted for measurements. This is necessary, because the reading from the photo diode may not be zero for no incident radiation. With these known parameters, conversion between measurement and ADC value n_{ADC} can be done with equation 4.5.

$$n_{ADC} = \frac{2^N G}{U_{ref}} I_{PD} - n_{offset} \quad (4.5)$$

The system's gain G can be calculated with equation 4.6 as the two amplification steps are in series, with $G_1 = R_7$ and $G_2 = 1 + R_6/R_8$.

$$G = R_7 \left(1 + \frac{R_6}{R_8} \right) \quad (4.6)$$

Doing the calculation with values for the resistances from the circuitry diagrams C.4 and C.5, the gain of the transimpedance amplifier system is $G = 50$ V/A.

5. Model Geometry and Parameters

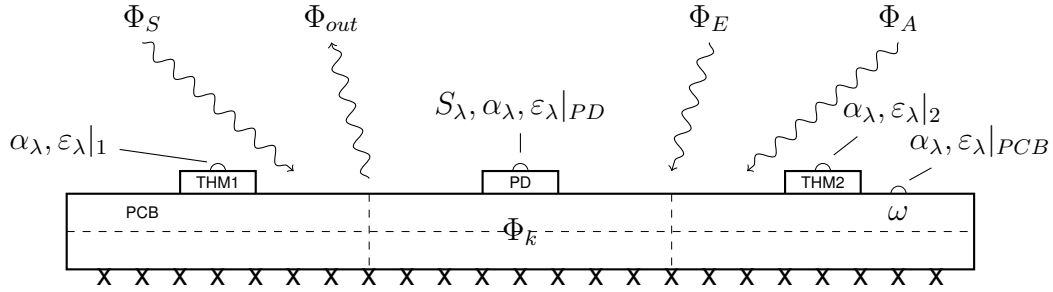


Fig. 5.1.: Thermal exchange mechanisms and surface properties.

The different sensor boards present have been modeled to simulate thermal behavior and to make predictions on the sensitivity of design parameters. The geometric properties of the sensor must be known to model it properly. Areas are necessary for calculating heat fluxes and volumes are required for calculating thermal states and temperature gradients. The thermal model resembles the geometric model with the geometric elements all being an individual thermal node. Therefore, each element is regarded to be of uniform temperature. Heat may flow between adjacent elements.

$$\rho_i c_i V_i \frac{\partial T_i}{\partial t} = \sum_{adj} A_j \Phi_j + \omega_i \quad (5.1)$$

For each volume element represented by a thermal node V_i , the change in its temperature T_i can be calculated with equation 5.1. The values of density ρ_i and specific heat capacity c_i are chosen to resemble the material of the modeled material or a compound. It is assumed that they are spatially constant as well as to temperature. Heat fluxes Φ_i are calculated with equations from the heat transfer chapter 3 with the model's geometric dimensions. Considering all fluxes, the differential equation for the temperature 5.1 can also be written as:

$$\begin{aligned} \rho c V \frac{\partial T}{\partial t} = & F_S A_r \int_0^\infty \alpha_{S,\lambda} M_{S,\lambda} d\lambda \\ & + F_A A_r \int_0^\infty \alpha_{S,\lambda} M_{A,\lambda} d\lambda \\ & + F_E A_r \int_0^\infty \alpha_{IR,\lambda} M_{E,\lambda} d\lambda \\ & - F_E A_r \varepsilon \sigma (T^4 - T_E^4) \\ & - (1 - F_E) A_r \varepsilon \sigma (T^4 - T_{CMB}^4) \\ & + \omega \\ & + \Phi_k \\ & (+ \Phi_h) \end{aligned} \quad (5.2)$$

When solving for the temperature T , all shares have to be determined.

5.1. TOSS v2.2 Model

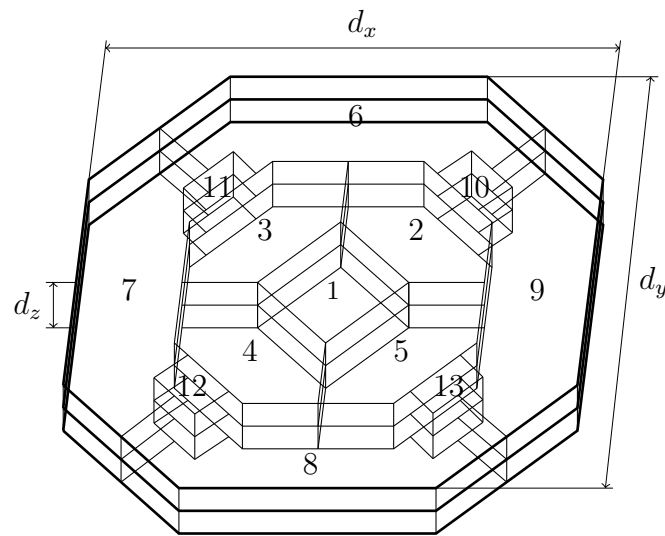


Fig. 5.2.: Geometric model of a TOSS v2.2 sensor board for volume and area calculations. The numbers are the index of the corresponding thermal node in the upper layer, see figure 5.3a.

The TOSS v2.2 sensor board is of octagon shape (see figure 2.3b). The dimensions indicated in figure 5.2 are $d_x = d_y = 70$ mm and $d_z = 3$ mm. As described in chapter 2, it features four DS18B20U thermometers and nine BPW34 diodes together with the necessary electronics. The PCB below the thermometers is cut out to reduce conductivity and the thermometers are soldered on the PCB. The photo diodes on the rim of the sensor board are orientated with the normal vector horizontally and are soldered to the sensor's upper surface comparable to Surface-mounting Technology (SMT) devices. In contrast, the central photo diode is soldered facing upward with Through-hole Technology (THT). Figure 5.2 depicts how the sensor's PCB has been divided into several volume elements and figures 5.3a and 5.3b show how the volume elements are connected. All in all, the model consists of 43 nodes.

As both figures 5.3a and 5.3b only give a limited insight into the model, table 5.1 notes the indices of all nodes and the volume element they represent. Components include the microcontroller, the ADC, multiplexer and various small resistors.

Tab. 5.1.: Number and respective volume element of all nodes in the TOSS v2.2 model.

Nodes	1 - 26	27 - 35	36 - 39	40 - 43
Element	PCB	PD	THM	Components

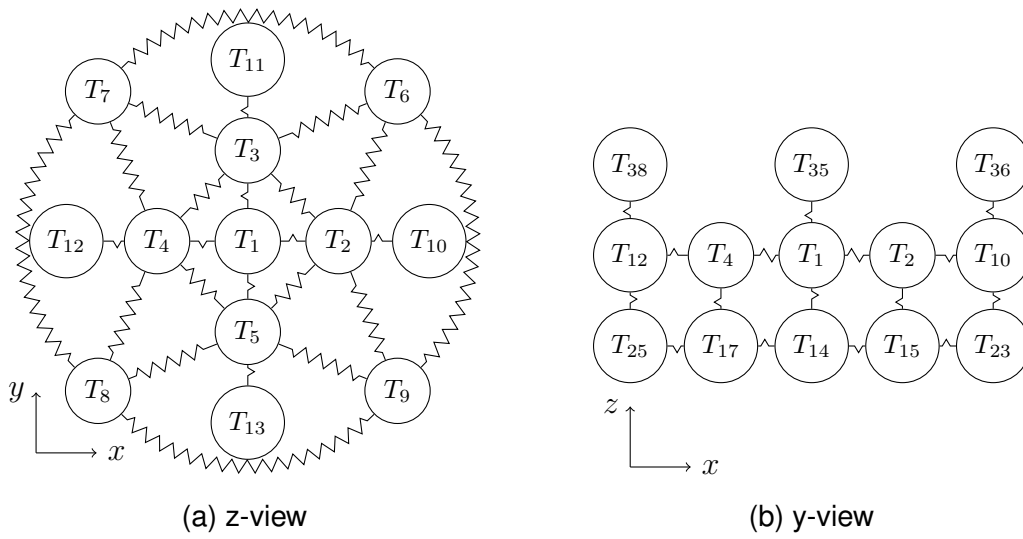


Fig. 5.3.: Thermal model of a TOSS v2.2 sensor board for heat flux calculation: Thermal nodes displayed as circles with their respective index and thermal conductivity resistances connecting them displayed as zigzag lines: a) View in $-z$ -direction on top layer, b) Cut through the model view in $+y$ -direction with nodes for thermometers and the photodiode.

5.2. TOSS v3 Model

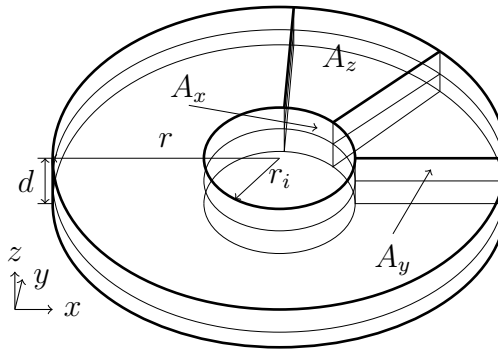


Fig. 5.4.: Geometric model of a TOSS v3.0 sensor board for volume and area calculations.

The TOSS v3.0 board is circular with an outer radius r and a thickness d (see figure 2.3c). It has been divided into eighteen elements, two levels with equal thickness of nine each. Eight elements in one layer are circularly distributed around one center element. All elements have the same volume and thus have equal surface areas in z -direction $A_z = \pi r^2/9$. The inner radius can be calculated to $r_i = r/3$. The area from the inner volume element to the outer ring A_r is calculated with $A_x = \pi d r_i/24$, whereas the area between two elements on the outer ring is $A_y = d r/3$. In figure 5.4 the sensor is displayed symbolically, although only two outer ring elements of each layer are displayed for better visibility.

Other components, which may be placed on either side of the board, are considered to be of box like shape and to be in contact with only one adjacent volume element. The nodes representing the two thermometers are connected to node 1 and 5. Additionally, the photo diode is connected to node 9 in the upper layer. Table 5.2 denotes which node represents which thermal element.

Tab. 5.2.: Number and respective volume element of all nodes in the TOSS v3 model.

Nodes	1 - 18	19 - 20	21
Element	PCB	THM	PD

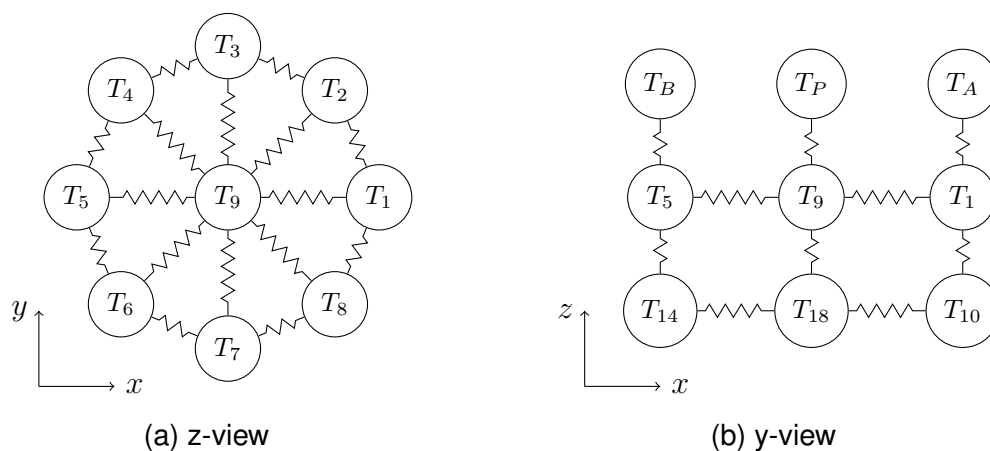


Fig. 5.5.: Thermal model of a TOSS 3.0 sensor board for heat flux calculation. Thermal nodes displayed as circles with their respective index and thermal conductivity resistances connecting them displayed as zigzag lines: a) View in $-z$ -direction on top layer, b) Cut through the model view in $+y$ -direction with nodes for thermometers A and B and the photodiode P .

In figure 5.5a thermal nodes and the conductive paths between them are displayed for one layer in the $x - y$ plane. In z -direction, the nodes of elements above one another are connected as can be seen in figure 5.5b. Nodes of the upper layer are numbered 1 to 9 and nodes of the lower layer are numbered 10 to 18. Additional components, such as thermometers, integrated circuits or photo diodes, are similarly modeled with an individual node. Table 5.2 relates the indices to the respective thermal nodes. For simulation, the two thermometers THM 1 and THM 2 were modeled as coated with silver and black, respectively.

5.3. Printed Circuit Board

The sensor is built upon a PCB onto which all components are soldered. The PCB's are manufactured by OSH Park LLC (USA) and feature a two layer solder

Tab. 5.3.: FR4 glass epoxy PCB substrate properties from [49] and [50].

Property	Symbol	Value and Unit
Density	ρ	$2.0 \times 10^3 \text{ kg/m}^3$
Specific Heat Capacity	c	$1.2 \times 10^3 \text{ J/kg} \cdot \text{K}$
Thermal conductivity (through)	k_{\perp}	$0.343 \text{ W/m} \cdot \text{K}$
Thermal conductivity (along)	k_{\parallel}	$1.059 \text{ W/m} \cdot \text{K}$

mask over bare copper board [51]. It has FR4 as substrate of 1.6 mm (63 mil) thickness and copper weight of 1 oz = $2.835 \times 10^{-2} \text{ kg}$. FR4 is an epoxy/glass laminate and thermal properties are given in table 5.3. A distinction between thermal conductivity through and along the surface of FR4 is important because the material is anisotropic [50]. Additionally, the copper weight describes the mass of copper cladding per square foot. Assuming the density of copper to be $\rho_{Cu} = 8960 \text{ kg/m}^3$ ([34]), the thickness of the cladding can be calculated with equation 5.3.

$$d_{Cu} = \frac{V_{Cu}}{A_{PCB}} = \frac{m_{Cu}}{\rho_{Cu} A_{PCB}} = 34.1 \text{ } \mu\text{m} \quad (5.3)$$

The PCB's analyzed by [50] had the same structure, thus their data in table 5.3 can be used to model heat fluxes.

For the DS18B20U thermometers used in all TOSS boards, reliable thermal parameters are hard to find. Table 5.4 gives the parameters used for the thermometers in the model which are estimations based on values for Silicon, FR4 and Copper [34, 31]. Internal heat dissipation inside the DS18B20U can occur due to electrical resistance and was included into model.

Tab. 5.4.: Thermal properties of DS18B20U temperature sensors used in the model.

Property	Symbol	Value and Unit
Specific heat capacity	c	$1000 \text{ J/kg} \cdot \text{K}$
Density	ρ	1500 kg/m^3
Volume	V	$2 \times 10^{-8} \text{ m}^3$
Radiant area	A_r	$9 \times 10^{-6} \text{ m}^2$
Internal heat dissipation	ω	1 mW

The sensors are built with two kinds of soldering techniques, SMT and THT. They vary in how the components are attached to the PCB and influence the thermal exchange. According to their names, through-hole components have pins, which are inserted into holes through the PCB and are soldered in place. In contrast, surface-mounted devices are soldered directly to the surface of the

PCB and do not require holes through the PCB. As the thermal conductivity through FR4 (see table 5.3) is about 150 times smaller than the thermal conductivity of typical solder (SnPb: $k = 50 \text{ W/m} \cdot \text{K}$) [34], through-holes greatly increase the heat flux through the PCB. According to the Wiedemann-Franz law [52], there is a relationship between thermal and electric conductivity for metals, which allows the assumption that good electric contacts are also good thermal contacts. This has to be taken into consideration for the development of the thermal model. Surface mounting devices are assumed to be in good thermal contact only with the node they are soldered on, while through-hole devices are in contact with all the nodes around the through-hole. These connections are modeled with an increased thermal conductivity between the two respective nodes. In general, PCB is a good thermal insulator and thus SMT components should be used when thermal decoupling is desired.

A summary of used model parameters for the TOSS v3.0 is given in section C.3.

6. Numerical Methods

Initially, the temperature $T(x, t)$ is not known. Solving the partial differential equation 5.1 analytically for each node and various boundary conditions is beyond the scope of this thesis, due to non linearities and dependencies on other variables. It might even be impossible. The system of equations is, therefore, solved numerically. As a simulation software Matlab was chosen due to its highly versatile programming environment, good community support and stable, fast and good documented built-in routines. Figure 6.1 describes how the program works.

As the temperature field is not known as a function, the partial derivatives have to be approximated numerically. The result is a numeric scheme, which allows the computation of discrete solutions of the partial differential equation. The applied methods significantly influence the computational stability and the effort necessary to obtain usable results. The temporal discretization scheme is given in equation 6.1

$$\left. \frac{\partial T_k}{\partial t} \right|_i = \frac{T_k^{i+1} - T_k^i}{\Delta t} \quad (6.1)$$

while the spacial discretization scheme is given in equation 6.2.

$$\left. \frac{\partial T_k}{\partial x} \right|_i = \frac{T_{k+1}^{i+1} - T_k^{i+1}}{\Delta x} \quad (6.2)$$

In both cases the index k denotes the node and thus the spacial position of the volume element. The index i denotes the temporal position.

Taking equation 5.2, the spacial and temporal discretization schemes can be applied, yielding equation 6.3. For stability an implicit Euler scheme has been selected for arrangement of the temporal steps. This method takes the temperatures of the next time step to calculate fluxes. It is more stable than a forward Euler method but still solvable with reasonable numerical effort as it relies on solving a system of linear equations with sparse connections.

$$\rho_k c_k V_k \frac{T_k^{i+1} - T_k^i}{\Delta t} = - \sum_n A_{k,n} k_{k,n} \frac{T_n^{i+1} - T_k^{i+1}}{\Delta x_{n,k}} - \sum \Phi_{k,other} \quad (6.3)$$

Here, the index n denotes all nodes adjacent to the current node i , describing thermal conduction. The second term on the right side summarizes all fluxes, which are not thermal conduction. All equations for all nodes form a system of equations, which is described in equation 6.4.

$$(\mathbf{I} - \mathbf{C} - \mathbf{D}_l) \mathbf{T}^{i+1} = \mathbf{T}^i + \mathbf{D}_r \quad (6.4)$$

where I is the identity matrix, C is the connection matrix, effectively describing conductive fluxes, and D_l and D_r are a matrix and a vector describing radiation

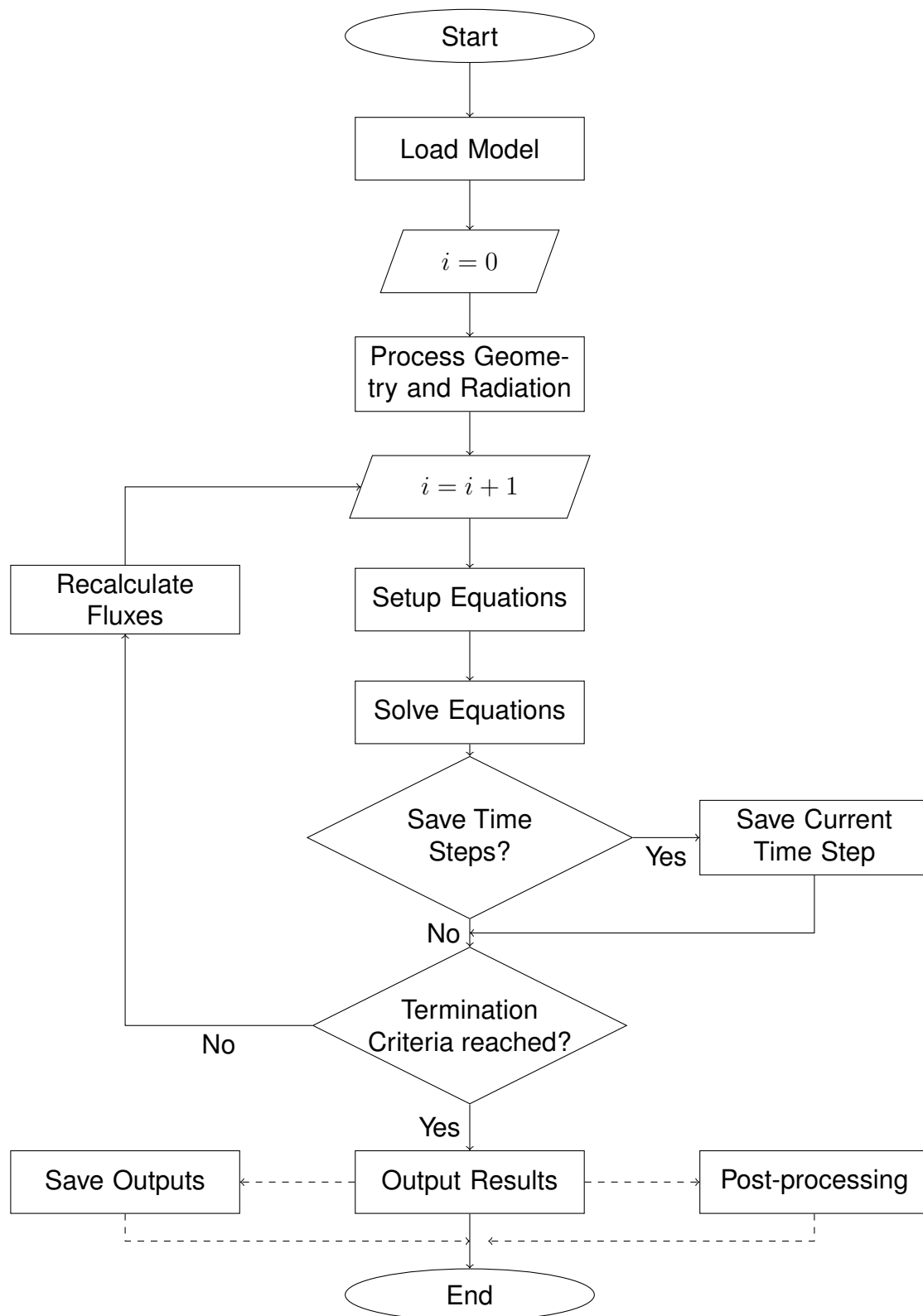


Fig. 6.1.: Flow chart describing the program routine. Post-processing and saving outputs is optional.

and other fluxes in equation 6.3. The entries in the C matrix can be calculated with equation 6.5.

$$C_{n,k} = \frac{A_{n,k} k_{n,k} \Delta t}{\rho_n c_n V_n \Delta x_{n,k}} \left[\frac{\text{m}^2 \text{ W/m} \cdot \text{K s}}{\text{kg/m}^3 \text{ J/kg} \cdot \text{K m}^3 \text{ m}} = 1 \right] \quad (6.5)$$

Furthermore, thermal radiation poses a problem as it is not linearly dependent on the temperatures involved. In order to apply the implicit Euler method, linearization with a Taylor series expansion has been done. Given a function $X_k^{(i)}$, where k denotes the spacial position and (i) denotes the temporal step, equation 6.6 shows how to calculate the [53]

$$\Phi_k^{(i+1)} = \sum_{n=0}^m \frac{\partial^n \Phi_k^{(i)}}{\partial T^n} \frac{\Delta T_k}{n!} + \mathcal{O}((\Delta T)^{m+1}) \quad (6.6)$$

where $T_k^{(i+1)} - T_k^{(i)} = \Delta T_k$. For thermal radiation, equation 3.20 must be linearized, which yields equation 6.7. The heat flux is only linearly dependent on the temperature of the next time step $i + 1$ and can thus be calculated with the described numeric scheme.

$$\begin{aligned} \Phi_k^{(i+1)} &= \sigma \varepsilon_k A_{k,rad} (T_k^{(i+1)4} + 4T_k^{(i)3} (T_k^{(i+1)} - T_k^{(i)}) - T_{bg}^4) + \mathcal{O}((T_k^{(i+1)} - T_k^{(i)})^2) \\ &= \sigma \varepsilon_k A_{k,rad} (4T_k^{(i)3} T_k^{(i+1)} - 3T_k^{(i)4} - T_{bg}^4) + \mathcal{O}(\Delta T_k^2) \end{aligned} \quad (6.7)$$

In addition with the other fluxes and internal heat sources, D_l and D_r can be determined. They are given in equations 6.8 and 6.9, respectively. The matrix D_l is a diagonal matrix populated with the radiation linearization part of the next time step.

$$\mathbf{D}_l = 4\sigma\varepsilon \frac{\mathbf{A}_{rad}\Delta t}{\rho\mathbf{cV}} \mathbf{T}^3 \left[\frac{\text{W/m}^2 \cdot \text{K}^4 \text{ m}^2 \text{ s K}^3}{\text{kg/m}^3 \text{ J/kg} \cdot \text{K m}^3} = 1 \right] \quad (6.8)$$

The vector D_r is the sum of the radiation linearization part of the current time step and all other fluxes.

$$\mathbf{D}_r = \frac{\Delta t}{\rho\mathbf{cV}} (\Phi_{other} - 3F\sigma\varepsilon\mathbf{A}_{rad}(\mathbf{T}^4 - \mathbf{T}_{CMB}^4)) \left[\frac{\text{s (W + W/m}^2 \cdot \text{K}^4 \text{ m}^2 \text{ K}^4)}{\text{kg/m}^3 \text{ J/kg} \cdot \text{K m}^3} = \text{K} \right] \quad (6.9)$$

The matrices D_l and D_r have to be adapted and recalculated in every iteration. By performing a dimensionality analysis, the structure of the matrices can be confirmed. Both C and D_l have no dimensionality, D_r has the unit K . The units are in accordance with equation 6.4.

7. Verification and Experiments

This section shows that the numerical routines implemented work properly, for both the TOSS v2.2 and the TOSS v3.0 model. For the TOSS v2.2 board, results of experiments scrutinizing its model's physical behavior are presented and taken under investigation. The TOSS v2.2 board has been selected, because it has more sensors and thus can yield more information on the model parameters.

7.1. Simulation Code Verification

In this section, the numerical routines are evaluated using designed, generic test cases individually focusing on specific and critical solver aspects. The test cases are intended to highlight proper and stable numerics. The results are shown in various figures and are also evaluated mathematically.

7.1.1. No Gradients Case

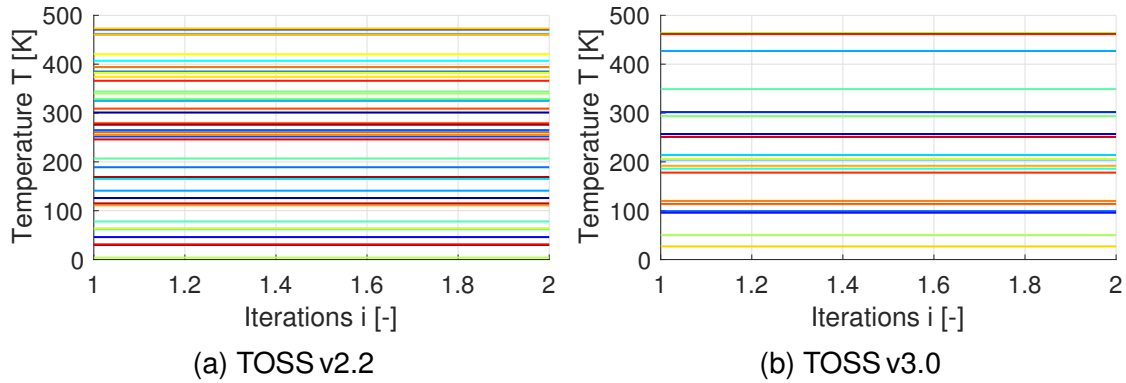


Fig. 7.1.: Verification case - No gradients: All conductivities are set to zeros.

Firstly, the solver is checked for numerical leaks, which may appear whenever the connections between volume elements and their respective nodes are not implemented properly. In this test case, radiative heat exchange calculation and thermal conductivity are disabled, theoretically prohibiting thermal exchange between the nodes by not allowing thermal gradients. The temperatures are initialized randomly to ensure differences. Equation 7.1 gives a metric with which the test can be evaluated.

$$\sum_i T_{i,2} - T_{i,1} \stackrel{!}{=} 0 \quad (7.1)$$

where the index i denoted the nodes.

Figure 7.1 depicts the results of the simulations. Temperatures do not change for both models as all gradients are zeros. Equation 7.1 is satisfied and the test is passed. This test's results also shows that the termination criteria works. Iteration counts are always integers and the solver terminates after just one iteration, because there are no changes in temperature.

7.1.2. Heat Diffusion Case

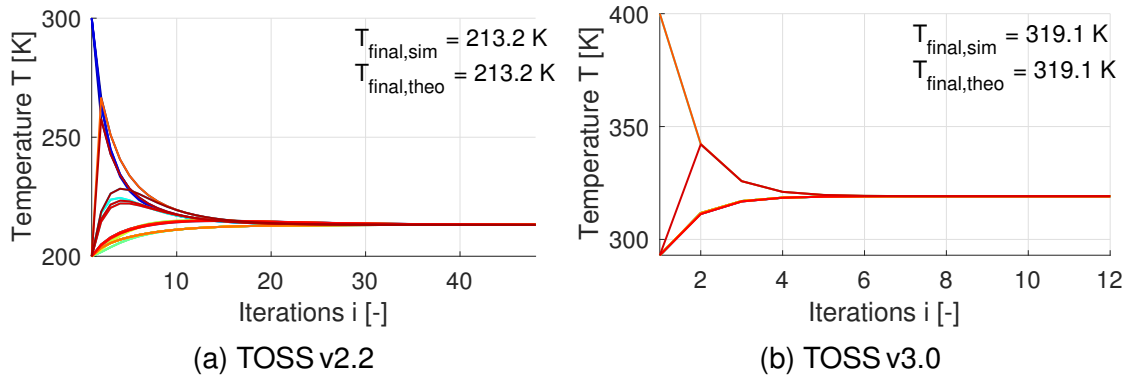


Fig. 7.2.: Verification case - Heat diffusion: All radiation is neglected and the temperatures are initialized with spikes.

Secondly, the model's thermal conduction is investigated. Unequally distributed heat, which is set up by initializing some node's temperatures higher than others, is supposed to spread equally to all nodes. The resulting equilibrium temperature can be calculated using equation 7.2

$$T_{equal} = \frac{\sum_i \rho_i c_i V_i T_{i,1}}{\sum_i \rho_i c_i V_i} \quad (7.2)$$

where $T_{i,1}$ are the initial temperatures in K .

Figure 7.2 depicts the results of the simulation. The temperature curves show the convergence towards the equilibrium temperature. The metric in equation 7.2 also returns the simulated temperature. Additionally, the TOSS v3.0 model converges significantly faster than the TOSS v2.2 model, as it consists of fewer nodes. The test is passed.

7.1.3. IR Radiation Case

Thirdly, infrared emission calculation is scrutinized. When radiating towards an environment with constant uniform temperature, the Stefan-Boltzmann law (see equation 3.17) predicts convergence of the radiating system's temperature to the stable environment temperature, $T_{final} \stackrel{!}{=} T_{\infty}$, where T_{∞} is the environment's temperature. In this verification case, the environment temperature has

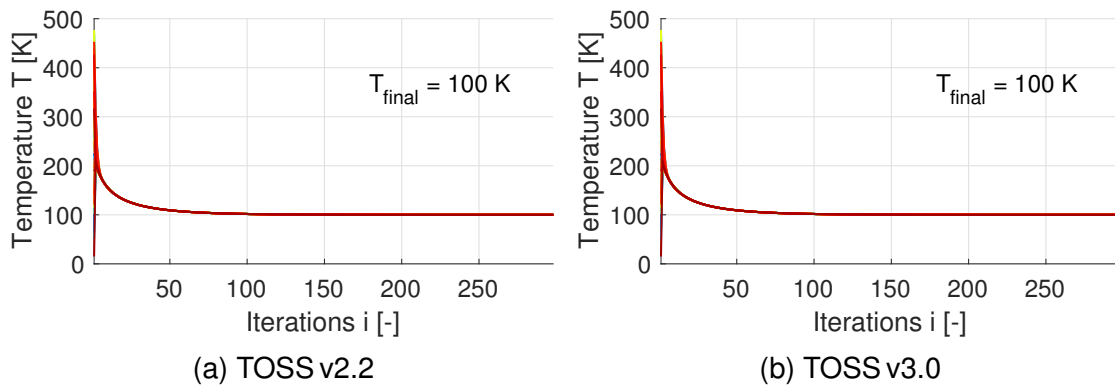


Fig. 7.3.: Verification case - IR radiation: IR emission is enabled and temperatures are initialized randomly.

been set to $T_{bg} = 100$ K to allow for faster convergence and better visualization. This change does not impact the validity of the test case, as the environment temperature does not change the nature of IR emission. The temperatures are initialized randomly, as the initial temperature must not have an impact on the final temperature.

Figure 7.3 depicts the results of the simulation. The final temperatures converge properly to the environment's temperature. Also, the curves confirm proper representation of the Stefan-Boltzmann law. The speed of decline is proportional to the fourth power of the difference between the radiating node's temperature and the environment's temperature. The test is passed.

7.1.4. Radiation Equilibrium Case

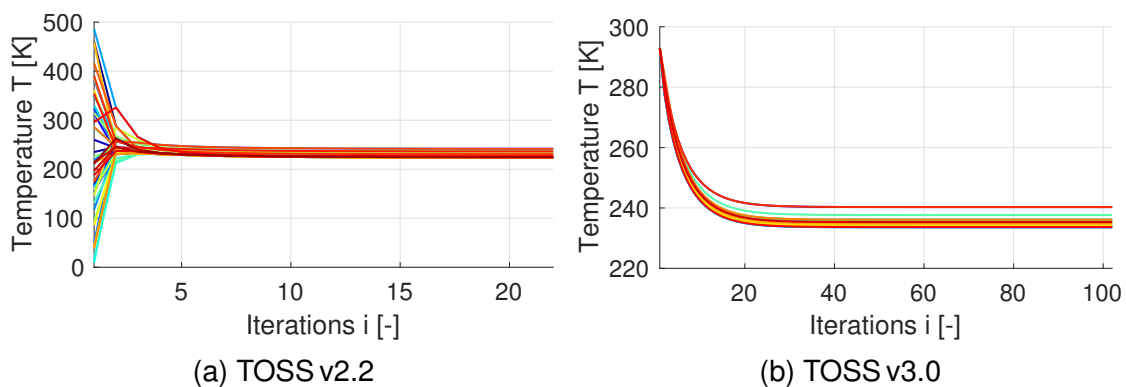


Fig. 7.4.: Verification case - Radiation equilibrium: Solar irradiation and IR emission yield stable equilibrium temperatures.

Fourthly, incident solar radiation and IR emission is tested. Given these two heat exchange mechanisms, the temperatures must converge to stable values according to their surface properties. Emissivity and absorptivity are the main

parameters contributing to the final temperatures, which have to be in accordance with equation 7.3.

$$\sum_i \Phi_{i,in} = \sum_i \Phi_{i,out} \quad (7.3)$$

Conductive fluxes inside the model may also occur, making quantitative prediction hard. Two pairs out of four THM's are each considered to be coated with similar finish, which differ in emissivity and absorptivity. The PCB and the PD's also have differing surface coating properties. Qualitatively, this translates into different final temperatures for each node.

Figure 7.4 depicts the results of the simulation. The differing temperatures are distinguishable and on a reasonable level. Especially for the TOSS v3.0 model in figure 7.4b multiple temperatures are visible. The test is passed.

7.1.5. Temporal Behavior

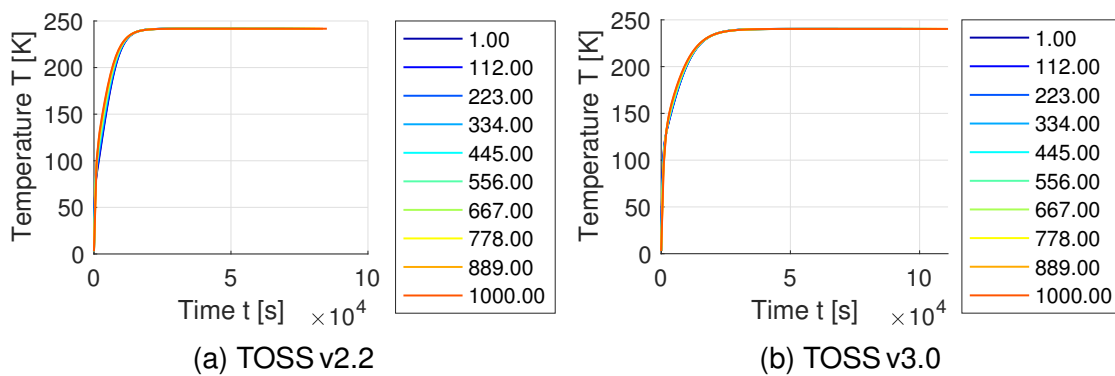


Fig. 7.5.: Verification case - Solver time step: Variation of the solver's time step. The legend shows the time step in seconds.

Lastly, the influence of the iterative time step on the result has been investigated. The influence of the chosen time step on the simulation's physical results should converge towards the real physical process with decreasing time step. Because an implicit iteration scheme has been selected (see equation 6.3), changes are prone to overestimation for bigger time steps.

The results of the analysis for both models are given in figures 7.5a and 7.5b. The final temperature is equal for all time steps, proving independence from the selected time step. The differences in the curves is due to different time discretization and approaching the curves of smaller time steps. Also the error from linearizing radiative heat exchange gets smaller with decreasing time set size. The test is passed. Although, it is worth noting that increasing the time step significantly decreases the iterations necessary to reach the termination criterion. Especially for preliminary testing, increasing the time step can be reasonable ($\Delta t > 60$ s).

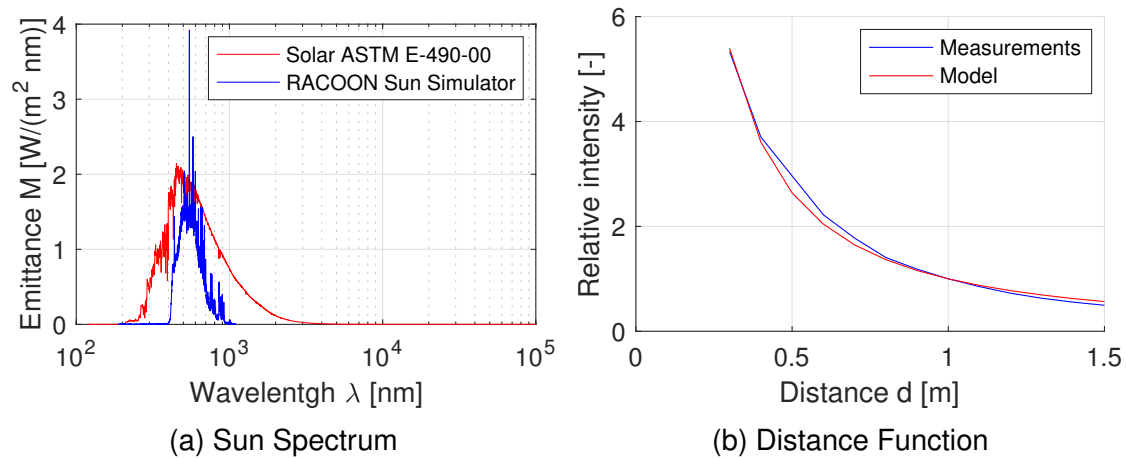


Fig. 7.6.: RACOON-Lab Radiation Environment: a) Sun simulator spectrum at $d = 1$ m and ASTM E-490 standard AM0 Sun spectrum for comparison, b) Radiation intensity relative to reference $d = 1$ m.

7.2. RACOON-Lab Experiments

For physical model verification, experiments have been performed in the Robotic Actuation and On-Orbit Navigation Laboratory (RACOON-Lab) [54] using the TOSS v2.2 sensor board. The laboratory has some unique environmental features, as depicted in figure 7.6. Its walls are covered with low reflective theater cloth and a lamp with known spectrum is available. The lamp's measured spectrum is depicted in figure 7.6a [55]. Besides, the irradiation over distance function in the lab is different from what a space craft experiences. As the Sun simulator is a focused lamp with lenses and mirrors, the photometric law in equation 3.22 can not be applied. The inverse square law must be altered to be able to predict thermo-optical processes in the RACOON-Lab. Changing the exponent to 1.4 yields the desired behavior, see figure 7.6b. The intensity was measured with an INS DX-100 Digital Lux Meter [56]. For simulation, this exponent for the photometric law has been used rather than applying the inverse square law. With these assumptions, an optically and thermally well known environment can be provided by the RACOON-Lab. The TOSS v2.2 was chosen for the experiments, because it had more sensors providing information.

When the experiments were performed, the ambient temperature was $T_{bg} \approx 306$ K = 33 °C. Three of the sensor's thermometers have been coated with plastic foils. Different emissivity and absorptivity yields different steady state temperature measurements. Thermometer 1 has not been coated, thermometer 2 has been coated with a golden plastic foil, thermometer 3 with a black CFRP-imitate and thermometer 4 with a silver plastic foil.

To be able to show behavior over different angles, a high precision test bed for CubeSats was used [57]. The test bed allows for rotations with a very well defined angular velocity. The experiments focus on different aspects of the model and two measurement campaigns were conducted. Parameters of the

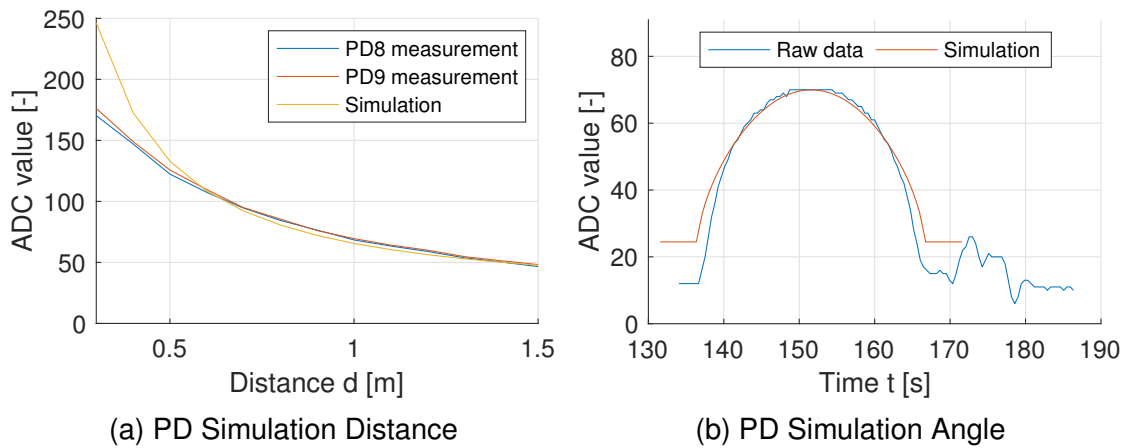


Fig. 7.7.: Measured and simulated photocurrent ADC values from RACOON-Lab experiments: a) Over distance from the Sun simulator for irradiation in normal direction, b) Over time for a system with constant angular rotation from experiment 6.

first measurement campaign are listed in table C.1. The experiment's main purpose was the demonstration of a proper thermal modeling. Experiments 1 to 9 and partially 11 measure how the photo diodes on the TOSS v2.2 board work. Experiments 10 and 12 to 15 focus on thermal steady states, while experiment 11 pays attention to unsteady conditions. Experiments 1 to 3 were not used, because reflections from the test bed might have influenced the measurements. In the following, the test bed was covered with a dark velvet which significantly reduced the reflections. The second measurement campaign focused on the photo diode and the radiation attenuation over distance. Temperature measurements were recorded without prior influence and thus should theoretically show identical ambient temperatures. Although, all thermometers measured slightly different temperatures. In following post-processing routines, these differences were subtracted out as calibration for better comparability.

7.2.1. Photo Diode Experiments

Firstly, the TOSS v2.2 photo diode model has been tested against data from test campaign two's distance experiments and campaign one's experiment 6 which measured photocurrent versus angular displacement (see table C.1). Figure 7.7 depicts both results. Plotting the results in ADC-values allows plotting of raw measurement data and simultaneous verification of the ADC model.

Figure 7.7a shows both the measurements of the experiments and the results of TOSS v2.2 simulations for corresponding distances under RACOON-Lab environment. From the raw measurements (see figure C.3) the mean of the high state was taken as photocurrent. The curves overlay each other nicely and prove proper modeling of the spectral sensitivity.

For verification of the radiant sensitivity, figure 7.7b shows measured photocurrent from photo diode 6 of experiment 6 and the results of a corresponding simulation over time. As a constant angular velocity $\omega = 1 \text{ r/min}$ of the test bed was used, the time linearly translates into incident angle, which is the value of interest. For angles greater than 90° the measurements are noisy and are not considered valid measurements because no radiation should be incident on the photo diode. Within the angle range, both curves overlay each other nicely and prove proper modeling of radiant sensitivity.

7.2.2. Thermal Experiments

Secondly, the TOSS v2.2 thermal model has been tested against data from experiments 10 and 12 to 15. These experiments are designed to show the temporal convergence towards a steady state temperature for both different distances from the radiation source and different incident angles. Although, some model parameters are rather poorly known, for example the thermometer's specific heat capacity or the coating's thermal radiation coefficients. By tweaking these parameters within a reasonable range, a close fit of the model to the experiments was achieved.

Most prominently, the thermal capacity and the density of the PCB and the Thermometer (THM) have been adjusted for a better fit. Combining these two parameter with the volume yields the thermal capacity, which determines the rate at which the temperature changes under irradiation. Under equal circumstances, high thermal capacity systems change temperature slower than systems with low thermal capacity. Since both parameters are known rather poorly, they can be adjusted to fit the measurements within reasonable ranges. In table 5.4 these adjusted values are given.

Besides, the surface properties of the PCB and the THM have been modified to yield better results. Spectral absorptivity and emissivity can vary significantly even for seemingly equal materials, due to invisible differences in material composition, differences in wave lengths outside of the visible spectrum and others. The surface coating parameters influence the radiative thermal fluxes and thus mainly the final temperatures. As the temperature curves for the non rotating experiments converge towards individual temperature, the radiative surface properties of all THM's have been adjusted within a reasonable range. The aim was a good fit between measured and simulated temperatures.

Figures 7.8a and 7.8b show the temperature curves of thermometers 3 and 4 for all relevant experiments, respectively. As mentioned, THM 3 was coated with a CFRP imitate plastic foil while THM 4 was coated with a silver plastic foil. The plots for the other thermometers are given in figures C.1 and C.2. The measured data was calibrated and the simulated temperature curves were obtained using the adjusted model. Apart from experiment 14, the simulations and the experiments correlate to a high degree. Experiment 14 shows consistent

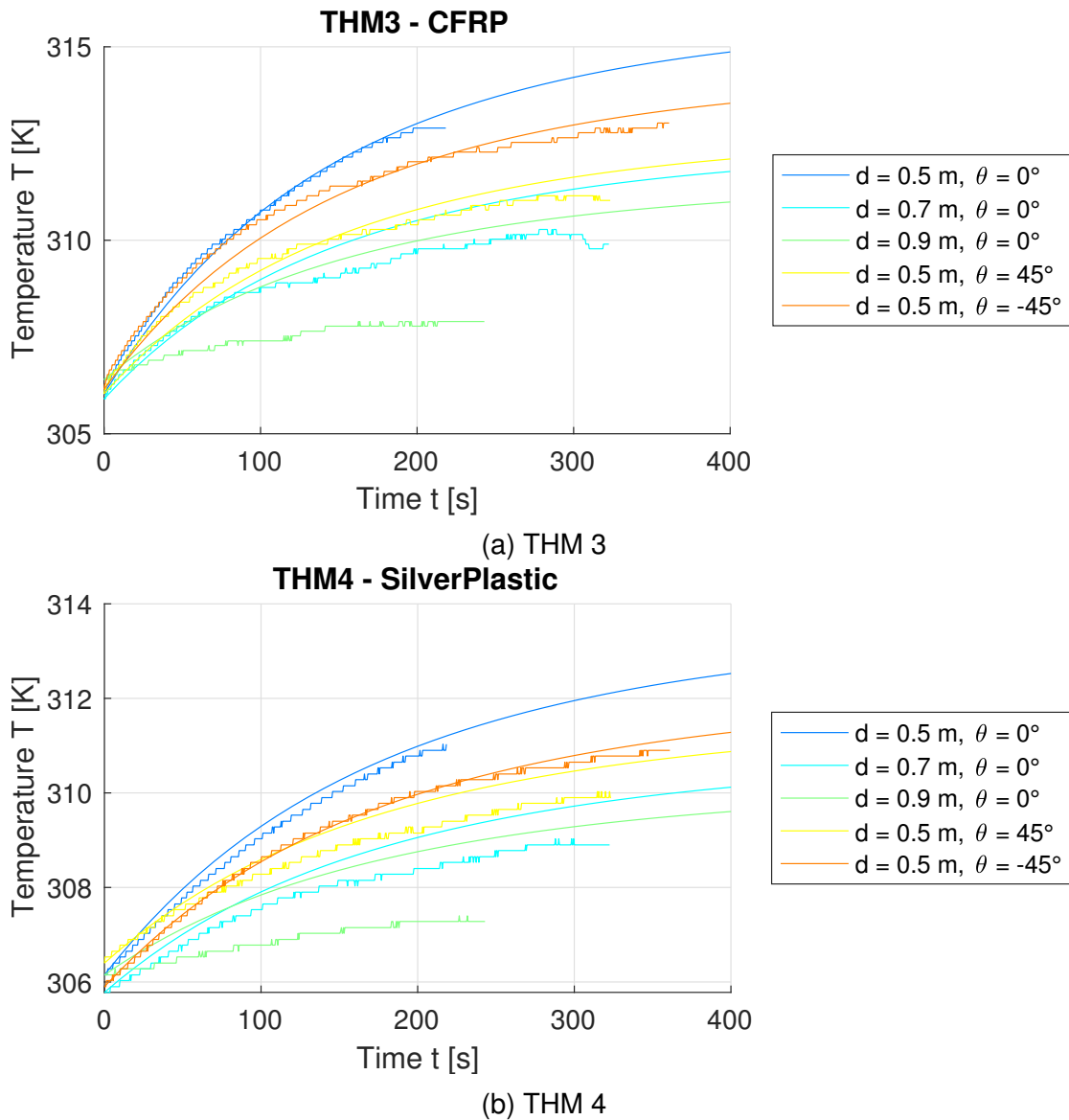


Fig. 7.8.: Temperatures of thermometer simulated using the adapted TOSS v2.2 model and measured in the RACOON-Lab experiments: a) THM 3 coated with a CFRP imitate plastic foil, b) THM 4 coated with a silver plastic foil.

lower temperature measurements than simulated temperatures. Before the experiment has been conducted, the distance between the Sun simulator and the sensor has been changed, which could have resulted in a lower distance measurement and subsequently in higher simulation values as the distance function is steadily decreasing. Another interesting observation is, that there are significant differences in the magnitude of the temperature change, which clarifies the influence of the surface coating.

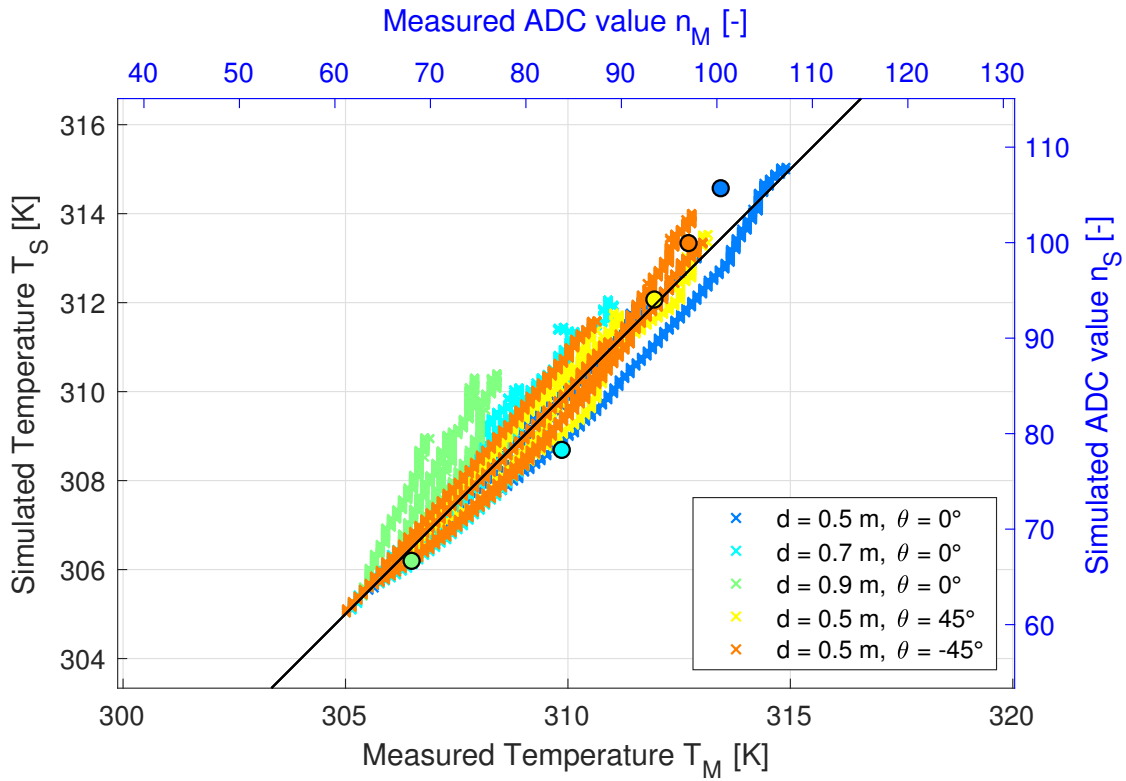


Fig. 7.9.: Cross plot of experiments in the RACOON-Lab and corresponding simulation using the TOSS v2.2 model. Different colors indicate experiments. Crosses show temperatures, circles photocurrent ADC readings. The black line is the identity line, which is also the optimum result.

7.2.3. RACOON-Lab Experiments Summary

As a summary, the cross plot of the simulated temperatures versus the measured temperatures is given in figure 7.9. For the mentioned experiments, all four thermometer measurements are plotted in the same color. The closer the data points are to the identity line, the better the model. A linear fit (see section B.3) of simulated temperatures against measured temperatures yields a slope of $\hat{b}_T = 0.97$ with a root mean square error of 0.62 and a coefficient of determination of $R^2 = 0.95$. These two values show a good correlation between the thermal model and reality. Additionally, figure 7.9 depicts the simulated photocurrents over the measured photocurrents. The identity line is similar for both axes. An offset of $n_{offset} = 25$ to the measured photocurrents was used, as the photo diode's reading was this value under no irradiation. The slope of a linear fit to the ADC values is $\hat{b}_{ADC} = 0.8$ with a root mean square error of 2.85 and a coefficient of determination of $R^2 = 0.93$. Comparing the values to the PD measurements in figure 7.7, the model can be seen as sufficient. Also, the experiments investigate change in temperature both over distance and over incident angle. Therefore, results from the simulation with the adjusted model show proper description of both phenomena.

8. Simulation and Analysis

With the correlated material parameters from chapter 7, simulations with the TOSS v3.0 sensor board model have been performed. In the following, the simulation is regarded as a function f , as given in equation 8.1. It relates the model, incident angles and albedo share to the temperature measurements and the photocurrent.

$$[T_1, T_2, I_{PD}] = f(model, \beta_S, \beta_E, \xi) \quad (8.1)$$

where T_1 is the measurement of thermometer THM 1, T_2 is the measurement of thermometer THM 2 and I_{PD} is the current produced by the photo diode. The combinations of β_S , β_E and ξ in a simulation is called the parameter space in the following and is abbreviated with $X = [\beta_E, \beta_S, \xi]$. The process of finding a set of angles from measurements will be referred to as the pseudo-inverse function to the simulation. Equation 8.2 gives the mathematical description.

$$[\beta_E, \beta_S] = f^{-1}(T_1, T_2, I_{PD}) \quad (8.2)$$

Figure 8.1 shows a generic temperature field for thermometer 1 for the entire possible parameter space and gives an overview over specific regions in the parameter space, where the sensor shows different behavior due to incident radiation. This field is part of the results from a generic TOSS v3.0 simulation. In figure 8.1, $\beta_{S,crit}$ and $\beta_{E,crit}$ describe the maximum angles for which the respective celestial body is visible. As the orbit is not a fixed design parameter for the TOSS, these lines can move for different orbits depending on the view factors and possibly influence the sensor's behavior. For a LEO with $h_{LEO} = 400$ km the critical Earth angle is $\beta_{E,crit} = 160^\circ$ (see equation 3.26). The critical Sun angle is $\beta_{S,crit} = 90^\circ$ (see equation 3.25). The regions, which have been labeled in figure 8.1, have different properties:

- **Region 1** ($\beta_S < \beta_{S,crit}$ and $\beta_E < \beta_{E,crit}$): This is the main region in which the sensor should be operated. Here, solar radiation, infrared radiation from Earth and albedo are potentially visible and the determination of both the Sun and the Earth angle is possible. Region 1 is characterized by gradients in all directions.
- **Region 2** ($\beta_S < \beta_{S,crit}$ and $\beta_E \geq \beta_{E,crit}$): In this region, only solar radiation is incident on the sensor. As the Earth angle is greater than the critical Earth angle, Earth is not in the sensor's FOV and no measurement regarding its direction can be made. Only the determination of the Sun angle is possible. Region 2 has no gradient in Earth angle direction and the uncertainty regarding the Earth angle is the width of this region in the parameter space.
- **Region 3** ($\beta_S \geq \beta_{S,crit}$ and $\beta_E < \beta_{E,crit}$): Similarly to region 2, in region 3 no solar radiation is incident on the sensor as the Sun angle is greater

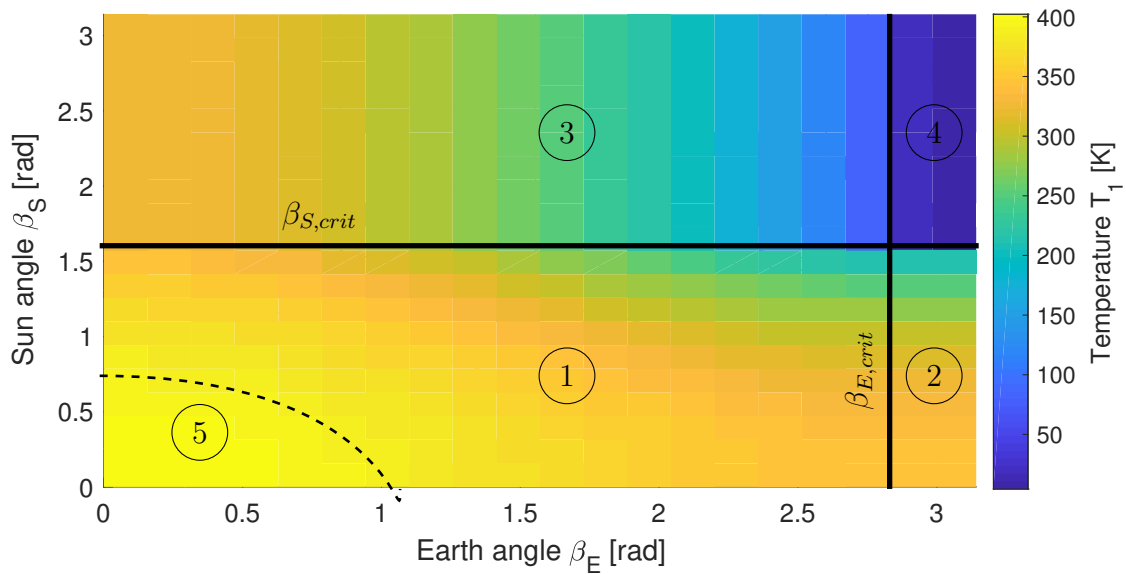


Fig. 8.1.: Generic temperature field of THM 1 over the parameter space. Measurement regions are indicated.

than the critical Sun angle. Thus, only a measurement of Earth's direction is possible because region 3 has no gradient in Sun angle direction. The uncertainty regarding the Sun angle is the width of this region in the parameter space.

- Region 4 ($\beta_S \geq \beta_{S,crit}$ and $\beta_E \geq \beta_{E,crit}$): When both angles are above their respective critical angle, no radiation is incident on the sensor and no attitude determination is possible. Region 4 has a gradient neither in Earth angle direction nor in Sun angle direction and is characterized by a constant final temperature, defined by internal heat sources and emission towards the CMB. The uncertainty regarding both Sun and Earth angle is the width of the parameter space in the respective direction.
- Region 5: This region is special and has an undefined boundary. Values within this region might not be possible from a geometric point of view. For example, when both angles are zeros, the satellite would be in Earth's shadow. This fact is of no special interest to this thesis but determining the boundaries could become important, for example when considering maximum temperatures.

One should be aware, that figure 8.1 displays a generic temperature field in two dimensions. The temperature field along with the boundaries also extends in ξ direction. For analyses, points within region 1 were selected as the accuracy for both Sun and Earth angle should be assessed by sensitivity analysis.

8.1. Sensitivity Analysis

Sensitivity in the context of numerical evaluation of mathematical models describes the relation between changes in the input parameters to changes in the output values. Analysis of a systems stability, can yield valuable insights on the relations between the individual model parameters, the uncertainty and may lead to simplifications. Multiple methods to analyze, calculate and describe sensitivity exist. However, defining an optimum sensitivity appears to be difficult. A sensor which is too sensitive can be prone error due to exterior disturbances. On the contrary, an insensitive sensor may not recognize changes at all.

To find parameters critically influencing the accuracy of the sensor and evaluating the influence, One-factor-at-a-time (OFAT) analysis were conducted. OFAT is one of the most commonly used methods to analyze sensitivity due to its simplicity and practicability. Information on the influence of one parameter is gained by changing one input parameter while holding all other inputs at a constant, nominal value and evaluating the system. Afterwards, the system is returned to its nominal state and another input parameter can be analyzed. The TOSS v3.0 model struct with the values used is given in section C.3.

Although, OFAT does not explore the whole space of solutions, which can lead to interactions between input variables not being detected. The result of an OFAT run can be evaluated with regression and statistics. Determining whether the sensitivity of the output on an input is beneficial is considerably arbitrary. Nevertheless, sensitive parameters should usually be considered to be of higher importance to the model than insensitive parameters. In the following, OFAT analysis of parameters, which appeared to be influential during the model development, are performed and evaluated. The method of evaluation, primarily concerning changes in the model's outputs and the related radiation incident angles are described in the next section.

8.2. Simulation Evaluation Method

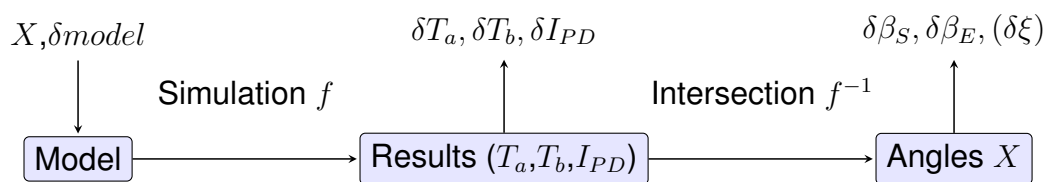


Fig. 8.2.: Flow diagram describing the evaluation method for sensitivity analysis of a TOSS sensor board. Simulation relates the model to temperatures and photocurrent. Finding intersections relates temperatures and photocurrents back to angles.

This section shows how the results from OFAT analysis are evaluated. Figure 8.2 shows the general procedure for an analysis.

1. One model parameter is changed by $\delta model$. All other parameters are unchanged.
2. Simulations with the changed model are performed to cover the parameter space of interest X , which usually is $0 \leq \beta_S \leq \pi$, $0 \leq \beta_E \leq \pi$ and $0 \leq \xi \leq 1$. Here, linearly spaced steps on the interval are taken, yielding temperature and photocurrent matrices.
3. Intersection points of isosurfaces are determined and the difference for different magnitudes of δX is calculated. This yields the uncertainty of the Earth angle $\delta\beta_E$ and the Sun angle $\delta\beta_S$ with respect to the change δX .
4. This process is repeated for different values of $\delta model$ and the changes are evaluated.

Based on simulations with agreed on values for the sensor's material parameters, the reverse calculation can be done by storing a lookup table in the sensor's memory and then searching for a set of angles and albedo share, for which the isosurfaces intersect at one point. Essentially, the reverse calculation is the process of solving equation 8.2.

Initially, isosurfaces were determined. An isosurface Ω to value z for quantity y , defined in equation 8.3, is the amount of point X on which the function f_y is equal to z .

$$\Omega_y(z) = \{X | f_y(X) = z\} \quad (8.3)$$

For example, $\Omega_I(2.5 \text{ mA})$ would be the isosurface for the photocurrent of 2.5 mA with respect to the measurement of the photo diode I . In general, the isosurface Ω describes for which combinations of angles β_S and β_E and albedo share ξ the sensor could measure that value z . As the simulation results are in 3D-grid form, finding the isosurface was done by using the surface intersection algorithm implemented by Tuszynski [58].

The shape of the isosurface alone allows prediction on the sensors behavior with respect to the measured quantity. Firstly, if there is an isosurface to be found in the parameter space, the model states, that the value z is a realistic measurement under the given model constraints. Secondly, the dimensions of the surface are interesting. The isosurface's extend in one dimension shows the uncertainty for that dimension. When it only has no or a small range of values in one dimension, one may assume, that for that the sensor's uncertainty with respect to that value is small. In contrast, an extensive value range of the isosurface in one dimension indicates, that the measurement only provides unreliable information with regard to that dimension.

Figure 8.3 gives an example for this relation. Here, an isosurface for a photocurrent can be seen from a view in ξ – direction. Seeing a surface instead of a line means that the photo diode is influenced by the albedo. If the albedo share is unknown, the Sun angle can be anywhere in the range of approximately 0.9 rad to 1.4 rad, especially at low Earth angles. This range illustrates the inaccuracy of a single photo diode as sensor for the Sun direction. Additionally, the isosurface extends over the entire range of Earth angels which clarifies that a photo

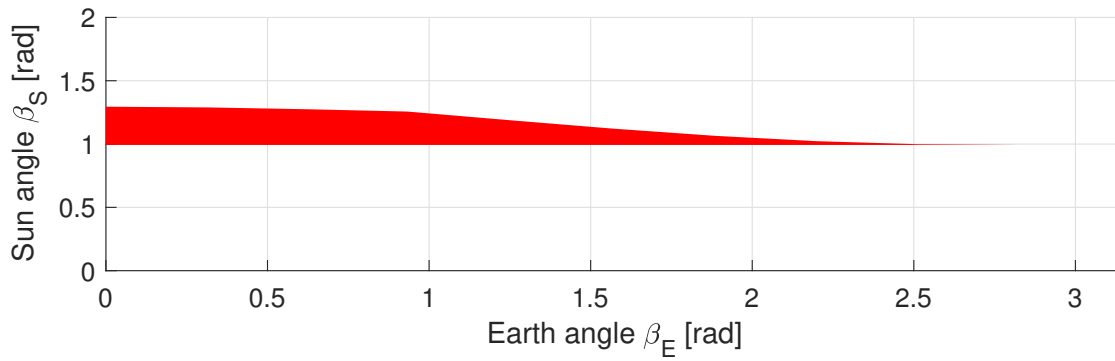


Fig. 8.3.: Example of an isosurface $\Omega_I(2.84 \text{ mA})$ from a TOSS v3.0 model simulation. View in ξ – direction. The extend of the surface describes the sensor’s accuracy under albedo influence.

diode is an inadequate sensor for the nadir direction. Moreover, it can be seen, that the albedo can have a major influence on the sensors accuracy, especially when the Earth angle β_E is small and the view factor F_E is big. This is in accordance with the accuracy problems of Sun sensors due to albedo radiation mentioned in chapter 2.

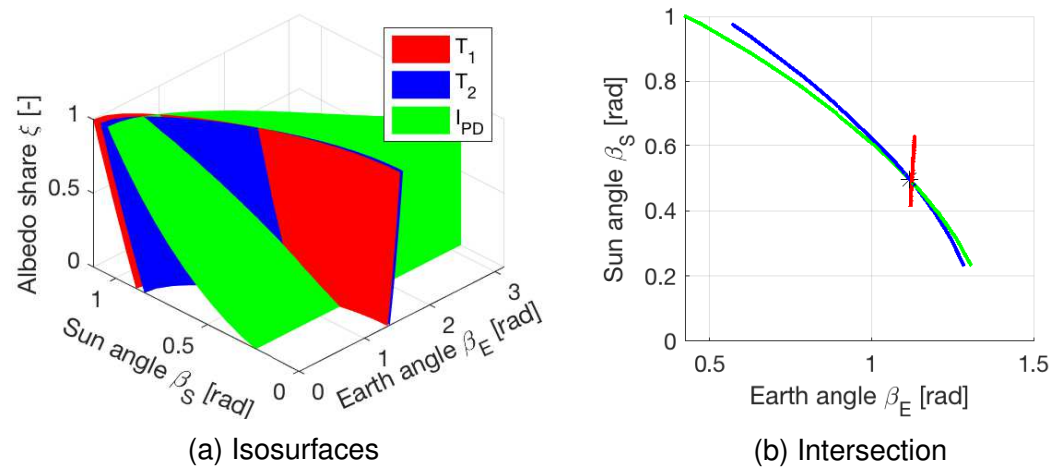


Fig. 8.4.: Example of intersections: a) Three generic isosurfaces intersecting at one point, b) Intersection lines for the three isosurfaces viewed for ξ – direction. The black star is the point where all lines intersect and thus gives the current angles.

The next evaluation step for a TOSS sensor simulation was relating the available isosurfaces of THM 1’s temperature measurement $\Omega_T(T_1)$, THM 2’s temperature measurement $\Omega_T(T_2)$ and the photo diodes current measurement $\Omega_I(I_{PD})$ to the incidence angles for which these measurements could be expected. By geometric reasoning, there are three possibilities of interest for three surfaces to intersect:

- There may be infinitely many intersection. This occurs when the three surfaces are identical or intersect at one line. As the sensor is designed

to have different responses to both the radiation's incident angle and the radiation's spectrum, this case occurs when there is ambiguity in the orientation, as described in figure 8.1. Within these regions all combinations are potentially valid. However, this circumstance is inherent to the sensor and cannot be avoided.

- If the three surfaces are parallel towards each other, there may also be no intersection at all. This would translate in a discrepancy between reality and the model and should not occur.
- Ideally, the three isosurfaces intersect at one distinct point in the parameter space. In this case, the coordinates of this point are the estimations for the Sun angle β_S and the Earth angle β_E . An estimation of the albedo share ξ can also be deduced. Figure 8.4 shows a generic case in which an intersection is present.

Mathematically speaking, the intersection P in the parameter space is the set of parameters $X = [\beta_E, \beta_S, \xi]$ which lies within all isosurfaces for specific values T_1 , T_2 and I_{PD} . Equation 8.4 gives the mathematical description.

$$P = \{X | (X \in \Omega_{T_1}(T_1)) \cap (X \in \Omega_{T_2}(T_2)) \cap (X \in \Omega_I(I_{PD}))\} \quad (8.4)$$

Finding the intersection numerically was done by finding the nodes on the intersections, which had the smallest spacial distance between them and taking their midpoint as intersection. This approximation is necessary because the data is available in gridded form only.

8.3. Sensor Accuracy

With these tools, analysis of the TOSS's accuracy was performed to assess its accuracy. Any quantity x can be described by given the expected value \bar{x} and its uncertainty δx , thus $x = \bar{x} \pm \delta x$ (see section B.4). Finding the intersections, on which determination of the uncertainty is based, relies on accurate temperature and photocurrent measurements. However, the thermometers and the photocurrent measurement circuitry have inherent uncertainties, which have to be taken into account. The photocurrent amplification circuitry is subject to uncertainties standard COTS components have inherent. When in a system together, the gain (see equation 4.6) has an uncertainty which is given in equation 8.5 and which relies on the uncertainties of all individual parts (see section B.4).

$$\delta G = \sqrt{\sum_i \left(\frac{\partial G}{\partial R_i} \right)^2 \delta R_i^2} \quad (8.5)$$

An uncertainty of 0.1% for the resistors used on the board translates into $\delta G = 0.05$. The relative uncertainty, given in equation 8.6, is thus the amount of uncer-

Tab. 8.1.: Statistics of TOSS v3.0 uncertainty analysis for Earth and Sun angle due to inherent instrument uncertainty.

Dimension	Mean μ	Standard Deviation σ
Earth angle β_E	0.5 rad	0.12 rad ²
Sun angle β_S	1.1 rad	0.14 rad ²

tainty for both the gain and the photocurrent compared to their absolute value and can be seen as the accuracy of the current measurement.

$$\frac{\delta G}{G} = \frac{\delta I}{I} = 1 \times 10^{-3} \quad (8.6)$$

There is also an uncertainty in the ADC within the microcontroller used. The datasheet specifies the uncertainty of the ADC to be ± 2 for the least significant bit, which is around 0.1% of its maximum [59]. This error also includes the uncertainty from the internal reference voltage and is added to the result from equation 8.6, yielding $\delta I/I = 2 \times 10^{-3}$.

For the thermometers, the data sheet gives an accuracy of $\delta T_{THM} = 0.5$ K [24]. This means, that even without external influences the sensor has an inherent uncertainty as the isosurfaces necessary for finding the intersection point in the simulation data may vary.

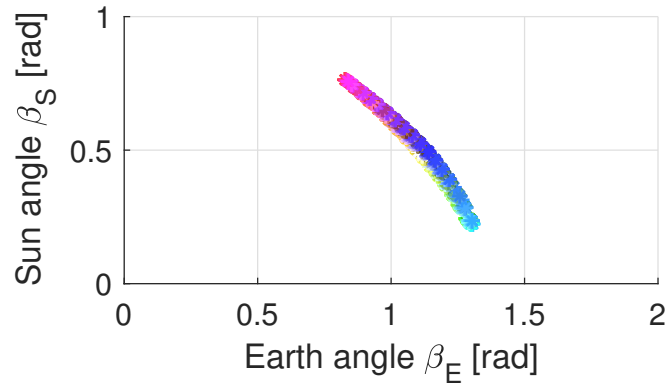


Fig. 8.5.: Isosurface intersection P of the uncertainty analysis for the TOSS v3.0 sensor model. The color encodes variation of parameters X in RGB.

To address TOSS v3.0's uncertainty when using its model, a variation of temperatures and photocurrent was performed. For a point in the parameter space ($\beta_E = 0.5$ rad, $\beta_S = 1.1$ rad, $\xi = 0.5$), the temperatures of both THMs and the photocurrent from the photo diode were taken as reference values. Then, all three quantities were varied around that point in the range of the parameter's respective uncertainty. Performing this variation yields information on the sensor's response to its inherent uncertainty.

Figure 8.5 depicts the intersections resulting from temperature and photocurrent variation. The image is RGB color encoded. Variations in the red share encode

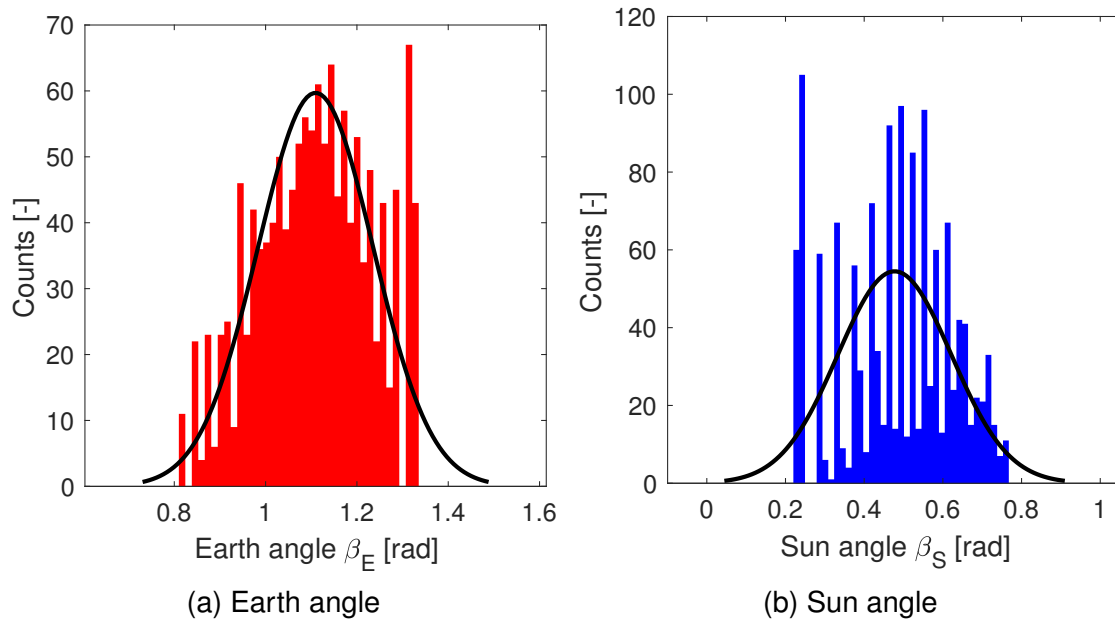


Fig. 8.6.: Histograms of the sensor's vector uncertainty due to inherent instrument uncertainty in: a) Earth angle, b) Sun angle. In both figures the black line is the best fit Gaussian probability distribution curve.

variation for temperature T_1 , green for temperature T_2 and blue for photocurrent I_{PD} . For analysis, figure 8.6 shows histograms of the intersection point coordinates in Earth and Sun angle direction for all variations. A Gaussian normal distribution curve $\mathcal{N}(\mu, \sigma)$ (see section B.1) has been fitted to both datasets and their statistical parameters are given in table 8.1. The distribution's mean values are equal to the values used as reference. For technical systems, the 68%-error is a common characteristic by which uncertainties are quantified. The background is, that for a data set with underlying normal distribution, approximately 68% of all data is within the interval $[\mu - \sigma, \mu + \sigma]$. Based on the current model and the statistical parameters, the TOSS v3.0 sensor has a 68% Earth vector error of $\delta\beta_{E,\sigma} \approx 0.12 \text{ rad} = 7.0^\circ$ and a 68% Sun vector error of $\delta\beta_{S,\sigma} \approx 0.14 \text{ rad} = 8.2^\circ$ due to its inherent component accuracy mainly in the thermometers.

8.4. Influence Analysis

The sensor's model itself has uncertainties, inducing uncertainties into the sensor's accuracy as finding the intersections from temperatures and photocurrent relies on an accurate model. Therefore, model parameters that showed to be influential during development are analyzed in the following. The methods used are similar to the previous analysis of the overall sensor accuracy.

8.4.1. Albedo Radiation

Earth's albedo radiation M_A is the a major source of inaccuracies for Sun sensors (see section 3.3.7). To assess the magnitude of the error inflicted on the sensor by Earth's albedo, an uncertainty analysis of Earth's albedo influence has been performed. An uncertainty in the reflectance defining Earth's albedo spectrum of $\pm 30\%$ ($\delta \varrho_A = \pm 0.3$) for all wavelength was assumed. The following figures 8.7a and 8.7b give the distributions of the angles resulting from the albedo variation.

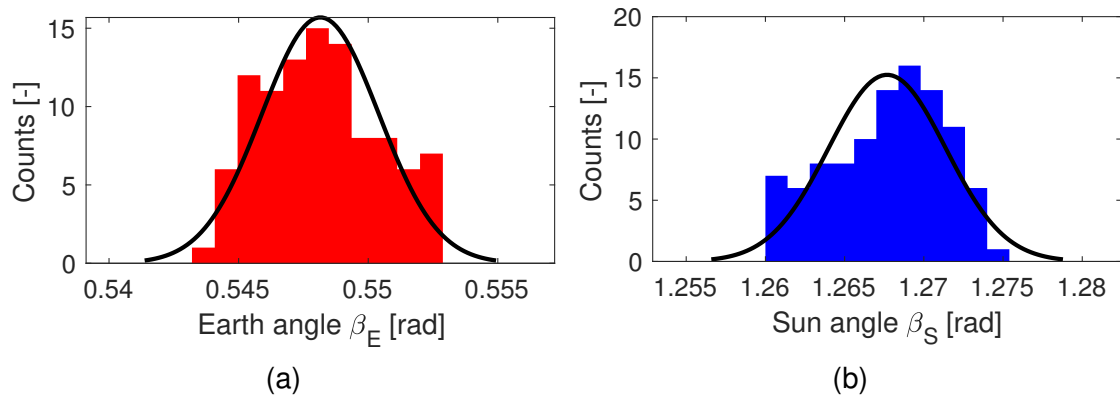


Fig. 8.7.: Histograms of the sensor's vector uncertainty due to Earth's albedo M_A in: a) Earth angle β_E , b) Sun angle β_S . In both figures the black line is the best fit Gaussian probability distribution curve.

Tab. 8.2.: Statistics of albedo influence analysis for Earth and Sun angle.

Dimension	Mean μ	Standard Deviation σ
Earth angle β_E	0.49 rad	0.01 rad ²
Sun angle β_S	1.12 rad	0.01 rad ²

Table 8.2 gives the statistical parameters of the angle distributions for the variation of the albedo. The 68% Earth vector error is $\delta \beta_{E,\sigma} \approx 0.01 \text{ rad} = 0.4^\circ$ and the 68% Sun vector error is $\delta \beta_{S,\sigma} \approx 0.01 \text{ rad} = 0.4^\circ$.

8.4.2. Earth IR Emission

Similarly to the albedo of Earth, its infrared emission M_E varies significantly over both time and position which has already been discussed in section 3.3.8. To assess the IR emission's influence and the resulting uncertainty of the TOSS, a variation of Earth's IR emissivity has been conducted. Reference was the MODTRAN mean spectrum from figure 3.8. An uncertainty of $\pm 10\% \delta M_E$ in Earth's IR emission was assumed. Figures 8.8a and 8.8b give an overview over the intersection distribution for the albedo variation.

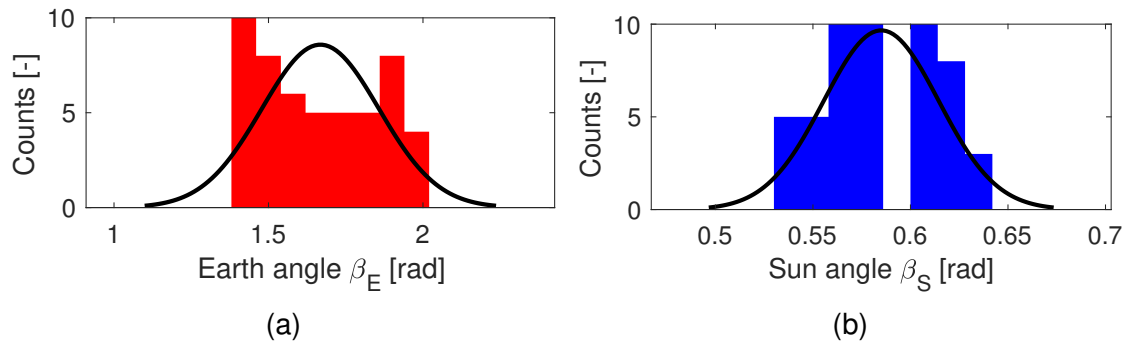


Fig. 8.8.: Histograms of the sensor's vector uncertainty due to variations in Earth's IR emissivity in a) Earth angle β_E , b) Sun angle β_S . In both figures the black line is the best fit Gaussian probability distribution curve.

Tab. 8.3.: Statistics of Earth's IR emission influence analysis for Earth and Sun angle.

Dimension	Mean μ	Standard Deviation σ
Earth angle β_E	1.04 rad	0.01 rad ²
Sun angle β_S	0.59 rad	0.03 rad ²

Table 8.3 gives the statistical parameters of the angle distributions for the variation of Earth's IR emission. The 68% Earth vector error is $\delta\beta_{E,\sigma} \approx 0.01 \text{ rad} = 0.7^\circ$ and the 68% Sun vector error is $\delta\beta_{S,\sigma} \approx 0.03 \text{ rad} = 1.7^\circ$.

8.4.3. Solar Radiation

Besides albedo and IR emission, there are also variation in the solar irradiance M_S . Albeit the solar spectrum can be assumed constant, the distance between the Earth and the Sun changes over time, as Earth's orbit has a nonzero eccentricity [60]. This changes the intensity of the solar radiation. To determine the distance's influence, it was varied in the range encompassing perihelion and aphelion of Earth's orbit, which is $d_{S,E} \in [0.983, 1.017] \text{ au}$.

Tab. 8.4.: Statistics of Solar irradiation influence analysis for Earth and Sun angle.

Dimension	Mean μ	Standard Deviation σ
Earth angle β_E	0.88 rad	0.01 rad ²
Sun angle β_S	0.97 rad	0.01 rad ²

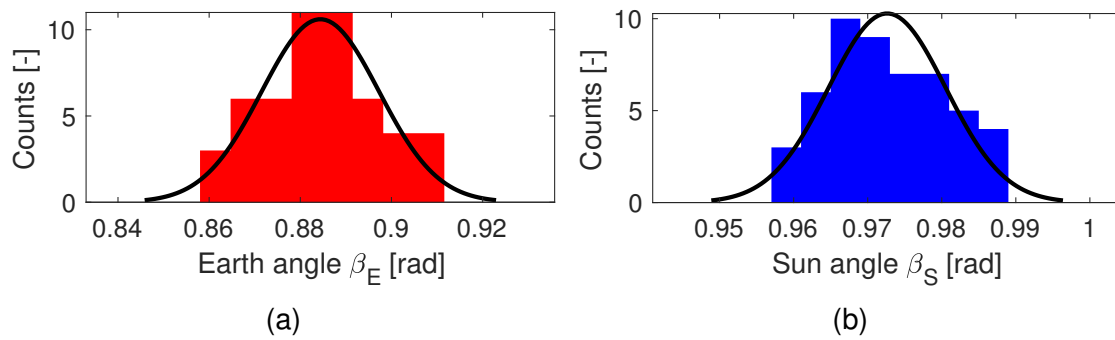


Fig. 8.9.: Histograms of the sensor's vector uncertainty due to variations in Solar irradiation M_S in a) Earth angle β_E , b) Sun angle β_S . In both figures the black line is the best fit Gaussian probability distribution curve.

Table 8.4 gives the statistical parameters of the angle distributions for the variation of the solar irradiance. The 68% Earth vector error is $\delta\beta_{E,\sigma} \approx 0.01 \text{ rad} = 0.7^\circ$ and the 68% Sun vector error is $\delta\beta_{S,\sigma} \approx 0.01 \text{ rad} = 0.5^\circ$.

8.4.4. Thermometer Surface Coating

Still, not only the radiation's intensity but also the surface coating is important for radiant heat exchange. Reliable data on spectral absorptivity (see section 3.3.5) is very hard to find and mostly an educated guess. The influence of different surface coatings, which is an essential feature of the analyzed sensor, can clearly be seen in the verification cases in section 7.2. Nevertheless, an assessment of the sensitivity due to an uncertainty in the absorptivity and its influence induced under the current model is important. As the modeled surface coating are given as reflectivity data, which can be translated directly into absorptivity, the reflectance was varied in a range of $\delta\rho = \pm 5\%$ around the reference. Two analysis were performed because the two thermometers are modeled with differing surface coatings. As with the previous analysis, the histograms of the surface coating analyses are given in figure 8.10a and 8.10b for both the Earth angle and the Sun angle, respectively.

Tab. 8.5.: Statistics of THM absorptivity influence analysis for Earth and Sun angle for both thermometers.

Parameter	Dimension	Mean μ	Standard Deviation σ
THM 1 Absorptivity α_A	Earth angle β_E	1.11 rad	0.15 rad ²
	Sun angle β_S	0.47 rad	0.17 rad ²
THM 2 Absorptivity α_B	Earth angle β_E	1.25 rad	0.11 rad ²
	Sun angle β_S	0.91 rad	0.09 rad ²

Table 8.5 gives the statistical parameters of the angle distributions for the variation of the albedo for both thermometer coatings from figure 8.10. For the

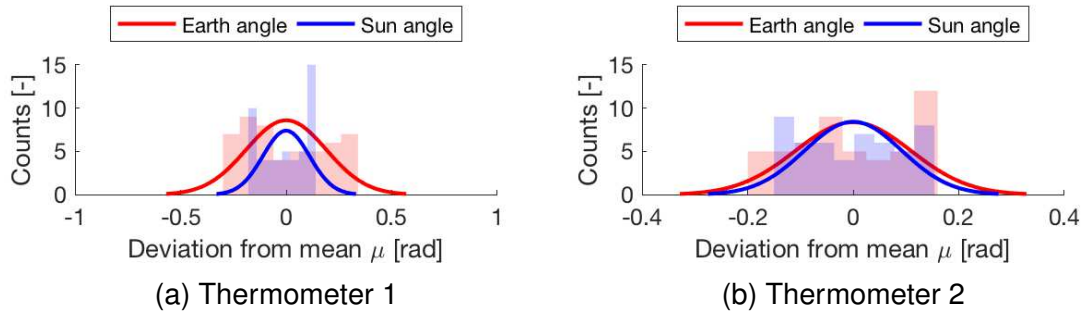


Fig. 8.10.: Histograms of the sensor's vector uncertainty due to uncertainties in the surface coatings: a) Variation of thermometer 1's spectral absorptivity $\alpha_{\lambda,1}$, b) Variation of thermometer 1's spectral absorptivity $\alpha_{\lambda,2}$. For both figures, the histogram and the fitted normal distribution are given for both Earth angle and Sun angle.

low absorptivity surface coating of THM 1 the 68% Earth vector error is $\delta\beta_{E,\sigma} \approx 0.15 \text{ rad} = 9.1^\circ$ and the 68% Sun vector error is $\delta\beta_{S,\sigma} \approx 0.17 \text{ rad} = 10.2^\circ$. In contrast, the 68% error due to variation of the high surface coating's absorptivity for the Earth angle is $\delta\beta_\sigma = 0.11 \text{ rad} = 6.3^\circ$ and $\delta\beta_\sigma = 0.09 \text{ rad} = 5.3^\circ$ for the Sun angle.

8.4.5. PCB Surface Coating

Comparing the surface areas of the PCB and the thermometers, it is obvious that the surface properties of the PCB have an influence on the sensor. To assess this influence, the absorptivity of the PCB was varied by $\pm 5\%$ around its nominal value, similarly to the procedure for the other surface properties. Figure 8.11 shows the histograms of the uncertainty in both the Sun and the Earth angle due to variation of the PCB's absorptivity.

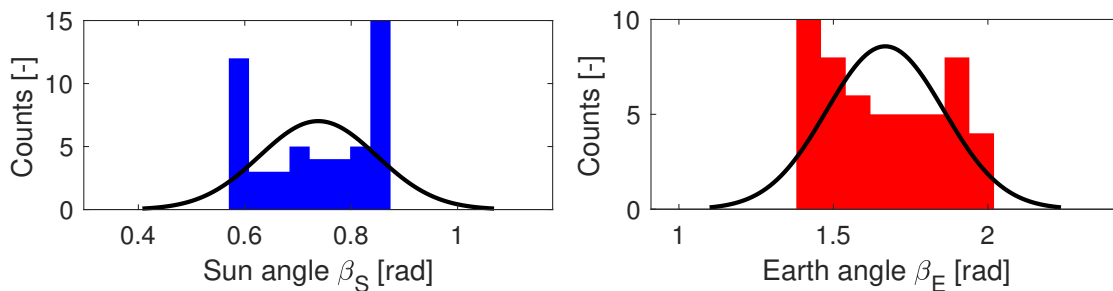


Fig. 8.11.: Histograms of the sensor's vector uncertainty due to uncertainties in the PCB coating for: a) the Sun angle β_S , b) the Earth angle β_E .

Table 8.2 gives the statistical parameters of the angle distributions for the variation of the PCB's absorptivity. The 68% Earth vector error is $\delta\beta_{E,\sigma} \approx 0.19 \text{ rad} = 10.9^\circ$ and the 68% Sun vector error is $\delta\beta_{S,\sigma} \approx 0.11 \text{ rad} = 6.3^\circ$. The spikes at the

Tab. 8.6.: Statistics of PCB absorptivity influence analysis for Earth and Sun angle.

Dimension	Mean μ	Standard Deviation σ
Earth angle β_E	1.67 rad	0.19 rad ²
Sun angle β_S	0.71 rad	0.11 rad ²

extrema of the histogram for the Sun angle come from the intersections reaching a parameter space boundary (usually ξ being zero or unity). Nevertheless, the statistics behave reasonably as the distribution is significantly broader.

8.4.6. Thermometer Thermal Mass

Apart from the uncertainties regarding the incident radiation, the model parameters for the THMs are estimations and, therefore, possibly subject to errors (see table 5.4). This analysis was conducted to estimate the uncertainty due to imprecise thermometer parameter. In the model, the volume, density and specific heat capacity form a compound usually referred to as thermal mass and it determines the thermal inertia, which is the responsiveness to change. Changing the thermal mass of the THM's should, therefore, yield different transient behavior. To demonstrate this influence, the thermal mass has been varied by changing the THM's specific heat capacity in a range of $\delta_{CTHM} = \pm 10\%$ around its respective reference in the model (see table 5.4). Figure 8.12a shows the influence of the thermal mass on the TOSS' accuracy and figure 8.12b shows the changing temporal behavior due to the change in the THM's thermal mass for a generic point in the parameter space.

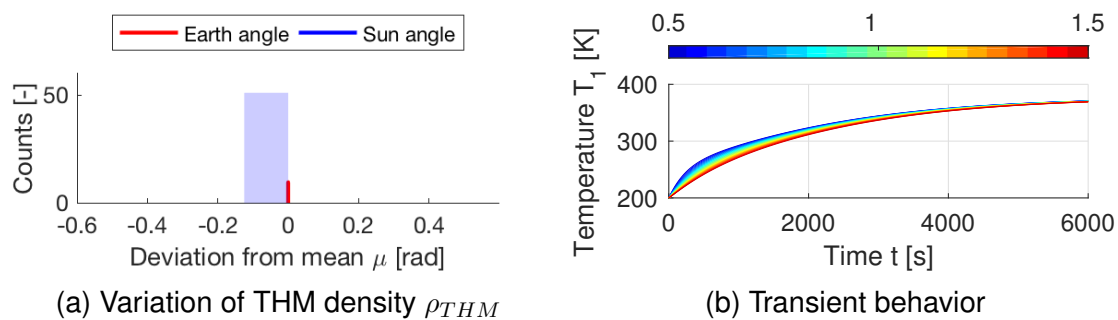


Fig. 8.12.: Plots of variations of the thermometer's thermal mass: a) Histograms of the sensor's vector uncertainty due to uncertainties in the thermal mass, b) Transient behavior of the sensor for a generic set of parameters and varying thermal masses. The colorbar indicates the relative change to the reference.

Table 8.7 gives the statistical parameters describing the data from PCB absorptivity variations in figure 8.12. As predicted, there is no loss in accuracy for

Tab. 8.7.: Statistics of thermometer's thermal mass influence analysis for Earth and Sun angle.

Dimension	Mean μ	Standard Deviation σ
Earth angle β_E	1.02 rad	0.0 rad ²
Sun angle β_S	0.63 rad	0.0 rad ²

change in the THM's thermal mass $\delta\beta_{S,\sigma} = \delta\beta_{E,\sigma} = 0^\circ$. In the histogram in figure 8.12a all values are binned to the same range and just one bar is visible. Here, the red line shows that deviations are negligible. However, the influence on the transient behavior of the sensor is clearly visible in figure 8.12b. Also, the convergence towards the same temperature is clearly visible.

8.4.7. Cutout Analysis

For the TOSSv2.2 board, the bases of the thermometers are separated from the rest of the board by having cutouts around them and connecting them only with a narrow bridge. In theory, this should make the sensor more responsive to changing thermal conditions because parasitic fluxes through the PCB are reduced. To assess the influence cutouts would have for the TOSSv3.0, the area between the nodes above which the THM's are mounted and their adjacent nodes was varied with a factor in the range from zeros to unity.

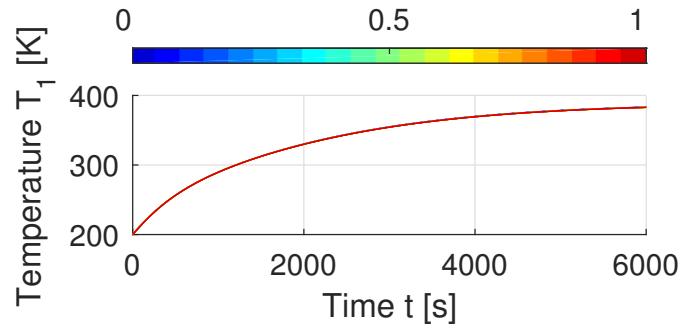


Fig. 8.13.: Transient temperature behavior for variation of the cutout factor.

Figure 8.13 depicts the temperature curves of THM 1 for variation of the cutout factor. All curves converge towards the same temperature which again shows that the cutouts do not affect the sensor's accuracy ($\delta\beta_{S,\sigma} = \delta\beta_{E,\sigma} = 0^\circ$). The cutout factor instead has an influence on the transient behavior. This effect is, however, minor compared to the influence other parameters have on the transient behavior, for example the THM's thermal mass.

Tab. 8.8.: Summary of 68% uncertainties obtained by OFAT analyses with the TOSS v3.0 model. For comparison, the values for the CESS are given [26].

Parameter	Input	Sun angle	Earth angle	Type
Sensor Uncertainty	± 0.5 K $\pm 0.2\%$ <i>I</i>	8.2°	7.0°	intrinsic
Albedo	$\pm 30\%$	0.4°	0.4°	extrinsic
Earth IR	$\pm 10\%$	0.7°	1.7°	extrinsic
Solar	$\pm 2\%$	0.5°	0.7°	extrinsic
Surface coating THM 1	$\pm 5\%$	9.1°	10.2°	intrinsic
Surface coating THM 2	$\pm 5\%$	5.3°	6.3°	intrinsic
Surface coating PCB	$\pm 5\%$	5.3°	6.3°	intrinsic
THM thermal mass	$\pm 5\%$	0°	0°	temporal
Cutouts	$\pm 5\%$	0°	0°	temporal
CESS		10°	15°	-

8.5. Discussion

Having performed sensitivity analyses for critical parameters, advantages and points for further improvement are revealed. Table 8.8 summarizes the findings.

Considering the general shapes of the isosurfaces, differences in the behaviors between the photo diode and the thermometers are apparent. The distinct shape of the photocurrent's isosurface compared to the shapes of the temperature's isosurfaces illustrates the importance of this measurement as it enables reliably finding an intersection and thus enabling attitude determination. In contrast, the rather similar shapes of the temperature isosurfaces is concerning because small changes in measurements can cause comparably big changes in position of the intersections between these two surfaces. This behavior is visible in figure 8.4. Here the intersections follow the shape of the temperature isosurfaces rather than the shape of the photocurrent isosurface.

Initially, possible errors in attitude determination due to the components' accuracy were analyzed and they are significant. As predicted, this is mostly due to uncertainties induced by thermometers. These DS18B20U thermometers are common COTS components, which are not designed for very high accuracy both rather for vast applicability and low cost. In comparison, the CESS uses high precision PT1000 thermometers, which can measure temperatures with a much higher accuracy. The photocurrent measurement process also introduces

uncertainties albeit with smaller influence. Thus, these uncertainties can be reduced by design and are classified as intrinsic.

Data from albedo variation shows very promising results. The low sensitivity of both Sun and Earth angle while being subject to major variation in albedo intensity, proves that the sensor can properly measure both Sun and Earth angle under albedo influence. By comparison, the influence Earth's IR radiation has on the sensor, is more significant. As these uncertainties can not be reduced by engineering effort, they are of extrinsic type. The uncertainties due to variation of the Sun-Earth distance are also extrinsic, as the movement of Earth can not be influenced. However, the position of Earth and thus its distance to the Sun can be precisely calculated. With this information uncertainties due to solar radiation variability could be reduced. Also the extrinsic uncertainties' magnitudes promise that small changes in solar radiation, for example from local changes on the Sun, would have a minor influence on the sensor's accuracy.

Much more significant are the uncertainties induced by the surface coatings. Especially for the low absorptivity coating of THM 1 slight variations can result in significant uncertainties in the direction measurements. THM 2 with its higher absorptivity is not as sensitive as THM 1, still it induces major uncertainties. Albeit the potential to induce uncertainty, this sensitivity also yields chances for better sensor design. For example, selecting specific materials as surface coatings or using spectral filters to prioritize wavebands could yield higher accuracy by focusing on a specific waveband. Detecting radiation only in a very narrow waveband and being sensitive to small changes could increase performance of the sensor.

Moreover, variations of the THM's thermal mass and board cutouts gave interesting results. Although the accuracy of the TOSS did not change, its temporal behavior changed. Using cutouts or reducing thermal mass of the thermometers reduces thermal inertia, indicating that change in attitude could be measured faster. As satellites are seldom in a stable position, orbit determination is a transient process and the sensor's transient behavior is important. Uncertainties with respect to this behavior are classified as temporal.

From the previous analyses and their statistics, it is obvious, that any TOSS is still subject to significant errors. Nevertheless, there are still statements which can be made to address these unwanted uncertainties. A distinction between different sources of uncertainties has been made between extrinsic, intrinsic and temporal uncertainties. Extrinsic sources cannot be reduced. For example, variation in Earth's albedo or its IR radiation are always present to some extent and a satellite in a LEO will always experience these variations. Extrinsic influences must be dealt with either by accepting loss in accuracy or by clever design of software and hardware. The hardware's physical properties could be changed to have reduced sensitivity to extrinsic sources of uncertainty, for example by changing the surface coating. Approaches regarding software solutions include signal filtering and model based simulations which has been shown to be possible in the previous chapter. In contrast, uncertainties in attitude determination

due to intrinsic sources can be reduced in the design process. Precise characterization of all sensor component properties has the potential to greatly reduce uncertainty in attitude determination. Especially the surface coating's radiant properties must be determined to a high degree of confidence. The hardware can also be adjusted to be less susceptible to variations by reducing dependencies and parameters. For example, the sensor, apart from the photo diode and one THM, could be coated equally which would eliminate one model parameter. As intrinsic sources of uncertainty can be addressed during development, they could theoretically be reduced to zero.

Considering all the uncertainties from parameters, the TOSS has the potential of reaching an 68% error for Sun's direction of $< 2^\circ$ and for Earth's direction of $< 3^\circ$ limited due to extrinsic influences. As there will always be uncertainties, even in a very highly developed system, these are ideal values and are hard to achieve. A good assumption for the current TOSS design is an accuracy of $< 20^\circ$ for both Sun and Earth direction.

Apart from considering the TOSS as a stand-alone sensor, the current TOSS could also be regarded as sensor head of a system combining multiple TOSS. The CESS uses this approach (see chapter 2). Combinations of TOSS measurements could then not only reduce uncertainty in the attitude determination when in regions with ambiguity for a vector but also increase the in other regions (see figure 8.1). Another benefit would be the gain of azimuth estimations, compared to pure elevation estimations returned by a single TOSS.

9. Conclusion

This chapter summarizes the thesis. Work, which has been done to model and analyze the TOSS, is presented and an outlook over future applications as well as possible improvements is given.

In this thesis, numerical models featuring important aspects of the existing TOSS variants have been developed together with a stable temporal implicit solver using Matlab. The model is highly modular which means that material parameters, radiation spectra and other settings defining the model can easily be changed in a separate Matlab struct. This enables quick changes in the model, which was extensively used for OFAT analysis, and allows easy implementation of new features. The thermal exchange mechanisms, which are featured in the model, are discussed in detail. Reliable information for the used material parameters and spectra are presented. Also, the photo diode has been modeled based on the basic photo-electric effect.

Following the model's built-up, generic test cases have been used to verify the solver and the numerical methods. These test cases show that the solver works properly and has no influence on the physical results. Using results from experiments in the RACOON-Lab with the TOSS v2.2 model, the model's physical parameters have been verified. The model's simulation results are in accordance with measurements from RACOON-Lab experiments. The uncertain parameter's values, for which the model shows the best agreement, were used for simulations of possible applications for a TOSS. Environmental differences between the RACOON-Lab and space have been assessed and removed.

With TOSS v3.0 simulations, it could be shown, that temperatures and photocurrent behave differently over the parameter space, forming the desired system of linearly independent variables. By finding isosurfaces for temperatures and photocurrent and their intersections, determination of the radiation's incident angles, which is the attitude determination, is possible. This method was used for evaluating OFAT analyses of model parameters, which showed to be influential during modeling. Statistical parameters were used to express the influence of model parameters on the attitude determination.

Therefore, the aims for this thesis stated in section 2.5 were fulfilled and the prove of concept that the Thermo-Optical Sun and Earth Sensor (TOSS) can function as a proper attitude determination sensor is achieved.

As discussed in the previous chapter, the current sources of uncertainty can be attributed to intrinsic and extrinsic phenomena. Neglecting the intrinsic sources of uncertainty, a TOSS or similar system can have an accuracy of $< 5^\circ$ for both Sun and Earth direction. Thus, the TOSS v3.0 sensor with its small form factor and its COTS components can achieve an accuracy comparable to the CESS, which has extensive flight heritage and was used in multiple high value missions

but is too big to fit onto a small satellite. Achieving this accuracy would, however, require further development.

Possible inhibitions for using a TOSS sensor are its uncertainties in Sun and Earth direction measurements. Whether coarse measurements are sufficient, must be decided individually. Currently, there is also significant numerical effort necessary to find intersections of isosurfaces. Considering that there is only limited space on the surface of a satellite and that any TOSS has to be on the surface, there might be problems positioning it, especially for small satellites.

With this in mind, the sensor should be used for initial acquisition, save mode or if only coarse attitude determination is necessary rather than for precision positioning. There are multiple advantages to be gained when using a TOSS or an equivalent composition of sensors and software. Firstly, a TOSS can provide small satellites with a coarse measurement for the Sun direction, which is important for numerous tasks on a satellite. Secondly, the nadir direction can be determined. Knowledge of the nadir is important, for example to ensure communication. Compared to common Sun sensors, which suffer from accuracy loss under albedo influence or can not determine the attitude when in Earth's shadow, the TOSS does function properly under both circumstances. Additionally, all TOSS versions have a theoretical FOV of 180° . As they use no shaders and have no structure above the thermometers and only insignificant amounts above the photo diode, its effective FOV will not be significantly reduced.

Referring back to the MOVE-II ADCS concept, the TOSS concept could possibly be applied to it even after its launch. Data from the satellite's Sun sensors and thermometers can provide the necessary information to gain a nadir direction estimation even without a sensor assigned to this measurement. Post-processing would require thermal modeling of the THM's behavior and subsequent simulations similarly to what has been done in this thesis.

For the TOSS, there are still points which require development and investigation. Improvements regarding the sensor's design include using components with higher accuracy and precise characterization of surface coating properties. Moreover, most material parameters used in this thesis are good estimation but still subject to uncertainties. Providing the model with more accurate data, inaccuracy of the model due to internal uncertainties could be reduced significantly. Further experiments under conditions closer to space, for example in a thermal-vacuum chamber or with a better characterized Sun simulator, could lead to much more precise data for some material parameters. Also tests with well characterized infrared radiation would be beneficial, as determination of Earth's direction relies on this radiation. As satellites are moving objects, future development should be done in order to obtain a method for transient attitude determination based on the model data. Cutouts and shielding the PCB from radiation could also yield a better transient performance which has to be investigated in depth. Here, a promising approach, which is also used in the CESS's flight software, is extrapolation of short time measurements to static temperatures and finding the intersection for these temperatures, which yields current

attitude estimations. Furthermore, installing multiple TOSS onto different satellite surfaces and combining their measurements would increase the system's fidelity. Besides that, combination of a fine Sun sensor, such as a NANO-ISS60, with specifically coated thermistors and a model describing the behavior might set new standards in albedo influence resistant attitude determination sensors for small satellites.

A. Bibliography

- [1] J. R. Wertz, ed., *Spacecraft Attitude Determination and Control*. Springer Netherlands, 1978.
- [2] M. Swartwout, "You say "Picosat", I say "CubeSat": Developing a better taxonomy for secondary spacecraft," in *2018 IEEE Aerospace Conference*, IEEE, Mar. 2018.
- [3] X. Xia, G. Sun, K. Zhang, S. Wu, T. Wang *et al.*, "NanoSats/CubeSats ADCS survey," in *29th Chinese Control And Decision Conference (CCDC)*, IEEE, May 2017.
- [4] L. Stras, D. D. Kekez, G. J. Wells, T. Jeans, R. E. Zee *et al.*, "The design and operation of the Canadian advanced nanospace eXperiment (CanX-1)," in *Proc. AMSAT-NA 21st Space Symposium, Toronto, Canada*, pp. 150–160, 2003.
- [5] The CubeSat Program, Cal Poly SLO, "CubeSat Design Specification," 2018. visited 2018-10-18 [Online] <http://www.cubesat.org/resources/>.
- [6] R. Hevner, W. Holemans, J. Puig-Suari, and R. Twiggs, "An advanced standard for CubeSats," *25th Annual AIAA/USU Conference on Small Satellites*, 2011.
- [7] J. Wells, L. Stras, and T. Jeans, "Canada's smallest satellite: The Canadian advanced nanospace experiment (CanX-1)," in *16th Annual AIAA/USU Conference on Small Satellites*, 2002.
- [8] W. J. Larson and J. R. Wertz, *Space Mission Analysis and Design, Space Technology Library*. Microcosm Press and Kluwer Academic Publishers, El Segundo, CA, USA, 3rd ed., 1999.
- [9] TY-Space (Beijing) Ltd., "Nano Star Tracker NST-4," Sept. 2018. visited 2018-10-18 [online] http://www.ty-space.com/en/product_details.php?id=16.
- [10] CubeSatShop.com, "NST-3 Nano Star Tracker," 2018. visited 2018-10-18 [Online] <https://www.cubesatshop.com/product/nst-1-nano-star-tracker/>.
- [11] National Aeronautic and Space Agency (NASA), "Spacecraft Earth Horizon Sensors," tech. rep., NASA Electronics Research Center; Cambridge, MA, United States, 1969. NASA Sp-8033.
- [12] New Space Systems (Pty) Ltd., SA, "NCSS-SA05 / NFSS-411 Performance," 2018. version 6a.

- [13] National Aeronautic and Space Agency (NASA), "Spacecraft Sun Sensors," tech. rep., NASA Electronics Research Center; Cambridge, MA, United States, 1970. NASA SP-8047.
- [14] Lens Research & Developement, NL, "Lens R&D Product and Price Catalogue," 2017.
- [15] Solar MEMS Technologies, "Sun Sensor NANO-ISSX/c. Technical Specifications.," 2014. version 1.04.
- [16] NanoAvionics , "Flight Proven Subsystems," 2018. visited 2018-10-18 [Online] <https://n-avionics.com/subsystems/>.
- [17] C. Hall, "Attitude Determination," tech. rep., University of New Mexico, 2003.
- [18] D. Brasoveanu and J. Sedlak, "Analysis of earth albedo effect on sun sensor measurements based on theoretical model and mission experience," tech. rep., National Aeronautic and Space Agency, 1998. [Online] <https://ntrs.nasa.gov/search.jsp?R=19980203812>.
- [19] G. L. Stephens, D. O'Brien, P. J. Webster, P. Pilewski, S. Kato *et al.*, "The albedo of Earth," *Reviews of geophysics*, vol. 53, no. 1, pp. 141–163, 2015.
- [20] SpaceTech GmbH, "Coarse Earth Sun Sensor (CESS)," 2018. visited 2018-10-18 [Online] <https://spacetechnology.com/products/satellite-equipment/cess>.
- [21] M. Langer, N. Appel, M. Dziura, C. Fuchs, P. Günzel *et al.*, "MOVE-II-der zweite Kleinsatellit der Technischen Universität München," in *Deutscher Luft- und Raumfahrtkongress*, Deutsche Gesellschaft für Luft- und Raumfahrt-Lilienthal-Oberth eV, 2015.
- [22] M. Langer, C. Olthoff, J. Harder, C. Fuchs, M. Dziura *et al.*, "Results and lessons learned from the cubesat mission first-move," *Small Satellite Missions for Earth Observation*, R. Sandau, H.-P. Roeser und A. Valenzuela, Springer Berlin Heidelberg, 2015.
- [23] D. Messmann, T. Grübler, F. Coelho, T. Ohlenforst, J. Van Bruegge *et al.*, "Advances in the Development of the Attitude Determination and Control System of the CubeSat MOVE-II," in *Proceedings of the 7th European Conference for Aeronautics and Space Sciences (EUCASS)*, July 2017. DOI: 10.13009/EUCASS2017-660.
- [24] Maxim Integrated, "DS18B20. Programmable Resolution 1-Wire Digital Thermometer," 2015. 19-7487; Rev 4; 1/15.
- [25] B. Doll and W. Pitz, "Grober Sonnen- oder Erdsensor für einen Satelliten sowie Verfahren zur groben Positionsbestimmung von Sonne oder Erde an Bord eines Satelliten," 1997. EP0863075A1.

- [26] SpaceTech GmbH, “Coarse Earth Sun Sensor (CESS),” 2015. visited 2018-10-18 [Online] http://www.spacetechnology.com/images/products/satellite_equipment/cess/DataSheet_HCESS.pdf.
- [27] M. Dziura, C. Gscheidle, and M. Langer, “A Compact Thermo-Optical Sun and Earth Sensor for Small Satellites,” in *69th International Astronautical Congress 2018*, Oct. 2018. IAC-18.B4.6B.8x46078.
- [28] Vishay Semiconductors, “BPW34 Silicon PIN Photodiode Datasheet,” 2018. visited 2018-10-18 [Online] <https://www.vishay.com/docs/81521/bpw34.pdf>.
- [29] H. D. Baehr and K. Stephan, *Wärme-und Stoffübertragung*, vol. 2. Springer, 9th ed., 2016.
- [30] W. Polifke and J. Kopitz, *Wärmeübertragung: Grundlagen, analytische und numerische Methoden*. Pearson Deutschland GmbH, 2nd ed., 2009.
- [31] Verein Deutscher Ingenieure VDI-Gesellschaft Verfahrenstechnik und Chemieingenieurwesen (VCI), ed., *VDI Heat Atlas*. Springer-Verlag GmbH, 2010.
- [32] I. Martinez, “Radiative View Factors,” tech. rep., Ciudad Universitaria, Madrid, 2018.
- [33] K. R. Lang, *A companion to astronomy and astrophysics: chronology and glossary with data tables*, vol. 830. Springer Science & Business Media, 2007.
- [34] W. M. Haynes, *CRC Handbook of Chemistry and Physics*. Boca Raton, FL: CRC Press, Internet Version 2005.
- [35] A. Adibekyan, E. Kononogova, C. Monte, and J. Hollandt, “High-Accuracy Emissivity Data on the Coatings Nextel 811-21, Herberts 1534, Aeroglaze Z306 and Acktar Fractal Black,” *International Journal of Thermophysics*, vol. 38, no. 6, p. 89, 2017.
- [36] C. Fröhlich and J. Lean, “Total solar irradiance variations,” in *International Astronomical Union Symposium 185: New Eyes to See Inside the Sun and Stars*, pp. 89–102, 1998.
- [37] T. N. Woods, D. K. Prinz, G. J. Rottman, J. London, P. C. Crane *et al.*, “Validation of the UARS solar ultraviolet irradiances: Comparison with the ATLAS 1 and 2 measurement,” *Journal of Geophysical Research*, vol. 101, pp. 9541–9569, 1996.
- [38] ASTM International, “Standard Solar Constant and Zero Air Mass Solar Spectral Irradiance Tables,” tech. rep., ASTM International, West Conshohocken, 2018. DOI: 10.1520/e0490-00ar14.

- [39] ASTM International, “ASTM G173-03(2012), Standard Tables for Reference Solar Spectral Irradiances: Direct Normal and Hemispherical on 37 Tilted Surface,” tech. rep., ASTM International, West Conshohocken, 2012. DOI: 10.1520/G0173-03R12.
- [40] R. C. Willson and H. S. Hudson, “The Sun’s luminosity over a complete solar cycle,” *Nature*, vol. 351, no. 6321, p. 42, 1991.
- [41] D. R. Williams, “Sun Fact Sheet,” tech. rep., NASA Goddard Space Flight Center, 2018. visited 2018-10-18 [Online] <https://nssdc.gsfc.nasa.gov/planetary/factsheet/sunfact.html>.
- [42] National Aeronautic and Space Agency (NASA), “Earth Albedo and Emitted Radiation,” tech. rep., NASA Electronics Research Center; Cambridge, MA, United States, 1971. NASA SP-8067.
- [43] R. Peyrou-Lauga, “Using real Earth Albedo and Earth IR Flux for Spacecraft Thermal Analysis,” in *47th International Conference on Environmental Systems*, 2017.
- [44] A. Berk, L. Bernstein, and D. Robertson, “MODTRAN: A Moderate Resolution Model for LOWTRAN,” tech. rep., Air Force Geophysics Laboratory, Hanscom Air Force Base, Massachusetts, 01731, 1987.
- [45] University of Chicago, “MODTRAN web application,” 2018. visited 2018-10-18 [Online] <http://climatemodels.uchicago.edu/modtran/modtran.html>.
- [46] Vishay Semiconductors, “Measurement Techniques,” tech. rep., Vishay Semiconductors GmbH, 2018. visited 2018-10-18 [Online] <https://www.vishay.com/docs/80085/measurerm.pdf>.
- [47] OSI Optoelectronics, “Photodiode Characteristics and Applications,” 2018. visited 2018-10-18 [Online] <http://www.osioptoelectronics.com/application-notes/an-photodiode-parameters-characteristics.pdf>.
- [48] Vishay Semiconductors, “Physics and Technology,” tech. rep., Vishay Semiconductors GmbH, 2018. visited 2018-10-18 [Online] <https://www.vishay.com/docs/80086/physics.pdf>.
- [49] Dielectric Corporation, “G-10 / FR-4 / G-11 (Glass-Epoxy) General Material Properties,” Online 2018. visited 2018-10-18 [Online] <http://www.dielectriccorp.com/downloads/thermosets/glass-epoxy.pdf>.
- [50] F. Sarvar, N. J. Poole, and P. A. Witting, “Pcb glass-fibre laminates: Thermal conductivity measurements and their effect on simulation,” *Journal of Electronic Materials*, vol. 19, pp. 1345–1350, Dec 1990.
- [51] OshPark LLC, “2 Layer Prototype Service,” Sept. 2018. visited 2018-10-18 [Online] <https://docs.oshpark.com/services/two-layer/>.
- [52] R. Franz and G. Wiedemann, “Ueber die Wärme-Leitungsfähigkeit der Metalle,” *Annalen der Physik und Chemie*, vol. 165, no. 8, pp. 497–531, 1853.

- [53] C. Karpfinger, *Höhere Mathematik in Rezepten*. Heidelberg, Berlin: Springer, 2014.
- [54] J. Harder, M. Dziura, and S. Haberl, "Future Technologies for Operating Robots in Space," in *68th International Astronautical Congress 2017*, Sept. 2017. IAC-17,D1,6,7,x38585.
- [55] A. Ciadamidaro, "Auslegung und Konstruktion eines Sonnensimulators für eine Simulationsumgebung zur Nahbereichsnavigation von Satelliten," 2016. Bachelor thesis at Chair of Astronautics (LRT), Technical University of Munich (TUM).
- [56] INS Instrumentation, "DX-100 Specification," 2018. visited 2018-10-18 [Online] <http://www.inss.com.tw/ep-3.htm>.
- [57] M. Burkhardt, "Test Bed for CubeSat Attitude Determination Systems," 2015. Semester thesis at Chair of Astronautics (LRT), Technical University of Munich (TUM).
- [58] J. Tuszynski, "Surface Intersection," 2014. visited 2018-10-18 [Online] <https://de.mathworks.com/matlabcentral/fileexchange/48613-surface-intersection>.
- [59] Atmel, "ATtiny25/V / ATtiny45/V / ATtiny85/V. Atmel 8-bit AVR Microcontroller with 2/4/8K Bytes In-System Programmable Flash," 2013. Rev. 2586Q–AVR–08/2013, visited 2018-10-18 [Online] http://ww1.microchip.com/downloads/en/DeviceDoc/atmel-2586-avr-8-bit-microcontroller-attiny25-attiny45-attiny85_datasheet.pdf.
- [60] U. Walter, *Astronautics - The Physics of Space Flight*. Wiley-VCH Verlag & Co. KGaA, 2., enl. a ed., 2012.
- [61] A. Roach, *Statistik für Ingenieure*. Berlin Heidelberg: Springer-Verlag GmbH, 2014.
- [62] U. Walter, "Datenanalyse, Mittelwerte und Fehlerfortpflanzung," tech. rep., Chair of Astronautics (LRT), Technical University of Munich (TUM), 2018.

B. Statistics

In reality, measurements of physical quantities are subject to uncertainties and these uncertainties can be sources of errors and misinterpretation. It is therefore important to determine and describe uncertainties and how they propagate through a model. This section's formulas and equations are based on Rooch, 2014 [61] and Walter, 2018 [62]. When considering the grade of any measurement, two key terms are unavoidable. Accuracy is regarded to describe how close a measurement is to its actual or agreed on value. Precision is the degree of reliability of a measurement regardless of its value. It also gives a degree of reproducibility as very precise measurements do not deviate from the average. Figure B.1 gives a graphical example for accuracy and precision for an arbitrary measurement. A good measurement is accurate and precise, meaning that it closely represents the actual value and has negligible deviation from it for multiple measurements.

B.1. Stochastic Methods

For an infinite amount of measurements, the result's distribution follows an underlying statistical probability distribution function. It determines how often a result can be expected. One of the most common distributions is the Gaussian Normal Distribution $\mathcal{N}(\mu, \sigma^2)$ given in equation B.1. Most measurement errors are normally distributed and knowledge on the normal distribution is essential for making statements on the quality of measurements.

$$\phi(x) = \mathcal{N}(x|\mu, \sigma^2) = \frac{1}{\sqrt{2\pi\sigma^2}} \exp\left(-\frac{(x - \mu)^2}{2\sigma^2}\right) \quad (\text{B.1})$$

In equation B.1, μ is the expectation and σ^2 is the variance. Figure B.2 depicts the standard probability distribution $\mathcal{N}(\mu = 0, \sigma^2 = 1)$. The expectation μ indicates the value with the highest probability and σ^2 indicates the width of the

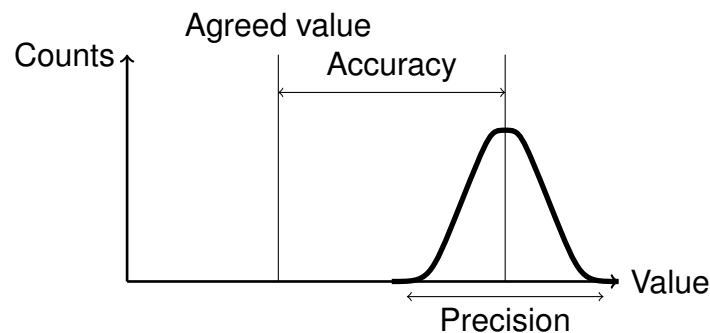


Fig. B.1.: Graphical representation of accuracy and precision for an arbitrary measurement.

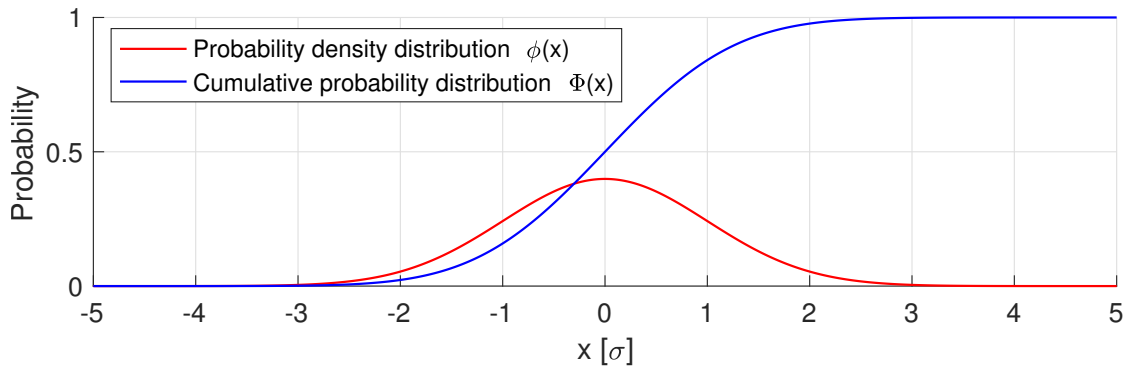


Fig. B.2.: Probability density function $\phi(x)$ and cumulative distribution function $\Phi(x)$ of the Gaussian Normal Distribution $\mathcal{N}(0, 1)$.

curve. With the transformation $z = (x - \mu)/\sigma$ any normal distribution can be translated to the plotted standard normal distribution. Therefore, the standard normal distribution will be analyzed further.

For analysis, the cumulative probability Φ is an important function which is the integration of the probability density p up to a specific value with equation B.2. The cumulative probability is also plotted in figure B.2.

$$\Phi(z) = \frac{1}{\sqrt{2\pi}} \int_{-\infty}^z e^{-\frac{t^2}{2}} dt \quad (\text{B.2})$$

This function is used when determining confidence intervals which describe with what probability a random single event from the underlying normal distribution is within a value range. For the standard normal distribution, the share of values within the range

- $(\mu - 1\sigma, \mu + 1\sigma)$ is about 68.3 %,
- $(\mu - 2\sigma, \mu + 2\sigma)$ is about 95.5 %,
- $(\mu - 3\sigma, \mu + 3\sigma)$ is about 99.7 %.

In general, for any given probability p the interval $(\mu - \Upsilon\sigma, \mu + \Upsilon\sigma)$ can be determined with the result from equation B.3

$$\Upsilon(p) = \Phi^{-1} \left(\frac{p+1}{2} \right) \quad (\text{B.3})$$

where Φ^{-1} is the inverse of the cumulative probability distribution function.

B.2. Discrete Statistics

However, it is clearly impossible to obtain an infinite amount of measurements and the parameters for the expectation μ and the variance σ have to be esti-

mated. For a set of n measurements x_i , where $i = 1, \dots, n$, the sample mean is computed with equation B.4.

$$\bar{x} = \frac{1}{n} \sum_{i=1}^n x_i \quad (\text{B.4})$$

It is the result of the maximum likelihood estimation and therefore the maximum likelihood estimator for the expectation. The same analysis yields the maximum likelihood estimator for the variance, which is called unbiased sample variance and is given in equation B.5.

$$s_x^2 = \frac{1}{n-1} \sum_{i=1}^n (x_i - \bar{x})^2 \quad (\text{B.5})$$

The corrected sample standard deviation of the dataset x can be calculated from the unbiased sample variance with the equation $s_x = \sqrt{s_x^2}$. Since these two parameters are estimates, their values should be treated with care. When dealing with empiric data, values of a quantity x are commonly given as an expectancy or mean value \bar{x} and an uncertainty or error δx , $x = \bar{x} \pm \delta x$. In accordance with the previous section, the data is given in a confidence interval. For a probability of $p = 95\%$, the value with its confidence interval can be reported as $x = \bar{x} \pm 1.96\sigma_x$, since $\Upsilon(p = 0.95) = 1.96$.

Furthermore, both the sample mean and the sample variance are estimates and not certain as they originate from empiric data with finite samples. In order to make a statement on the estimation's quality, confidence intervals can be given, which state the boundaries of a probability for the value being within for infinitely many data points. Confidence intervals for the mean and the variance at a given probability p can be calculated with equation B.6 and B.7, respectively.

$$\bar{x} \in \left[\bar{x} - t_{n-1, 1-p/2} \sqrt{\frac{s_x^2}{n}}, \bar{x} + t_{n-1, 1-p/2} \sqrt{\frac{s_x^2}{n}} \right] \quad (\text{B.6})$$

$$s_x^2 \in \left[\frac{(n-1)s_x^2}{\chi_{n-1, 1-p/2}^2}, \frac{(n-1)s_x^2}{\chi_{n-1, p/2}^2} \right] \quad (\text{B.7})$$

Here $t_{n,p}$ is the p interval of the Student's t distribution with n degrees of freedom and $\chi_{n,p}^2$ is the p interval of the χ^2 distribution with n degrees of freedom. The values of these distributions and their inverse are available in most programs or in tabled form and are not further analyzed.

B.3. Linear Regression

When one suspects a linear relationship between two parameters, linear regression is a method for determining this relationship by finding a line which fits through the given data with minimal squared errors. For a set of data points

(x_i, y_i) with $i \in [1, n]$, a linear regression line has the equation $y = \hat{a} + \hat{b}x$. The slope of the regression line \hat{b} can be calculated with equation B.8

$$\hat{b} = \frac{\sum_{i=1}^n (x_i - \bar{x})(y_i - \bar{y})}{\sum_{i=1}^n (x_i - \bar{x})^2} \quad (\text{B.8})$$

and the formula for the y-intercept \hat{a} is given in B.9.

$$\hat{a} = \bar{y} - \hat{b}\bar{x} \quad (\text{B.9})$$

As the regression is focus on minimizing the squared errors, there are likely still deviations in the data from the model. The remaining errors are described by the variance, which is calculated with equation B.10.

$$s_{y|x}^2 = \frac{1}{n-2} \sum_{i=1}^n (y_i - \hat{a} - \hat{b}x_i)^2 \quad (\text{B.10})$$

To put the regression's variance into context, the coefficient of determination R^2 can be determined, as defined in equation B.11.

$$R^2 = 1 - \frac{s_{y|x}^2}{s_{y|\bar{x}}^2} \quad (\text{B.11})$$

It compares the regression's variance to the variance of a dataset with only its mean value and thus gives an indication of how good the fit is. Values close to unity indicate that the variance after regression, and thus the remaining errors, are small in comparison with the errors before the regression.

As the regression coefficients \hat{a} and \hat{b} are again both estimates, the formulas for calculating their confidence intervals of probability p are given in equations B.12 and B.13.

$$\hat{a} \pm t_{n-1, (1-p)/2} \sqrt{s_{y|x}^2} \left(\frac{\sum_{i=1}^n x_i^2}{\sum_{i=1}^n (x_i - \bar{x})^2} \right)^{1/2} \quad (\text{B.12})$$

$$\hat{b} \pm t_{n-1, (1-p)/2} \sqrt{s_{y|x}^2} \left(\frac{1}{\sum_{i=1}^n (x_i - \bar{x})^2} \right)^{1/2} \quad (\text{B.13})$$

For the estimated variance of the remaining errors the confidence interval of probability p is given in equation B.14

$$\left[\frac{(n-2)s_{y|x}^2}{\chi_{n-2, (1-p)/2}^2}, \frac{(n-2)s_{y|x}^2}{\chi_{n-2, p+(1-p)/2}^2} \right] \quad (\text{B.14})$$

These formulas are slightly different, because they rely on two normal distributed data sets.

Tab. B.1.: Error propagation for addition, multiplication and raising to power.

Operation $z =$	Mean $\bar{z} =$	Uncertainty $\delta z =$
Addition $ax + by$	$a\bar{x} + b\bar{y}$	$\sqrt{a^2\delta x^2 + b^2\delta y^2}$
Multiplication $\frac{ax}{y}$	$\frac{\bar{a}\bar{x}}{\bar{y}}$	$\bar{z}\sqrt{\left(\frac{\delta a}{a}\right)^2 + \left(\frac{\delta x}{x}\right)^2 + \left(\frac{\delta y}{y}\right)^2}$
Raising to power $x^n y^m$	$\bar{x}^n \bar{y}^m$	$\bar{z}\sqrt{\left(\frac{n\delta x}{x}\right)^2 + \left(\frac{m\delta y}{y}\right)^2}$

B.4. Error Propagation

For quantities $x_i = \bar{x}_i \pm \delta x_i, i \in [1, n]$, which are associated with individual uncertainties, the result after an operation on them $z = f(x_1, x_2, \dots, x_n) = \bar{z} \pm \delta z$ is described in the following equations. The result's mean is given in equation B.15 and is calculated by evaluating the function at the input's mean values.

$$\bar{z} = f(\bar{x}_1, \bar{x}_2, \dots, \bar{x}_n) \quad (\text{B.15})$$

The result's uncertainty can be calculated with equation B.16. Although, this formula gives the result's mean uncertainty. If the maximum is of interest, the sum of the input's absolute uncertainties has to be calculated.

$$\delta z = \sqrt{\sum_{i=1}^n \left(\frac{\partial f}{\partial x_i}\right)^2 \delta x_i^2} \quad (\text{B.16})$$

The calculation of the partial derivatives can become challenging for complex functions and sensitivity analysis should be performed. However, for some basic operations table B.1 lists the formulas for uncertainty calculation.

C. Additional Figures

C.1. RACOON-Lab Experiments

Tab. C.1.: RACOON-Lab Experiment Parameters from the first campaign. Experiments 4-6 differ from experiments 1-3 due to a dark cloth being used to prevent reflections from the test bench. Experiments are therefore not used for verification.

Test	Orientation	Distance [m]	Rotation rate [rpm]	Angle range [deg]
1	horizontal	0.9	1	0 - 315
2	horizontal	0.9	0.5	0 - 315
3	horizontal	0.9	-2	0 - 315
4	horizontal	0.9	0.5	0 - 315
5	horizontal	0.9	-2	0 - 315
6	horizontal	0.9	1	0 - 315
7	horizontal	0.5	1	0 - 315
8	horizontal	0.5	-2	0 - 315
9	horizontal	0.5	0.5	0 - 315
10	vertical	0.5	0	0
11	vertical	0.5	0.1	0 - 315
12	vertical	0.5	0	45
13	vertical	0.5	0	-45
14	vertical	0.9	0	0
15	vertical	0.7	0	0

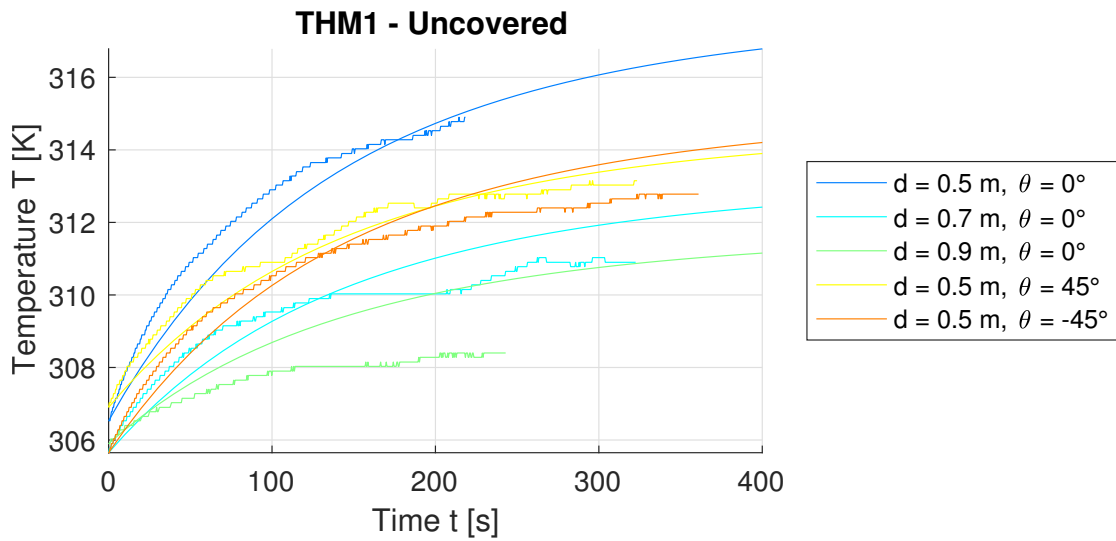


Fig. C.1.: Temperatures of thermometer THM1: Simulated using the adapted TOSS v2.2 model and measured in the RACOON-Lab experiments. The sensor's surface was not coated.

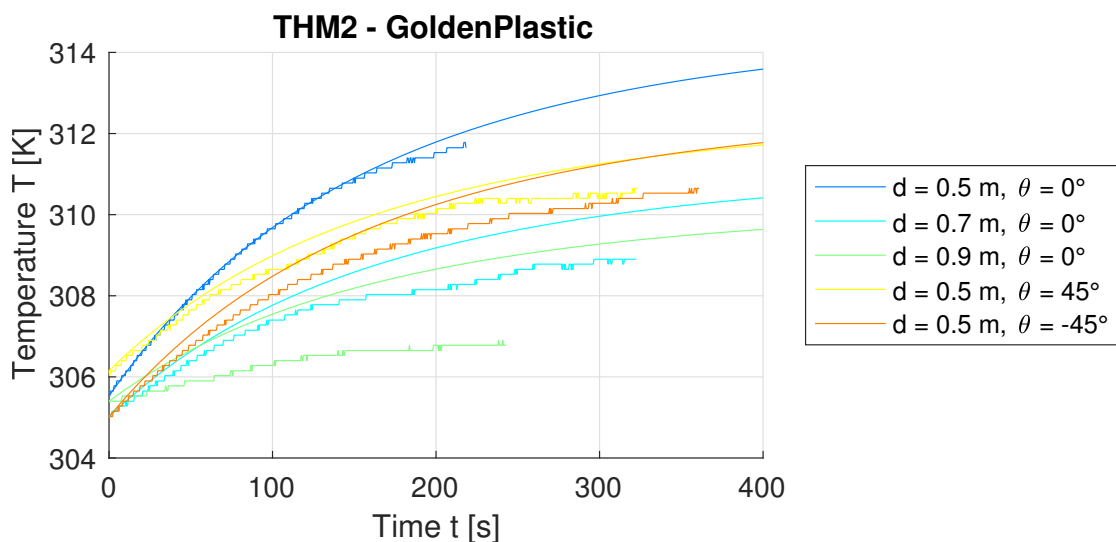


Fig. C.2.: Temperatures of thermometer THM2: Simulated using the adapted TOSS v2.2 model and measured in the RACOON-Lab experiments. The sensor's surface was coated with a golden plastic foil.

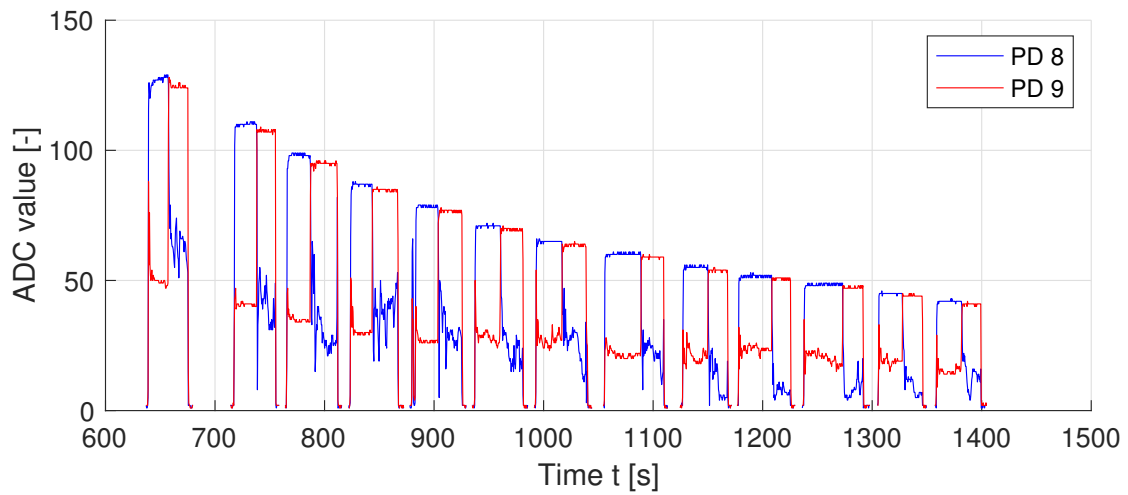


Fig. C.3.: Raw measured ADC values from photo diode 8 and 9 over time. The distance from the light source was increased from $d_1 = 0.3$ m to $d_2 = 1.5$ m by 10 cm for each measurement.

C.2. TOSS Schematics

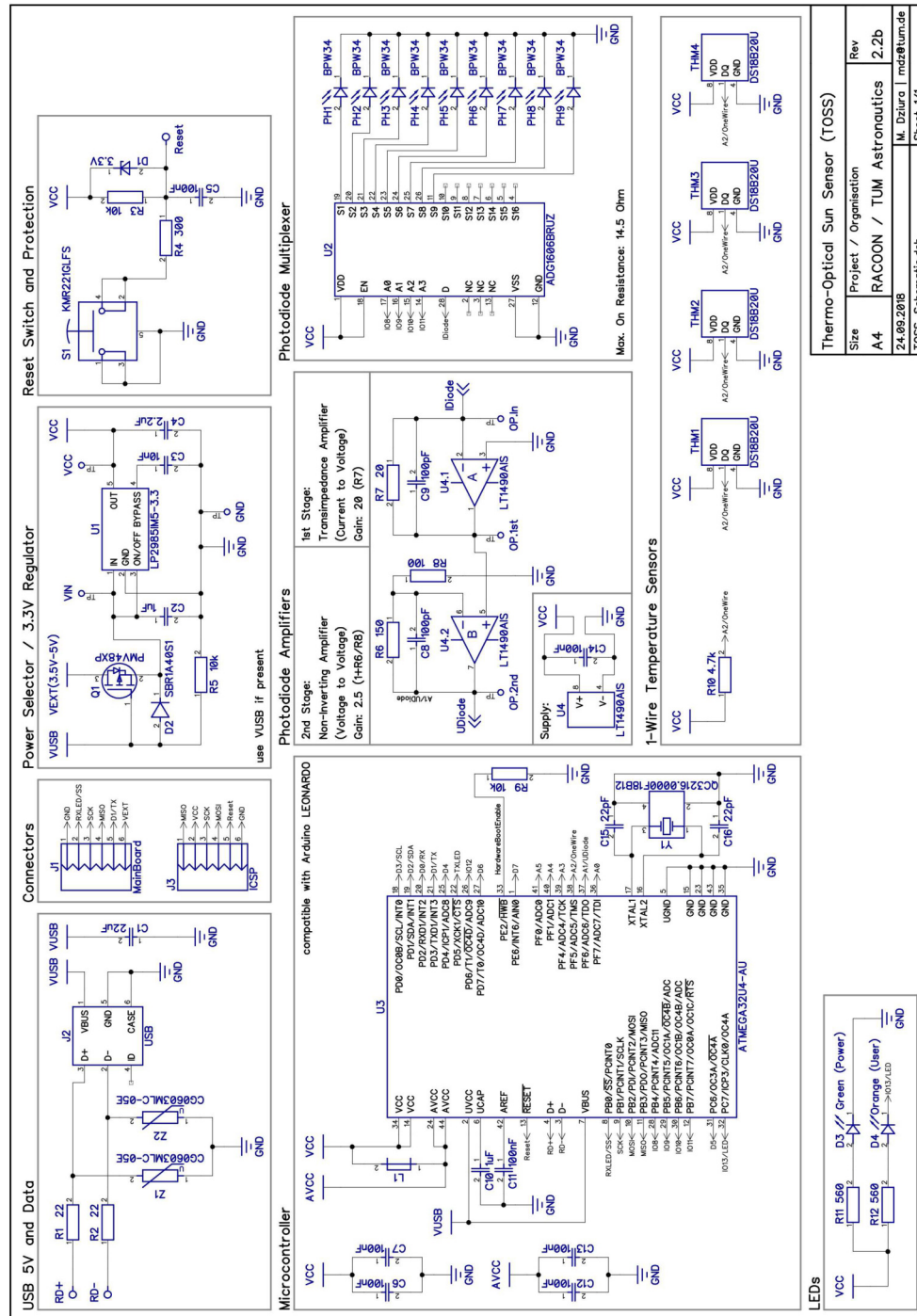


Fig. C.4.: Schematic of the TOSS v2.2 sensor board [27].

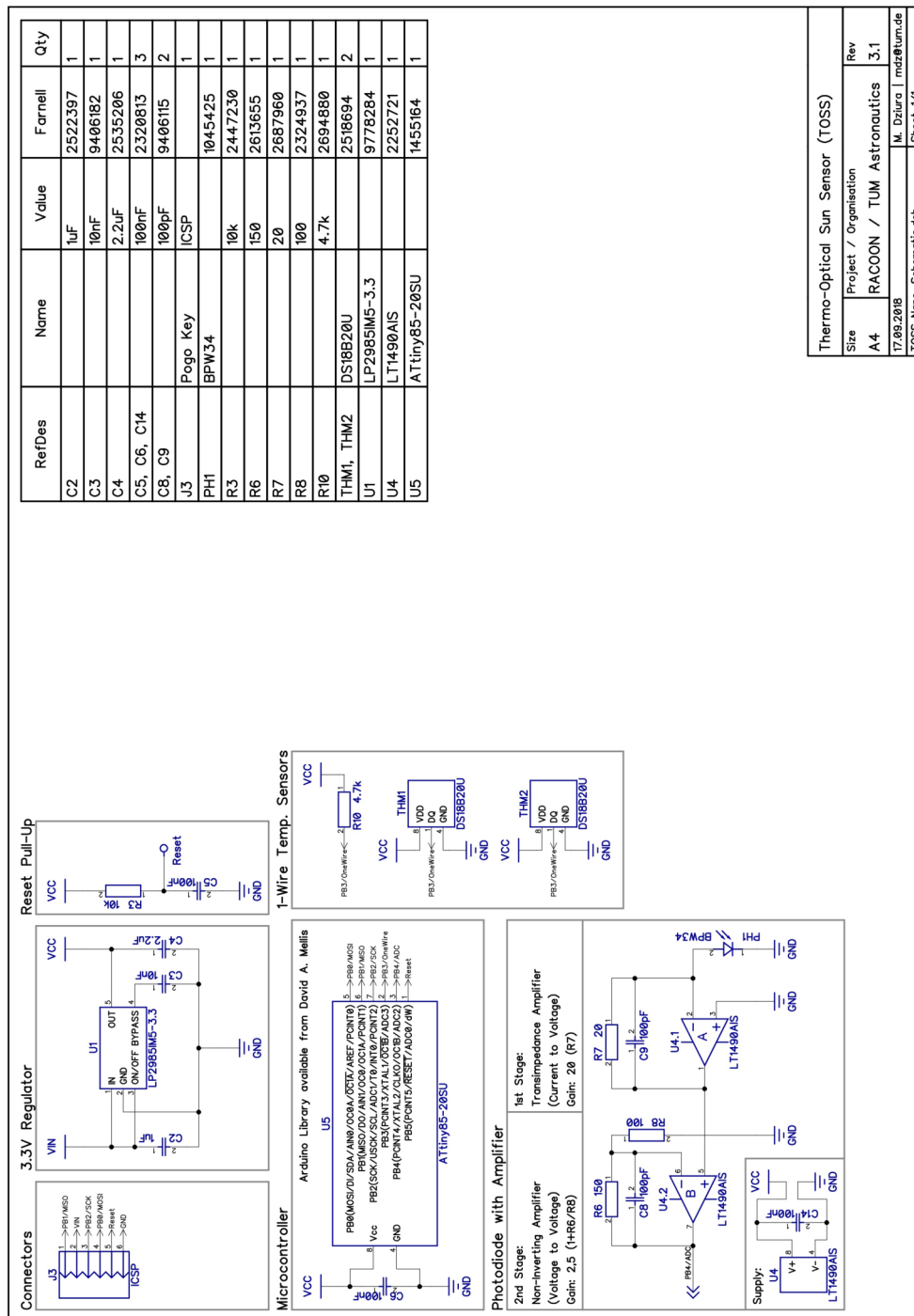


Fig. C.5.: Schematic of the TOSS v3.0 sensor board [27].

C.3. Matlab Struct

In the following a generic TOSS v3.0 model struct is presented.

```
%% Main Struct defining the TOSS v3.0 model
%% Remove possible old model struct
clear model
model.Path.Source = '/Users/christiangscheidle/Documents/Uni/MA';
addpath([model.Path.Source filesep 'Programcode/Matlab']);
model.Path.Figures = [model.Path.Source filesep 'Ausarbeitung/fig'];

%% Debugging flags
model.DEBUG.showTgrid = 0;
model.DEBUG.showSensorLines = 0;
model.DEBUG.displayResults = 0;
model.DEBUG.showSpy = 0;
model.DEBUG.ExtendedOutput = 0;
model.DEBUG.showEnv = 0;

%% Solver settings
model.solver.T_init_mode = 'constant';
model.solver.T_init = 200; %[K] initial temperature
model.solver.dt = 60; %[s] time increment
model.solver.stop_crit = 1e-3; %[K] stop criteria temperature difference
model.solver.maxIter = inf; %[-] maximum number of iterations

%% Sensor board geometry
model.geo.elements = 9; %[-] number of elements (outer ring plus middle)
model.geo.thickness = 0.003; %[m] PCB thickness
model.geo.radius = 0.02; %[m] PCB radius
model.geo.cutoutfactor = 1;

%% Natural constants
model.const.q = 1.60217653e-19; %elementary charge [C = J V^-1]
model.const.h = 6.6260693e-34; %Planck constant [J s]
model.const.c = 2.99792458e8; %speed of light in vacuum [m s^-1]
model.const.k = 1.38064852e-23; %Boltzmann constant [J K^-1]
model.const.sigma = 5.67e-8; %Stefan-Boltzmann constant [W m^-2 K^-4]

%% Orbit geometry parameter
model.orbit.SMA = 1.4960e11; %[m]
model.orbit.ECC = 1.67086e-2; %[-]
model.orbit.INC = 1.578690; %[deg]
model.orbit.LOP = 102.9; %[deg]
model.orbit.RAN = 174.9; %[deg]
model.orbit.AOP = 288.1; %[deg]
model.orbit.R_E = 6.3710008e6; %[m] WGS84 Radius of Earth
model.orbit.R_S = 6.96342e8; %[m] Radius of the Sun
model.orbit.h_sat = 4e5; %[m]
model.orbit.T_space = 2.73; %[K] temperature of deep space
model.orbit.T_Earth_mean = 297; %[K] mean black body temperature of Earth
model.orbit.R_O_ref = model.orbit.SMA;
model.orbit.R_O = model.orbit.SMA;
model.orbit.gamma_D = 2; %[-] distance attenuation factor {0,2}
```



```

%% Spectra of irradiance
model.spec.path = [model.Path.Source filesep 'Messdaten/01 Spectra'];
addpath(model.spec.path);
load('IR_spec_MODTRAN5_MEAN.mat');
load('Solar_ASTM_E-490-00.mat');
load('Solar_ASTM_G-173.mat');
load('Albedo.mat');
load('Racoon_Sun_spec.mat');
model.spec.IR = IR;
model.spec.Solar = Solar;
model.spec.RacoonSun = RacoonSun;
model.spec.AM15 = AM15;
model.spec.Alb = alb;
clear IR Solar AM15 alb RacoonSun

%% Surface coatings
model.coat.a = [];
model.coat.b = [];
model.coat.path = [model.Path.Source filesep 'Messdaten/02 Coatings'];
addpath(model.coat.path);
fns = fieldnames(model.coat);
coatings = {'AgP', 'BP'};
for i = 1:numel(coatings)
    load(['data_' coatings{i}]);
    model.coat.(fns{i}) = load(['data_' coatings{i}]);
end
clear fns coatings name i R epsilon

%% Photodiode (Vishay)
model.PD.path = [model.Path.Source filesep 'Messdaten/03 Photodiode'];
addpath(model.PD.path);
model.PD.c = 700; %[J/kg/K] specific heat capacity
model.PD.V = 18e-9; %[m^-3] volume
model.PD.k_PD_PCB = 100; %[W/m/K] thermal conductivity of contact PD-PCB
model.PD.A_PD_PCB = 2e-6; %[m^2] contact area PD-PCB
model.PD.rho = 3e3; %[kg/m^3] density
model.PD.A_PD_rad = 7.5e-6; %[m^2] Radiant sensitive area
model.PD.coat = load([model.coat.path '/data_PD.mat']);
load('PD_model_S_lambda.mat');
model.PD.S_lambda = S_lambda; %[-] model spectral sensitivity
model.PD.x_z = 10e-4; %[m] PD node height above PCB
model.PD.gamma_A = 0.4;
clear S_lambda;

%% PCB material parameters (FR4/1oz)
model.PCB.rho = 2.0e3; %[kg/m3] density
model.PCB.c = 1.2e3; %[J/kg/K] specific heat capacity
model.PCB.k_t = 1.059; %[W/m/K] thermal conductivity along
model.PCB.k_z = 0.343e-1; %[W/m/K] thermal conductivity through
model.PCB.coat = load([model.coat.path filesep 'data_PCB.mat']);

%% Thermistor paramters (DS18B20)
model.THM.k_THM_PCB = model.PCB.k_t; %[W/m/K] thermal conductivity with PCB
model.THM.A_THM_PCB = 9e-6; %[m^2] contact area THM PCB
model.THM.c = 1000; %[J/kg/K] specific heat capacity

```

```
model.THM.V = 20e-9; %[m^-3] volume
model.THM.rho = 1.5e3; %[kg/m^3] density
model.THM.A_THM_rad = 9e-6; %[m^2] radiant active area of the thermistor
model.THM.x_z = 5e-4; %[m] THM node height above PCB
model.THM.omega = 1e-3; %[W] internal power dissipation

%% Analog to Digital Converter
model.ADC.G1 = 25;
model.ADC.G2 = 2.5;
model.ADC.U_ref = 2.56;
model.ADC.res = 10;
model.ADC.OFFSET = -25;
```